

2010-2011 AIAA Foundation
Team Aircraft Design Competition



-Proposal-



USC Advanced Commercial Concepts Presents:

Azalzan

University of Southern California

University of California, Los Angeles

California State University, Los Angeles.



Todd Erickson
Member # 421648
USC
Thermal Control
Aerodynamics (CFD)

Elias Montoya
Member # 436282
USC
Propulsion
Structures

Sina Golshany
Member # 281677
USC
Lead Designer
System Integration

John Roehrick
Member # 421593
USC
Weight
Aerodynamic Performance

Ethan Sung
Member # 437744
USC
Stability & Control
Aerodynamic Performance



Dr. Geoff Spedding
Member # 233796
USC
Chairman & Project Advisor

Dr. Ossama Safadi
Member # 283128
USC
Faculty Advisor

Dr. Ron Blackwelder
Member # 1460
USC
Industrial Advisor

Michael Zarem
Member # 416621
USC
Structures
Ground Operations

Keith Homlund
Member # 413045
USC
Aerodynamics
High-Lift Mechanism

Darin Gaytan
Member # 279164
USC
Team Manager
Performance

Peter Anuyouthapong
Member # 438401
USC
Weight
Cost Analysis

Bahram Solhjou
Invoice # 797784
USC
Electric Systems
Weight

Dr. Geof Eldredge
Member #
UCLA
Faculty Advisor

Table of Contents

Nomenclature	4
Acknowledgement	7
Executive Summary.....	8
Requirements Matrix	10
Configuration Highlights	11
1.0 Design Methodology	12
2.0 Preliminary Sizing	13
2.1 Preliminary Aerodynamic Analysis	13
2.2 Battery Technology Evaluation.....	14
2.3 Mission Analysis	15
2.4 Preliminary Weight Analysis	16
2.5 Performance Sizing Chart	17
3.0 Market Analysis.....	18
4.0 Configuration Trade-offs.....	21
4.1 Sensitivity Analysis	21
4.2 Configuration Selection	22
5.0 Configuration Description.....	24
5.1 Fuselage Geometry.....	24
5.2 Cockpit & Ergonomics.....	24
5.3 Cockpit Access.....	26
5.4 Cargo Stowage	26
5.5 Wing Planform, Winglets, and Folding Mechanism.....	27
5.6 Empennage.....	28
5.7 Propeller.....	28
5.8 Electric Motor.....	29
5.9 Landing Gear.....	30
5.10 3-View Foldout.....	31
5.11 Inboard Profile.....	32
6.0 Aerodynamics	33
6.1 Airfoil Design.....	33
6.2 Wing Planform Optimization	34
6.3 Winglets.....	36
6.4 High Lift Devices	36
6.5 Wetted Area Distribution	37
6.6 Detailed Drag Polars and Breakdown	38
6.7 Full Airplane CFD Drag Verification.....	39
7.0 Structural Analysis.....	43
7.1 Loads V-n Diagram.....	43
7.2 Fuselage Structure	44
7.3 Landing Gear Attachment and Structure.....	45
7.4 Wing Structure	46
7.5 Wing Flutter Considerations.....	48
7.6 Empennage Structure.....	51
7.7 Manufacturing Methods	51
8.0 Propulsion.....	52
8.1 Electromotor Type Selection.....	52
8.2 Propeller.....	52
9.0 Electrical Systems.....	55
9.1 Electrical Storage	55
9.2 Electric Distribution Architecture	56

9.3 Avionics and Secondary Electrical Components	56
9.4 Electric System.....	58
10.0 Systems Integration	60
10.1 Heat Management	60
10.2 CFD Verifications	61
10.3 Flight Control System.....	63
10.4 Steering and Brakes.....	63
10.5 Mechanical Systems Integration Foldout.....	65
11.0 Weight Justification & Analysis	66
11.1 Detailed Weight Analysis	66
11.2 Class III Weight Estimation	67
11.3 Exploded Weight Group Foldout.....	68
11.4 Center of Gravity Analysis.....	69
12.0 Stability and Control.....	70
12.1 Loading Cases	70
12.2 Balance, CG Travel, and Wing Location	70
12.3 Tail Sizing and Trim Diagram	71
12.4 Stability & Control Derivatives	71
12.5 Aileron Sizing.....	73
12.6 Dynamic Stability.....	73
12.7 Propeller Tilting.....	74
13.0 Performance	75
13.1 Performance of Installed Powerplant.....	75
13.2 Takeoff Performance	75
13.3 Climb Performance	76
13.4 Maximum Cruise Speed.....	76
13.5 Maneuvering Performance.....	77
13.6 Endurance	77
13.7 Landing Trajectory	78
13.8 Stall Speed.....	78
13.9 Noise Assessment.....	79
14.0 Maintenance & Operations	80
14.1 T-Hangar & Storage.....	80
14.2 Battery Recharging Performance	81
14.3 Battery Lifecycle & Replacement.....	81
14.4 Extended Endurance Battery Package	82
14.5 Regular Inspections.....	83
14.6 Accessibility Picture	84
15.0 Safety Features and Analysis	85
15.1 Deep Stalls and Propeller Tilting	85
15.2 Parachute Deployment	85
15.3 G Seats, Seatbelts, and Airbags	86
15.4 Wings Folded	86
15.5 Lightning Strike	87
16.0 Cost & Risk Analysis	88
16.1 Market Forecast	88
16.2 Project Risk Assessment.....	88
16.3 Itemized Cost Estimation	89
16.4 Operating Cost.....	92
References	93

Nomenclature

A	Blade wetted area
α	Angle of attack
AR_w	Wing aspect ratio
$\bar{\gamma}$	Average flight path angle
C_a/C_w	Aileron chord to wing chord ratio
C_D	Airplane drag coefficient
$C_{D0_{TO}}, C_{D0_{clean}}$	Airplanes zero-lift drag coefficient at takeoff, clean configuration
$C_{d_{blade}}$	Average Blade Drag Coefficient
CGR	Climb Gradient
$C_{L_{maxS(Clean)}}$	Maximum lift coefficient for clean stall configuration
$C_{L_{maxTO}}$	Maximum lift coefficient at takeoff
$C_{L_{opt,MaxR}}$	Lift coefficient correspond to the optimum range performance
C_{l_a}	Airplane rolling-moment-coefficient due to ailerons deflection
C_{m_a}	Airplane pitching-moment-coefficient-due-to-AOA derivative
$C_{m_T(PT)}$	Airplane moment-coefficient-due-to-thrust-from-prop-tilting
C_{l_β}	Airplane rolling-moment-coefficient-due-to-yaw rate-derivative
C_{n_β}	Airplane yawing-moment-coefficient-due-to-side-slip-derivative
C_p	Coefficient of Pressure
d/D	Ratio of the radome diameter to the average diameter of the mid fuselage
D_p	Diameter of the propeller
Δ_h	Change in altitude
$\zeta_{P, long}$	Longitudinal phugoid mode damping ratio
ζ_{SP}	Short period mode damping ratio
η_{i_f}	Flap inboard station, in term of wing half span
η_{O_f}	Flap outboard station, in term of wing half span
$I_{xx_B}, I_{yy_B}, I_{zz_B}$	Moment of inertia along the body axis
$Level_p$	Level for phugoid stability
$Level_{\xi_{SP}}$	Level for short period damping
$L/D _{TO}$	Lift-to-Drag ratio at takeoff
λ_w	Wing taper ratio
Λ_w	Wing sweep angle
Λ_{LE}	Leading edge wing sweep
m_b	Blade mass
NP_{free}	Free stick neutral point
$n_{pull-up}$	Load factor during pull-up maneuver
n_{turn}	Load factor during turning maneuver
$P_{t,2}$	Intermediate parameters to compute Phillip's angle
$P_{SpExPwr}$	Specific Excess Power
Π_{TO}	Engine setting at takeoff
Q_1	Dynamic Pressure
R/C	Rate of climb

R_{turn}	Radius of maneuvering turn
S_{air}	Distance from obstacle height to the point of touchdown
S_L	Landing distance
S_{LG}	Ground roll landing distance
SM_{free}	Stick free static margin
S_{TO}	Total field length
S_{TOG}	Take-off ground run distance
S_W	Wing surface area
SM	Static margin
$t(1 \rightarrow 3)$	Time to climb
$T_{\frac{V}{2_p}}$	Time to half amplitude in phugoid mode
T_{avail}	Thrust available
T_{req}	Thrust required
v_0	Initial tangential blade velocity at blade center of mass
V_A	Approach speed
$V_{Cr_{\text{Max}}}$	Maximum cruise speed
V_{LOF}	Speed at liftoff
V_m	Speed in maneuver
V_s	Stall speed
V_{SL}	Landing stall speed
$V_{s_{\text{TO}}}$	Takeoff stall speed
W_E	Empty weight
W_{fix}	Weight of Fixed Equipment
W_{PL}	Weight of the payload
W_{PP}	Weight of the powerplant
$W_{\text{Structure}}$	Weight of the structure
W_{TO}	Takeoff weight
$W_{\text{TO,Extended}}$	Takeoff weight, extended mission
$W_{\text{TO,Light}}$	Takeoff weight, light mission
$(W/S)_{TO_{\text{max}}}$	Maximum take-off wing loading
$(W/T)_{TO_{\text{max}}}$	Maximum take-off power loading
φ	Thrust vector inclination with respect to freestream airflow
X_{apex_W}	X coordinate of the wing apex (i.e. distance b/w wing quarter chord station and the nose reference point)
$\bar{x}_{ac}, \bar{x}_{ac_{uf}}, \bar{x}_{ac_b}$	X coordinate of aerodynamic center in terms of mean aerodynamic chord
X_{CG}, Y_{CG}, Z_{CG}	Location of center of gravity
\bar{x}_{cg}	X coordinate of center of gravity in terms of mean aerodynamic chord
$\omega_{n_{P,\text{long}}}$	Longitudinal phugoid mode undamped natural frequency
$\omega_{n,\text{s.p}}$	Short period undamped natural frequency
Ω	Phillip's angle (Impingement angle) of a released blade

Acronyms:

AAA	Advanced Aircraft Analysis
AIAA	American Institute of Aeronautics and Astronautics
AIMC	Aircraft Information Management Computer
ACE	Actuator Control Electronics
CAD	Computer Aided Design
AR	Aspect Ratio
CFD	Computational Fluid Dynamics
CFRP	Carbon-fiber reinforced plastics
<i>cfm</i>	Cubic Feet per Minute
CG	Center of Gravity
DOC	Direct Operating Cost
DSM	Design Structure Matrix
EPNdB	Effective Perceived Noise in Decibels
ESDU	Engineering Sciences Data Unit
E/E	Electrical/Electronics
EIS	Entry into Service Date
ERP	Extended Range Pack
FAA	Federation Aviation Administration
FAR	Federal Air Regulation
FEA	Finite Element Analysis
<i>fpm</i>	Feet per minute
GAMA	General Aviation Manufacturers Association
ICA	Initial Cruise Altitude
ISA	International Standard Atmosphere
L/D	Lift-to-Drag Ratio
LAMA	Light Aircraft Manufacturers Association
LSA	Light Sport Aircraft
MFD	Multi-Function Display
MLW	Maximum Landing Weight
NLF	Natural Laminar Flow
RDTE	Research Development Testing and Evaluation
RFP	Request for Proposal
RMPU	Remote Power Management Unit
RPM	Revolutions per Minute
SAE	Society of Automotive Engineers
SAR	Specific Air Range
S-LSA	Special Light Sport Aircraft
UACC	University of Southern California Advanced Commercial Concepts
USAF	United States Air Force



Acknowledgement

We would like to express our appreciation for the help and support given by the faculty of USC's Aerospace and Mechanical Engineering department. First of all, we wish to thank the people who were integral to the creation of this project: *Dr. Geoff Spedding*, *Mr. Blaine Rawdon*, and *Mr. Mark Page*. With their experience in the field of aircraft design, they have been very supportive in all the phases of this project. During the first year of his retirement, *Dr. Ron Blackwelder* contributed greatly to all aspects of this project, including organizational support for team members. *Dr. Daniel P. Raymer*, president of the *Conceptual Design Corporation*, also contributed greatly by providing well needed advice and feedback. Special thanks are also due to *Marc Aubertine* in USC's engineering writing program for his contribution to the organization and composition of this proposal. During the development of this aircraft, UACC was provided with information regarding subsystem components and technologies presently under development in various fields: *Martin Gabrielsson*, CIO of *Amapola Flyg*, Sweden, provided great information regarding the present development of an iPad based avionics cluster. *Dr. Lutgard C. De Jonghe*, Faculty Senior Scientist at Lawrence Berkeley National Labs and *Dr. Binod Kumar*, from the University of Dayton Research Institute, provided UACC with critical information regarding the advancements in Lithium-Air battery technology. Also, great mentorship was provided by *Mr. Marty Bradley* of *The Boeing Company* with regard to electric aircraft architecture and subsystems.

We would also like to express appreciation for faculty and staff both at USC and UCLA, whose contributions made this project possible. Firstly, USC's Aerospace Engineering Department faculty and staff including *Dr. David Wilcox*, *Dr. Hai Wang*, *Samantha Graves*, *David Salter*, and *Silvana Martinez-Vargas* contributed greatly by providing organizational support. *Dr. Jeff D. Eldredge*, Associate Professor of UCLA's Department of Aerospace and Mechanical Engineering, assisted the team with regard to aerodynamic design. Last but not least, we wish to give thanks to all our friends and family for being there, providing both an understanding and supportive attitude in a multitude of ways.

May 2011, Los Angeles
USC's Advanced Commercial Concepts Team

Executive Summary

Due to improvements in methods of production and design, owning a Special Light Sport Aircraft (S-LSA) has become increasingly popular over the past few years. However, with the expected increase in oil prices plus stricter environmental regulations, the ever rising operating cost limits the market for this type of aircraft. Through the recent advancements in electric motor design and battery technologies, new avenues are enabled for the next generation of S-LSAs which allow them to be more affordable, more reliable, and safer than models presently in production.

This proposal describes the design of Azalzan, a fully electric S-LSA which implements state of the art electric propulsion technology as well as innovative features, promising an overall reduction in the operating cost through the elimination of the dependency on aviation fuel. Azalzan also implements a specialized prop-tilting mechanism to improve its safety in recovering from a deep stall (a situation not uncommon with S-LSAs). As with all aircraft designs, emphasis is placed on obtaining a fail-safe configuration that complies with industry and federal standards for Light Sport Aircraft.

From the standpoint of aerodynamic configuration, Azalzan utilizes high aspect ratio folding wings that provide compatibility with current airport infrastructure while increasing overall aerodynamic efficiency. Natural laminar flow technologies, verified using high resolution Computational Fluid Dynamics (CFD) simulations, are employed heavily in order to further reduce the friction drag produced by the airframe. The high aspect ratio wing planform dictates a need for particular attention to the structural design of the wing components to avoid aero-elastic flutter. Numerical methods and tools were developed to accomplish this task and ensure that the speed at which flutter of the wing structure occurs is well above the maximum speed anticipated in the flight envelope for Azalzan. Carbon fiber composite components were used extensively throughout the structure enabling substantial weight reductions, as well as making the high aspect ratio wing planform structurally feasible.



Azalzan features a specially designed, high performance Lithium-Air battery package, with the configuration providing room for an additional battery unit for extended-range missions. The electrical circuit and power management system has been fully designed and analyzed, enabling the accurate quantification of energy consumption and heat generation at each component to be addressed by the thermal management system.

During the conceptual design phase of the project, it was realized that the utilization of a fully electric power architecture presents difficulties with respect to thermal management. Due to limited volume and large amounts of dissipated heat, as well as the inherent inefficiency of composite structures in conducting thermal energy, design and implementation of effective heat management solutions received significant attention. High fidelity numerical tools were utilized to perform thermal simulations ensuring the effectiveness of the designed system even in the most critical flight scenarios.

As the intended users of the aircraft include aviation enthusiasts and private pilots who would use the aircraft for leisure purposes, particular attention was paid to the ergonomics of the cockpit interior, payload compatibility, and occupant visibility. Further, noise reduction played a decisive role in determining the technology level for the propeller system integrated into the design.

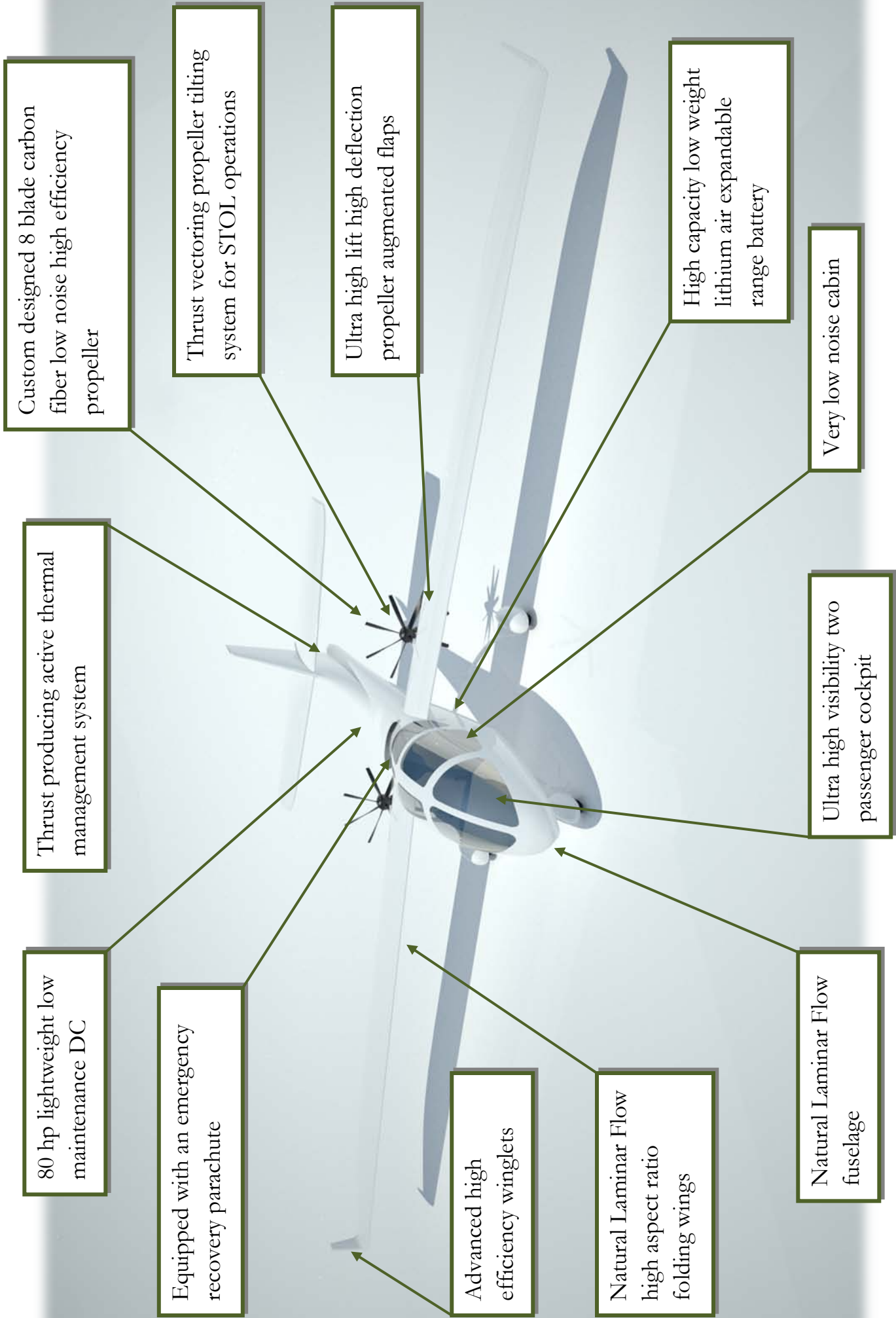
A wide variety of expertise was utilized due to the large number of disciplines involved and the high level of detail intended for the project. Team members from the University of Southern California, University of California, Los Angeles, and California State University, Los Angeles majoring in Aerospace Engineering, Mechanical Engineering, Electrical Engineering, Computer Science, and Physics collaborated on various aspects of the project to develop the final design.

Given the high level of detail considered and the high fidelity of the analysis methods utilized, it is the unilateral belief of UACC that Azalzan represents an astute blend of design innovation, technology integration, and cost effectiveness presently unmatched by any similar craft in the market.

Requirements Matrix

Table 1. Selected design parameters

Parameter	Requirement	Azalzan	Section
RFP			
Take-Off and Landing Distance over 50' Obstacle	$\leq 1600'$	600' takeoff, 1000' landing	§13.2, §13.7
Climb Rate Sea Level	$\geq 500 \text{ fpm}$	625 fpm	§13.3
Cruise Speed	80 $kts.$	$\leq 80 kts.$	§2.3
Max Operating Speed	110 $kts.$	180 $kts.$ No de-rating 147 $kts.$ Never exceed limit	§13.4
Max Altitude Capability	11,500'	$>11,500'$	§13.3
Climb Rate Max Operational Altitude (Std. Day +15 °F)	$\geq 100 \text{ fpm}$	$\geq 100 \text{ fpm}$	§13.3
Max Endurance	1 hr. 45 mins.	2 hrs. 45 mins.	§13.6
Extended Endurance	3 hr. 30 mins.	6 hrs. 10 mins.	§13.6
Seating	2	2	§5.2
Cabin Height & Width	Compatible with two 6'5" Adult Males	Compatible with two 6'5" Adult Males with winter outfits	§5.2
Cargo Volume	$\geq 10 \text{ ft}^3$	11 ft^3	§5.4
Useful Load	$\geq 400 \text{ lb.}$	400 lb.	§12
Battery Technology	Technology EIS 2016	Lithium Air (available in the timeframe of 2016)	§2.2, §9.1
Battery Replacement	500 cycles	500 cycles	§9.1, §14.3
Charging Time	$\leq 4 \text{ hrs. w/}$ 220/240 volt source	3.8 hrs. 220/240 volt source	§14.2
FAR §23 Adaptations			
§23.65 Rate of Climb	$\geq 1.2 V_{S_1(\text{clean})}$	Satisfied	§13.3
§23.65 Climb Gradient ISA	8.3%	10%	§13.3



1.0 Design Methodology

The general design philosophy of Azalzan has been substantially influenced by methodology presented by *Jan Roskam*¹ and *Ed Heinemann*². It should be noted that these methods are often quite extensive and cover technical aspects of the analysis in great detail. The majority of calculations performed and referenced within this proposal use published graphs and tables in order to determine the constants and parameters, often consisting of multiple time-consuming iterations. While the theoretical backgrounds of these methods are discussed in various parts of this proposal, many of the mathematical models and statistical data used in the design process are not presented in their entirety in the interest of brevity.

Design Structure Matrix (DSM), a modern method of development management, was used in order to determine the optimum design process. This method, described by *Eppinger et al.*³, is used to organize interrelated tasks in the design process in a way that minimizes feedback cycles and determines possible parallel analyses. The PSM 32 code, developed by Blitzkrieg Software, was utilized to implement the DSM in the routine process of developing Azalzan. Utilizing this code, the entire design process was re-ordered based on the degree of dependency of each sub-process on the outputs of others. As a result, the design approach presented by *Roskam* has been slightly modified so as to allow for additional parallel processes, as dictated by specific needs of the Azalzan concept, and consequently, improved development speed.

2.0 Preliminary Sizing

2.1 Preliminary Aerodynamic Analysis

Initial empirical drag polars were obtained using 2nd order regression methods presented by Roskam^{4,5} as well as results from the preliminary weight analyses of Azalzan. ESDU Performance Data Item 73018⁶ was consulted to choose the critical parameters with the highest influence on maximum Specific Air Range (SAR). Three parameters were chosen to investigate the optimal lift coefficient for the aircraft when operating at cruise: C_L/C_D , $C_L^{0.5}/C_D$ and $C_L/C_D^{3/2}$. ESDU 73018 suggests $C_L^{0.5}/C_D$ to be maximized, which corresponds to the maximum SAR at a fixed altitude, maintaining the same rate of energy consumption. Therefore, a battery powered airplane with a higher SAR would be able to fly further with the same battery pack*. As it can be seen from Fig. 1, the SAR is maximized if the aircraft is operating at a lift coefficient of 0.65, which is significantly lower than the lift coefficient corresponding to maximum L/D (1.2). However, one could observe that the C_L/C_D curve in Fig. 1 is relatively flat around a lift coefficient of 0.5; therefore, the reduction in maximum air range as a result of optimizing the aircraft for maximum SAR is minimal.

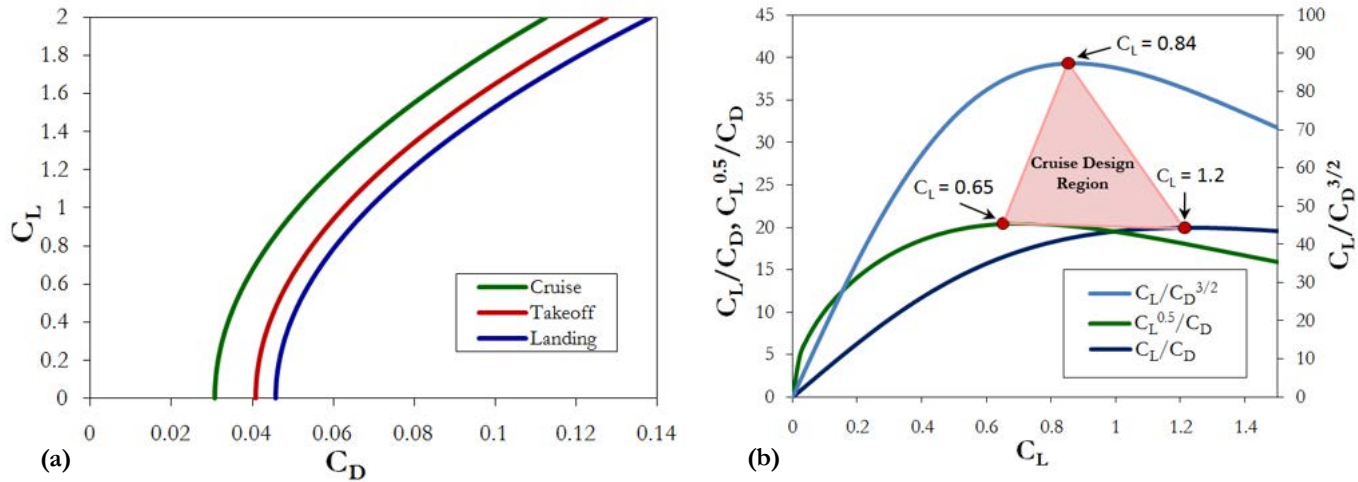


Fig. 1 Results of the preliminary aerodynamic projections. (a) Preliminary drag polars for different mission segments of the aircraft. (b) Parametric analysis of lift and drag data. C_L corresponding to maximum C_L/C_D maximizes the SAR at constant air speed. C_L corresponding to maximum $C_L/C_D^{3/2}$ maximizes the SAR at constant thrust. Parameter $C_L^{0.5}/C_D$ maximizes SAR at constant altitude and was selected based on the recommendations made by ESDU 73018 as a measure of merit, defining a design region of acceptable cruise C_L 's depending on the mission intended.

* SAR, in a typical fuel-burning aircraft, represents essentially the sensitivity of the air range to the amount of fuel used. Comparably, as the fuel carried on board represents mostly the amount of work done to overcome aerodynamic drag, an electric airplane carries potential energy in a chemical form to be converted to electric power (i.e. the battery, which is a substantial portion of the takeoff weight).

2.2 Battery Technology Evaluation

In reviewing literature relevant to technology developed for high energy density battery packs, and in examining studies on the future of battery technologies for aerospace applications, it was determined that metal-air battery concepts will be a viable technology available in the timeframe of 2016. In particular, a paper published by *K. M. Abraham*⁷ expressed very favorable opinions on the performance of metal-air batteries available for aerospace applications. Significant improvements in energy density are observed among next generation metal-air batteries that would make them a viable replacement for present state-of-the-art Lithium-Ion batteries. Performing a case study of performance and cost of various battery technologies, summarized in Table 2, it was observed that Lithium-Air batteries have the highest overall specific energy and energy density of all current and near future battery technologies. Although the specific costs of Lithium-Air batteries are projected to be substantially higher than Lithium-Ion batteries, it appears that this general difference is more than compensated by their improvements in specific energy and energy density. Such improvements make them ideal for applications in aerospace design, where space is limited and weight has significant effect on vehicle performance. Further investigation into the operation of Lithium-Air batteries⁸ revealed that their generic operating temperatures are very high (122 °F to 158 °F) due to their exothermic internal chemistry. This potentially leads to a need for a compact cooling system to prevent the temperatures from exceeding their optimal range.

Table 2 Summary of battery technology study. * denotes cost values that have been extrapolated from battery technology cost trends.

Battery Type	Specific Energy (Whr/kg)	Energy Density (Whr/L)	Cost (\$/kg)
<i>Lithium-Ion:</i>			
LiMn ₂ O ₄	100	243	15
LiFePO ₄	108	145	12
LG LiPo Gen 3	95	155	11.84*
LG Li-Ion	200	480	31
Tadiran XOL	252	645	40.50*
<i>Lithium-Air:</i>			
Li-Air (PolyPlus)	700	1000	122.25*
Li-Air (UDRI)	1000	1000	177*

2.3 Mission Analysis

In order to determine the mass of the battery, it was necessary to compute the amount of energy required to perform the mission outlined by the RFP. Using the results of the preliminary aerodynamic analysis as well as basic physical principles, the work done by the major forces acting on the airplane (namely Drag, Lift, and Gravitational Forces) was computed considering the mission presented in Fig. 2 and summarized in Table 3.

Table 3 Summary of Mission Energy Requirements

Flight Condition	Altitude (ft)	Speed (kts.)	Duration (min)	Preliminary C_D	Energy (Wh)	Energy Fraction
1. Takeoff	0	45	10	0.077	1,200	4 %
2. Climb	4,750	60	15	0.046	7,000	23 %
3. Cruise	9,500	80	60	0.037	15,000	50 %
4. Descent	6,000	60	7.7	0.048	1,300	4.33 %
5. Loiter	2,500	60	30	0.044	4,500	15 %
6. Descent	1,250	60	7.7	0.044	600	2 %
7. Landing	0	40	3	0.089	400	1.33 %

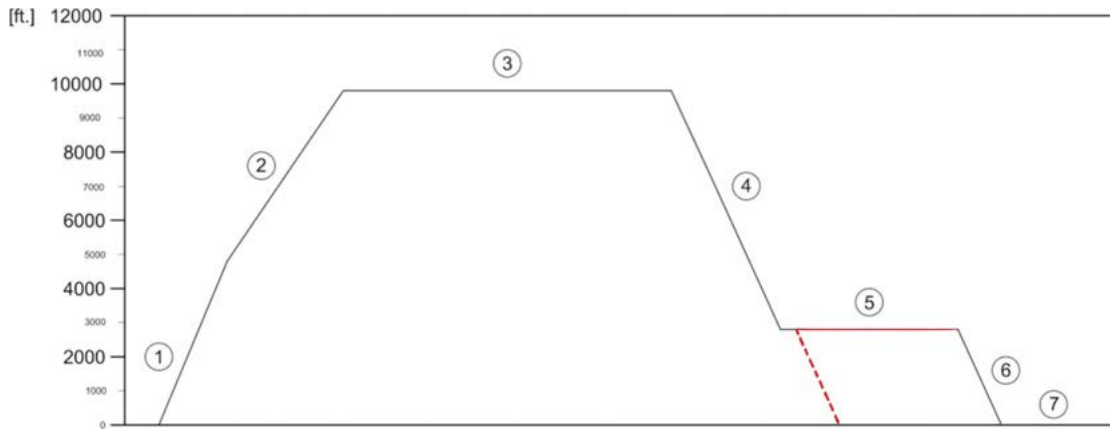


Fig. 2 Mission Profile. Note that the red solid line signifies the reserve mission, and the red hashed line signifies landing with the loiter segment in reserve.

From this analysis it was determined that the mission profile will involve a total of 30,000 Wh. of mechanical work done by the airplane. In order to account for losses due to propeller inefficiency, battery heat loses, and other energy loses in the circuit, an overall efficiency factor needed to be computed. Yuneec International states that the efficiency for an 80 hp DC brushless motor for aerospace applications is about 90%⁹. In personal correspondence with UACC, *Dr. Lutgard C. De Jonghe* claims that the efficiency for a high performance Lithium-Air battery pack is

approximately 70% at relatively high drain rates¹⁰. It was also assumed that a ground adjustable propeller with the efficiency of 85% can be designed to operate satisfactorily at all mission segments¹¹. Another efficiency factor of 98% was assumed to account for power loses due to circuit inefficiencies, electric power extraction to run the cooling system, avionics, and lighting. Therefore the overall efficiency was computed from multiplying all the individual efficiencies yielding an efficiency factor of about 52%, accounting for all power extractions and thermal loses. This computation yielded the first order estimate of battery capacity to be 67 kWhr . Inquires were made to the University of Dayton Research Institute (a leading institution in the field of metal-air battery technologies) with regard to the energy density of a generic Lithium-Air battery with an expected EIS of 2016. In response, *Dr. Binod Kumar*¹² cited an energy density of $1,000 \text{ kWhr./kg.}$, resulting in an approximately 160 lb. battery required.

2.4 Preliminary Weight Analysis

Using the weight fractions obtained from *Roskam*⁸, initial estimations for the empty weight of the aircraft were performed. This analysis was done using regression coefficients presented by *Roskam* that are derived using available weight data for similarly sized airplanes. Table 4 presents the results of this analysis. Note that these results only reflect the statistical trends in light sport aircraft design and are later refined in two phases using higher order methods of estimating weight, to be presented in Ch.11. Despite the electric propulsion system, the weight estimation method that is used for traditional aircraft was assumed to yield similar powerplant weights for either fuel-powered or electric system architectures. This assumption was later verified to be sufficiently accurate for the purpose of preliminary design, as will be presented in Ch. 11.

Table 4. Summary of initial weight analysis

Component	F_{MTOW}	Weight (lb.)
Fuselage	0.16	190
Wing	0.15	180
Empennage	0.03	30
Landing Gear	0.07	85
Engine Cowling	0.01	15
Structure	0.42	500
Powerplant	0.05	60
Battery	0.13	160
Fixed Equipment	0.07	80
<i>Empty Weight</i>	0.67	800
Passengers & Payload	0.33	400
MTOW	1.0	1200

2.5 Performance Sizing Chart

The initial performance sizing of the aircraft was completed based on the performance requirements presented by the RFP, summarized in Table 1, and methods presented by *Roskam*¹³. The wing loading and weight-to-power ratios were obtained by solving performance boundary equations. Based on ESDU Aerodynamics 95021¹⁴, it was assumed in this analysis that a maximum lift coefficient up to 2.0 is achievable by using stand-alone single slotted Fowler flaps and no leading edge high lift devices. Weight figures obtained from preliminary weight estimates were used in conjunction with lift and drag characteristics obtained from preliminary aerodynamic analysis, which are presented in Sec. 2.1 and 2.4, respectively. A matching plot was constructed by overlaying the performance boundary graphs to identify the acceptable design space for wing loading and weight-to-power ratio for Azalzan. The result of this analysis is presented in Fig. 3. With regard to climb performance, requirements set by FAR §23.77 were adopted as the RFP did not specify any climb performance for the aircraft. The design point was selected to minimize the required wing area and engine power while satisfying all performance requirements. A margin of error of 0.4 for $C_{L\max}$ (25% from the target $C_{L\max}$) and $2 \text{ lb}/\text{ft}^2$ (20% from the wing area target) was considered to allow for containment of weight growth in further development. According to the performance sizing chart and mindful of the preliminary weight analysis presented in Sec. 2.4, a target wing area of 136ft^2 and engine power of 80 hp . was selected as the initial design point.

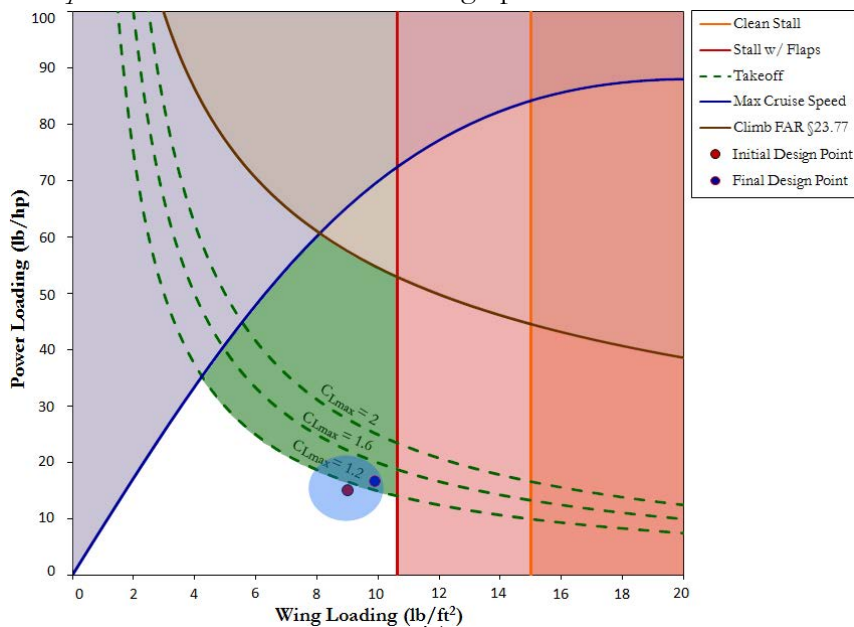


Fig. 3 Performance Sizing Chart. The blue circular region denotes a margin of development around the initial design point. In later design phases, a final design point was determined, lying within the margin.

3.0 Market Analysis

Starting with the release of the Light Sport Aircraft rules in 2005, the market has seen a steady rise in the popularity of this class of airplane. According to FAA estimates, at the end of 2009, there were 6,547 active LSAs. The FAA predicts this number to continue to increase at the rate of 450 per year until 2013 when it should start to abate and continue rising thereafter at a rate of 300 per year.¹⁵ Outside of the US, there is also a strong market for this type of airplane. The European Microlight Federation is looking to expand the microlight rules into an LSA category the same way that LSA in the US was born of the ultralight movement. This is expected to be adopted at standards very close to the US standards as that over 65% of the US sold S-LSAs are manufactured in Europe.² Further, an all-electric LSA would have additional value in Europe where the primary distracter from personal aviation is the cost (attributed to both fuel and fees.) Based on this, we recommend an initial release into the US market with the future direction of expanding to Europe and Asia Pacific.

Reviewing comparable designs currently in operation, it was observed that a heavy emphasis is placed on cockpit visibility. Additionally, manufacturers actively market such a feature to be used for the purposes of sight-seeing and leisure flights. Extrapolating from this trend, UACC decided to provide astute visibility and ergonomics for the cockpit to improve sales.

Typically, LSAs utilize high performance internal combustion engines and low blade number propellers installed forward of the cockpit. Such a configuration, combined with the tendency to minimize weight by reducing the amount of acoustic insulation, leads to aggravated noise levels in the cockpit, reducing the overall passenger comfort. In response, it was decided that a configuration that inherently minimizes cockpit and community noise levels would be preferable if no major sacrifice has to be made in airplane performance.

A general survey of presently operational airplanes was performed by reviewing the data collected and published by the General Aviation Manufacturers Association¹⁶ (GAMA) and the Light Aircraft Manufacturers Association¹⁷ (LAMA). The statistics gathered by GAMA were

analyzed to identify market and technology trends in general aviation airplanes that may apply to S-LSAs.

As it can be observed from Fig. 4, about 95% of the top selling general aviation airplanes and 80% of top selling LSAs shipped within the past 12 years were designed with a side-by-side seating arrangement. It is noteworthy that the increase in the market share of tandem cockpit LSAs is highly influenced by the replicas of the legendary Piper J-3 Cub. As the general customer group of S-LSA airplanes is dominated by personal flyers and flight schools¹⁸, it was decided to utilize a side-by-side cockpit arrangement for the development of Azalzan in order to maximize its marketability. This seating arrangement facilitates face-to-face communication, desirable during personal and instructional flights.

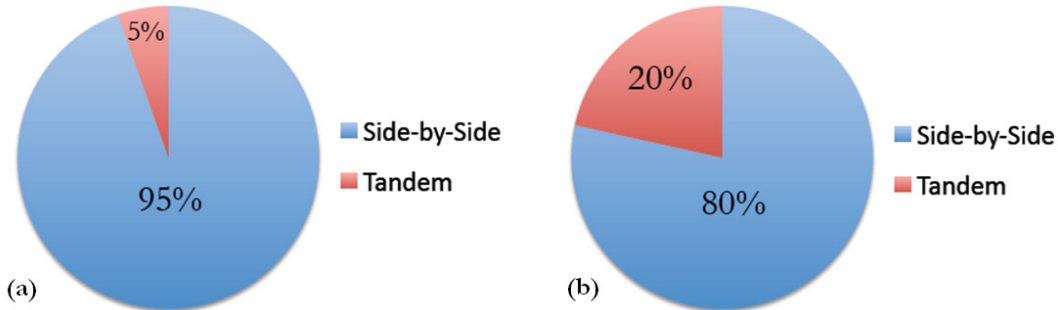


Fig. 4 Seating Arrangement Categories among top selling airplanes from 1999-2011: a) FAR 23 GA airplanes and b) light airplanes

As suggested by Roskam¹⁹, aesthetics and ramp appeal of light airplanes can heavily improve their commercial success. Therefore it was decided that the design, considering continuous improvements in manufacturing methods and cost effectiveness of composites, will feature complex geometries to improve its aesthetics, as well as performance. It was also decided that, to be a commercially successful project, Azalzan has to employ a significantly different design style, distinguishing it from its competitors as an independent and original design.

Reviewing the recent market environment for similar items, it was observed that goods that incorporate innovative technologies achieve better sales as buyers typically appreciate and choose creative designs. Therefore, it was decided that Azalzan must incorporate innovative features that focus on enhancing safety, performance, and airport compatibility.

Reviewing the statistics gathered from GAMA and LAMA, UACC identified a possible, lucrative market for an S-LSA with very short takeoff and landing abilities. It was determined that a large number of licensed LSA pilots have access to vast remote, flat grasslands and underutilized barns, allowing them to own and operate bush planes. It is realized that very short takeoff and landing (STOL) characteristics are essential to the operation of airplanes in such a setup. If the airplane is capable of making very short, low speed takeoffs, it can obtain a winning edge over well established and older airplanes by outperforming them in takeoff and landing distance.

Performing a survey of literature, two major design trends in low cost, STOL light airplanes were observed. First, some of the well established designs in this class use very large wing planforms and extremely light-weight truss-braced structures that allow for STOL performance, while sacrificing usable payload and passenger comfort. In contrast, a group of contemporary STOL aircraft utilizes thrust vectoring and powered flap systems to achieve STOL performance. Figure 5 presents examples of these types of aircraft.



a)



b)



c)

Fig. 5 a) Fi-156 "Storch" b) Piper J-3 Cub c) DornierDo-29

Two main approaches to light weight, STOL airplanes. a) and b) demonstrate the classic approach of large wing area and light weight, cramped cockpit, while c) presents a contemporary solution to achieve STOL performance through thrust vectoring and powered flap systems.

UACC decided that STOL performance characteristics are very valuable additions to the design concept of an S-LSA airplane and, therefore considered such additions as parts of the design philosophy of Azalzan.

4.0 Configuration Trade-offs

4.1 Sensitivity Analysis

A basic sensitivity analysis was performed in order to obtain a more detailed understanding of the relationship between the performance figures and the planform geometry, mainly the aspect ratio. As the range is the factor limiting the practicality of an electric airplane, the effects of aspect ratio and range received particular attention. To compute the effects of the change of aspect ratio on the air range of the airplane, Eq. 1 was used,

$$\left(\frac{\partial R}{\partial AR}\right)_{Cruise} = \left(\frac{\partial C_D}{\partial AR}\right)_{Cruise} \cdot \left(\frac{\partial R}{\partial C_D}\right)_{Cruise} \quad (1)$$

Partials $\partial C_D / \partial AR$ and $\partial R / \partial C_D$ were computed numerically by changing the aspect ratio and obtaining the respective steady state drag coefficient and range during cruise and loiter within the environment of the *Advanced Aircraft Analysis* tool as well as an in-house developed performance tool. Cruise and loiter were selected due to their long durations and their large impact on sizing the battery for the aircraft. The sensitivity of range to aspect ratio was plotted versus aspect ratio and can be seen in Fig. 6. It is noteworthy that the range performance is optimized where the $\partial R / \partial AR$ derivative is very small but positive. It can also be observed that the $\partial R / \partial AR$ derivative during loiter does not change significantly and therefore was found to not be a design parameter for wing geometry. Reviewing the results of this analysis, it was decided that a relatively high aspect ratio wing ($\sim 18-19$) will be needed to optimize the range performance of the airplane at cruise. Relatively higher aspect ratios ($\sim 20-25$) are routinely seen in sailplane configurations with comparable maximum speeds and, given the increased stiffness of modern composite wing structures, such very high aspect ratios may be used with no adverse effect.

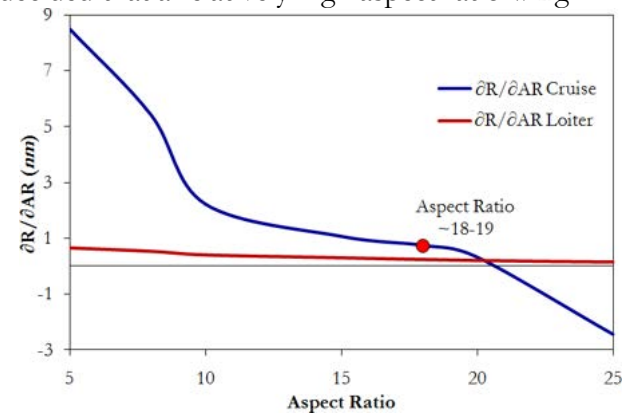


Fig. 6 Results of the sensitivity of range to AR at various ARs, at cruise and loiter. Note that each data point is a fully sized airplane.

4.2 Configuration Selection

Once the seat arrangement and the aspect ratio were selected for Azalzan, it was possible to explore the different possible configurations by evaluating the available options for main component configurations, as summarized in Table 4. The components for which available configurations were explored were wings, empennage, motor installation, and propeller placement.

For the wings, three possible vertical locations were evaluated: low wing, mid wing, and high wing. A high wing installation was selected, in which the lift distribution of the wing is less interrupted by the presence of the fuselage. This results in a higher lift generated by the wing, contributing to a better takeoff performance.

An analogous process was followed for landing gear layout and engine mounting. A tricycle landing gear was selected given its superior ground handling characteristics. A mid-engine configuration was selected for its improved balance characteristics, due to its proximity to region of desirable CG location. Finally, and after having selected the location of the engine and the overall configuration layout of the airplane, a wing-mounted propeller system was selected given promising improvements to high lift aerodynamics through powered flaps. Also, a wing-mounted propeller combined with a high wing configuration allows for improved ground clearance for the deflection of the propellers, facilitating thrust vectoring.

For the empennage, three possible configurations were also evaluated: conventional layout, in which the horizontal stabilizer is attached to the fuselage; cruciform, in which the horizontal stabilizer is attached to the vertical stabilizer; and V-tail, in which vertical and horizontal stabilizers are combined into diagonal surfaces that perform the functions of both. Given the induced swirl in the flow aft of the propellers, a cruciform empennage layout was selected for Azalzan to prevent the horizontal tail from heavily disturbed airflow.

After this synthesis was completed, the configuration of Azalzan was developed into high levels of detail to allow for higher order analyses to be performed. A description of the final configuration is presented in Sec. 5 of this document.

Table 4. Configuration Selection

Wing Location			
Options	High	Mid	Low
Justification	High wings allow the lift distribution of the wing to be less interrupted by the presence of the fuselage. This results in a higher lift generated by the wing, contributing to a better takeoff performance.		
Landing Gear			
Options	Tricycle	Tail Wheel	
Justification	Aircraft with tricycle landing gear have better ground handling characteristics than aircraft with tail wheel landing gear. Takeoff visibility is also improved relative to a tail wheel configuration. Finally, tricycle landing gear aircraft are more desirable for instructional use due to their improved view of the runway.		
Engine Location			
Options	Front	Mid	Rear
Justification	Locating the engine in the middle section of the fuselage makes it easier to provide cooling air for the engine than mounting it in the rear. It is also preferred for balance considerations over rear and front mounted engines, as it will have a lower effect on the location of the <i>CG</i> of the aircraft.		
Prop Placement			
Options	Front	Rear	Wing-Mounted
Justification	A wing-mounted propeller system gives promising improvements to high lift aerodynamics through powered flaps. Also, a wing-mounted propeller combined with a high wing configuration allows for improved ground clearance for the deflection of the propellers, facilitating thrust vectoring.		
Empennage			
Options	Conventional	Cruciform	V-Tail
Justification	A cruciform empennage layout alleviates the horizontal tail from heavily disturbed airflow.		

5.0 Configuration Description

This section describes the final configuration of Azalzan. This serves as a point of reference regarding the geometries and features discussed in later sections of this document that deal with engineering analysis and design of specific aspects of Azalzan.

5.1 Fuselage Geometry

The fuselage features smooth polynomial cross-sections in the forward region and elliptical sections in the aft region. The side and top profiles are designed in a way that the mean surface curvature is always positive while preserving smooth curvature changes to minimize profile drag and delay the transition of the surface flow to turbulence. Efforts have been spent to maintain a constant mean curvature on the regions occupied by transparencies to reduce optical distortion. Figure 7 presents the values of mean curvature plotted on the fuselage surface. Sample cross-sections longitudinal profiles are presented in the three-view foldout and the inboard profile foldout at the end of this chapter.

The fuselage structure is of semi-monocoque construction assembled from mostly Carbon Fiber Reinforced Plastic (CFRP) parts to save weight and increase stiffness. Figure 8 presents a view of the structural arrangement of the fuselage.

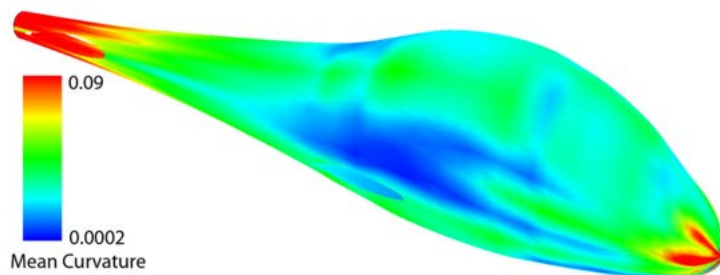


Fig. 7 Mean Curvature Distribution on the fuselage surface

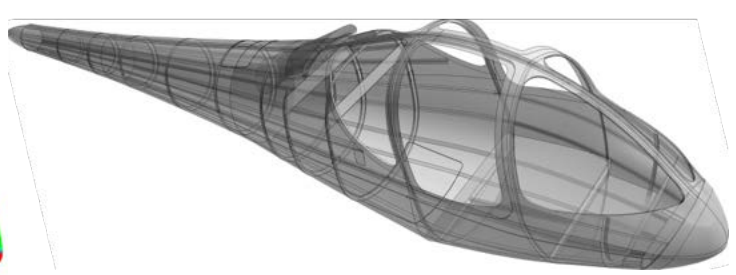


Fig. 8 Structural Arrangement of fuselage

5.2 Cockpit & Ergonomics

As previously mentioned in the market analysis section, particular emphasis was placed on the comfort level of the occupants inside the cockpit. The cockpit was designed to accommodate two 6'2" tall male occupants with comfort, while providing astute visibility and access to flight

controls. The design provides 25° over-the-nose visibility while providing unobstructed visibility to the sides suitable for sightseeing flights.

Figure 9 presents the final visibility pattern of the cockpit. The adjustable seats were designed to provide good lumbar and lateral support as well as crash survivability. The control column was designed to allow for $+9^\circ$ and -17° deflection in the pitch direction, and $\pm 8^\circ$ in the roll direction. Cockpit pedals were designed to allow for maximum rudder surface deflections by $\pm 2''$ of pedal movement, as can be seen in Fig. 10.

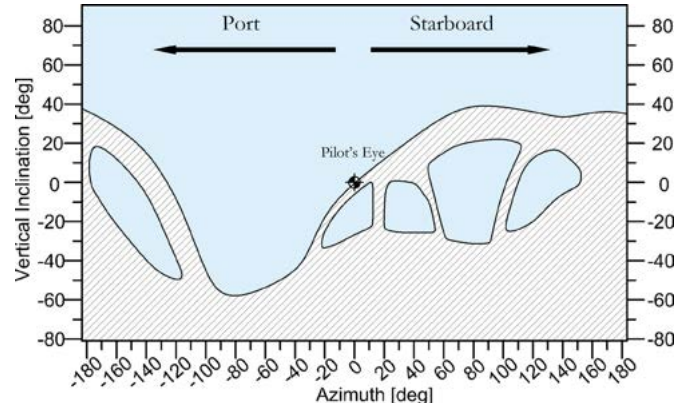


Fig. 9 Visibility Pattern from pilot seat

6'2" Male with winter suit

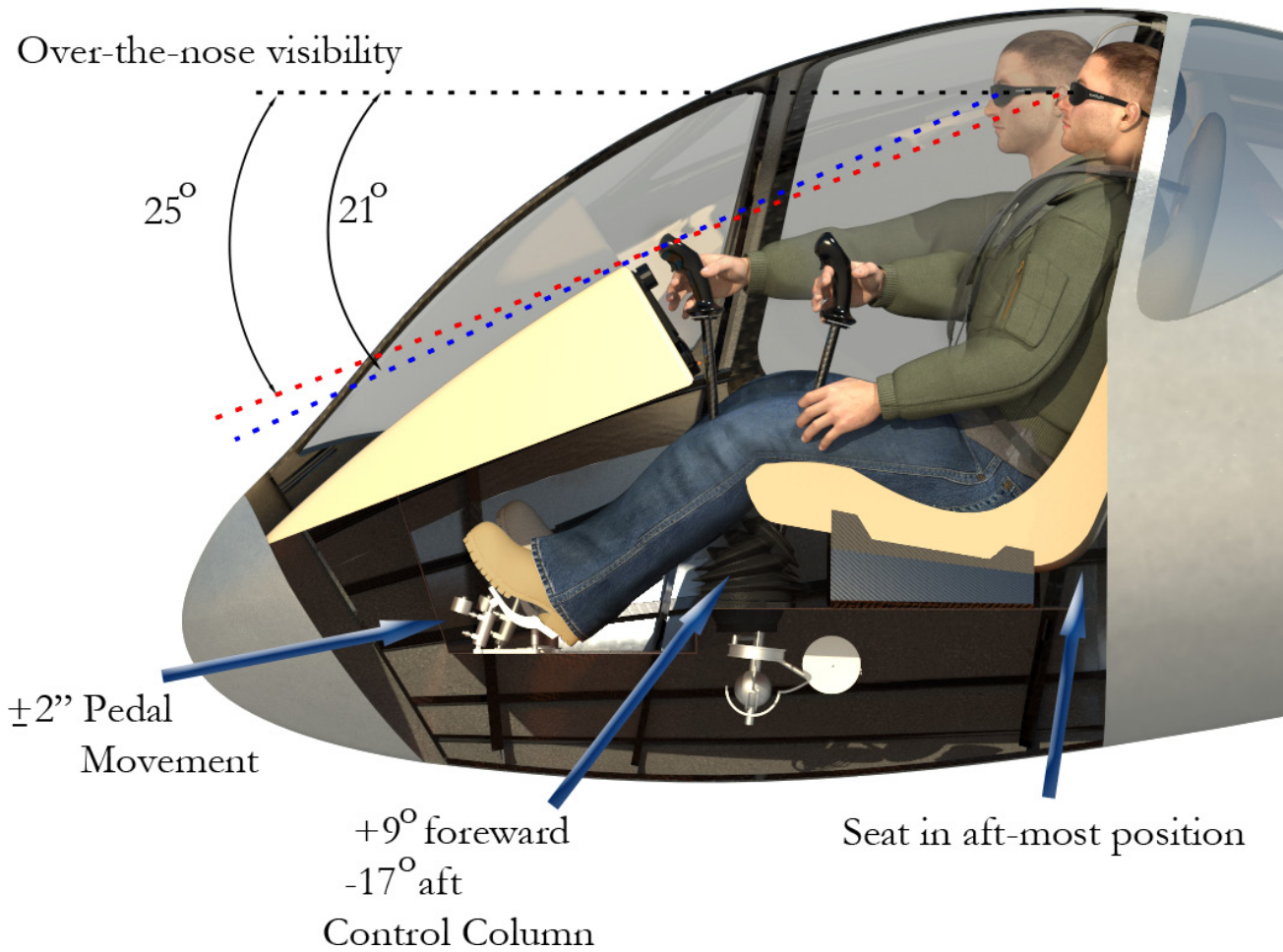


Fig. 10 Cockpit Cutaway Highlights

5.3 Cockpit Access

The cockpit of Azalzan is accessible via two gull-wing doors from the side. A full glass canopy was originally implemented, but after more synthesis, it was decided that the gull-wing arrangement will have a lighter weight and can be designed with a small impact on cockpit visibility, while providing more crash reinforcement to the forward fuselage structure. The doors have a slight curvature to keep them closed and in position using the air flow, should the doors become accidentally opened during flight. Figure 11 presents the location of the gull-wing cockpit doors.



Fig. 11 Gull-wing cockpit doors

5.4 Cargo Stowage

11 ft.^3 of useful volume for cargo stowage is provided, which exceeds the 10 ft.^3 requirement by the RFP. The internal arrangement of the components in mid-fuselage is designed in way to allow oversized popular cargo items for small aircraft (such as a bag of golf clubs, hunting or camping gear). Figures 12 and 13 present a view of the cargo stowage and an inboard profile of the stowage, respectively. Both figures display the capacity to carry oversized items.

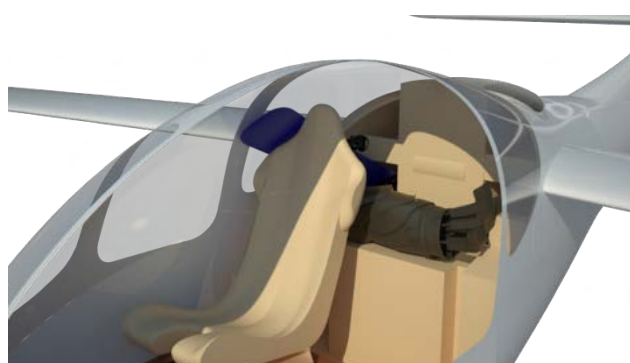


Fig. 12 Cargo Stowage with a golf bag and a snowboard

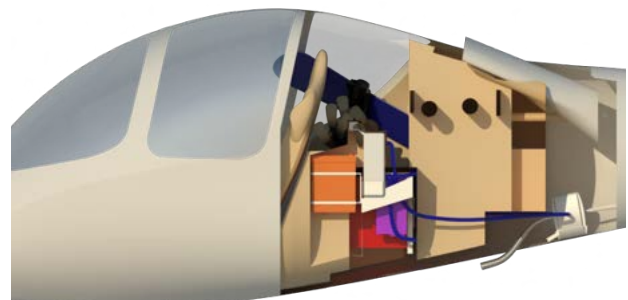


Fig. 13 Cargo Stowage inboard profile with a golf bag and a snowboard

5.5 Wing Planform, Winglets, and Folding Mechanism

The wing planform for Azalzan has an equivalent area of 136.3 ft^2 and a span of 50', resulting in an aspect ratio of 18.35. The quarter chord sweep of the wing is -1.4° while the leading edge is unswept. The taper ratio of the wing is 0.38, selected to optimize the Oswald's Efficiency factor for the wing at cruise. Choices surrounding planform are driven by aerodynamic trade studies and optimizations that are highly influenced by the concept of NLF. The low sweep of the wing planform, combined with relatively low Reynolds numbers and custom designed NLF airfoils, allows for extensive laminar flow (approximately 60%) on upper and lower surfaces of the wing, drastically reducing the friction drag of the configuration at cruise conditions. Sections 6.2 and 6.7 of this proposal present the wing planform optimization and CFD verification for NLF characteristics, respectively. To further increase the efficiency of the wing planform, a 1.28' high winglet is canted from the vertical at 6° . The outboard 7' of the wing is capable of folding via an internal electric folding mechanism to allow taxiing in narrow taxiways and to maintain compatibility with standard T-Hangers, as required by the RFP. The wing is equipped with two sets of single slotted Fowler flaps on the trailing edge extending up to 45% of the wing halfspan. An aileron surface starts at 45% of the wing halfspan and ends at 73% of the wing halfspan, coinciding with the location of the folding line of the outboard wing. Figure 14 presents the wing planform for Azalzan.

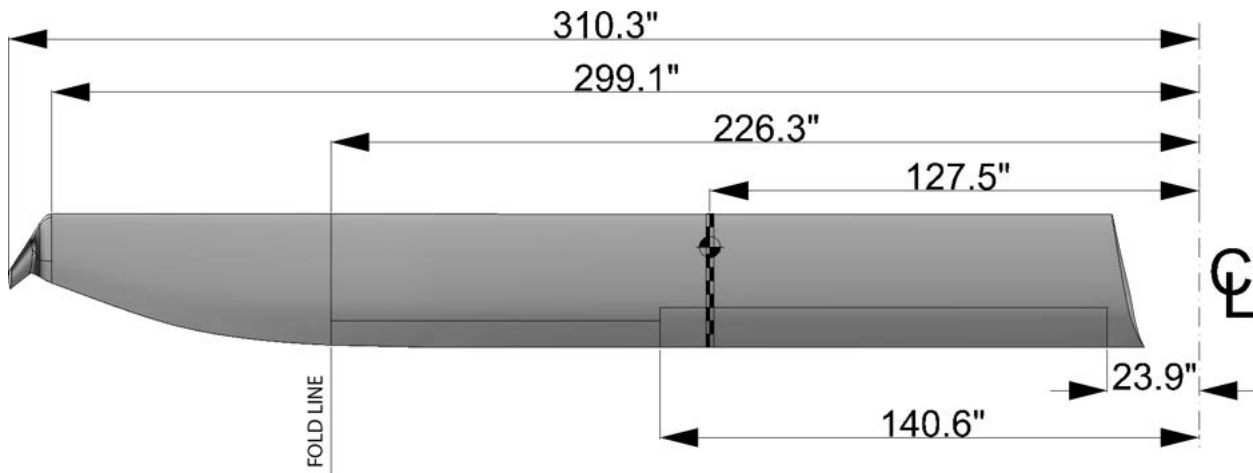


Fig. 14 Wing Planform

5.6 Empennage

The empennage of Azalzan consists of a conventional configuration, offering lower weight and requiring lower stick forces than the considered alternatives. The horizontal tail has a planform area of 42.2 ft^2 and a span of $15.1'$, resulting in an aspect ratio of 5.4. The quarter chord sweep of the horizontal tail is 8.7° . The vertical tail has an aspect ratio of 1.5 and is swept aft by 38° . Both horizontal and vertical tail sweeps are cosmetic features designed to improve the aesthetic qualities of the airplane, which typically lead to better market performance²⁰. The horizontal tail is equipped with elevators on the trailing edge extending up to 90% of the tail span. The structures of the horizontal and vertical tails are conventional, two-spar, semi-monocoque,

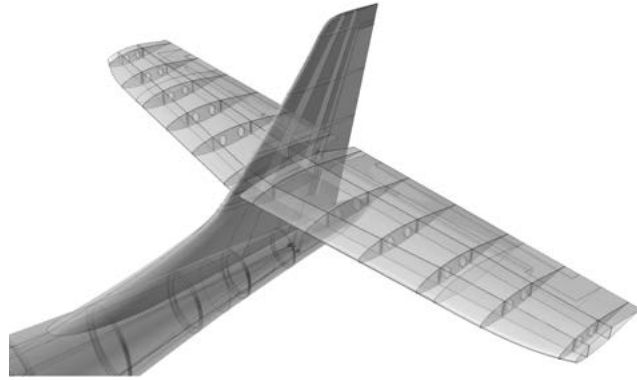


Fig. 15 Empennage Arrangement

composite elements that are fixed on the upper and sides of the fuselage frames. Figure 15 details the empennage structure of Azalzan.

5.7 Propeller

A ground-adjustable propeller was designed for its implementation in Azalzan. Size and noise considerations were the main driving parameters for the design, given the relatively small space available and the goal of improving comfort by reducing noise. In order to obtain the required thrust and match aforementioned constraints, the propeller diameter and number of blades were maximized within the limits imposed by the location selected. Figure 16 presents the propeller of Azalzan. The final design is an 8-blade, 55" diameter, high advance ratio propeller with composite blades and an aluminum hub. A propeller cone was designed to improve the aerodynamic performance of the airplane by faring the base of the propeller hub. A propeller tilting mechanism was designed to increase safety in flight by helping in deep stall recovery. This

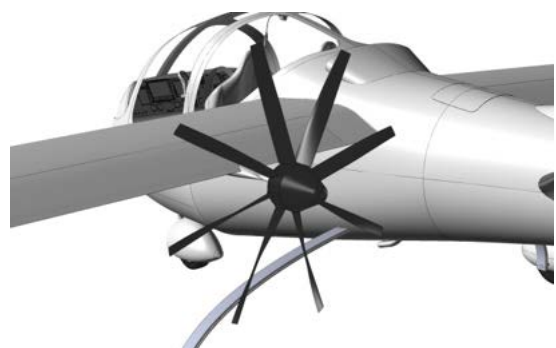


Fig. 16. 8-blade low-noise propeller

presents the propeller of Azalzan. The final design is an 8-blade, 55" diameter, high advance ratio propeller with composite blades and an aluminum hub. A propeller cone was designed to improve the aerodynamic performance of the airplane by faring the base of the propeller hub. A propeller tilting mechanism was designed to increase safety in flight by helping in deep stall recovery. This

system tilts the propeller generating a vertical thrust component, which results in a nose down pitching moment. This feature will be further discussed in Section 12.7. The propeller design and performance will be described in detail in Section 8.2.

5.8 Electric Motor

Azalzan is powered by a Yuneec PowerDrive60 DC brushless electric motor for aerospace applications. It is capable of producing a maximum of 80 *hp*. and 240 N·m of torque at 2,400 RPM. It is designed to operate at a voltage of 166 V and current of 340 A. It is essentially an air-cooled electric motor, which dissipates 3,000 W of heat yielding an overall mechanical efficiency of 90%. It requires an airflow rate of 1.2 kg/sec. rate at cruise to maintain its optimal operating temperature, which is provided by a dedicated S-duct located on the upper side of the fuselage. The electric motor weight is 66 lb. and requires a power management unit to regulate its voltage and current at different RPMs. The power control unit is installed in the dorsal electronics bay and occupies 170 in.³ of volume. The electric motor is installed via a simple truss in the mid fuselage section and can be accessed from a dedicated access panel from below. Figures 17 and 18 present the electric motor as installed inside the fuselage. The power from the motor is transmitted to the propellers through a gearing system comprised of one central and two wing-mounted bevel gears. The main driveshaft is 90" long, 7/8" diameter and made of SAE 4131 steel.

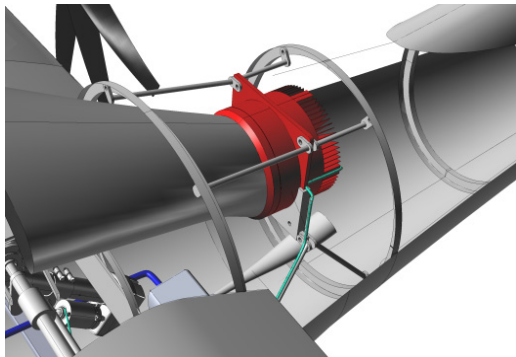


Fig. 17 Electric Motor Integration attached to fuselage frames

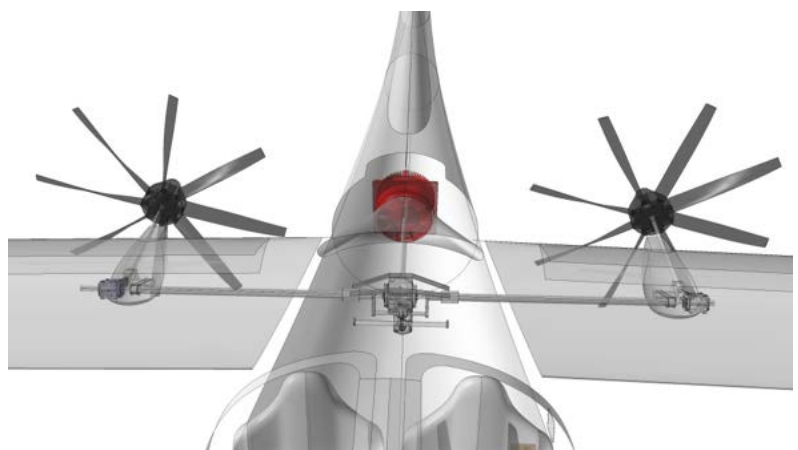


Fig. 18 Propeller-Drive Shaft integration

5.9 Landing Gear

Azalzan utilizes a tri-cycle landing gear equipped with 5.00-5" main tires and a 5.00-4" nose tire. A tri-cycle configuration was selected over a tail wheel configuration given its better ground handling characteristics as well as improved takeoff visibility. The main and nose tires can withstand maximum operating loads of 800 *lb.* and 700 *lb.*, respectively²¹. The nose landing gear is equipped with a steering mechanism directly linked to rudder pedals. Both of the main landing gears are equipped with a closed circuit hydraulic brake system, each individually controlled by brake cylinders coupled with the rudder pedals. A detailed description of the steering and braking systems is given in Sec. 10.4.

The suspension for the main landing gear is provided via a set of leaf springs made of 4130 low-carbon steel designed to absorb landing impact energy resulting from a sink rate of up to 10 *ft./sec.* The leaf spring is attached to the main structure via a carbon-fiber composite bracket that is mounted to two dorsal frames in the fuselage. Nose and main landing gears are equipped with fairings for the purpose of reducing drag as well as controlling their tire spray, which is discussed in detail in Sec. 10.1. Figures 19 and 20 present the landing gear arrangement and a detail of the nose wheel turning, respectively.

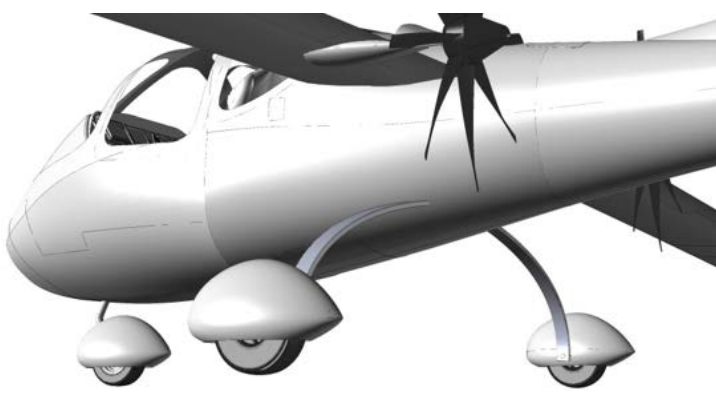


Fig. 19 Landing gear arrangement

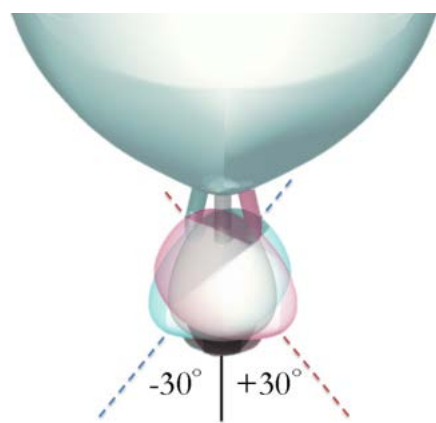
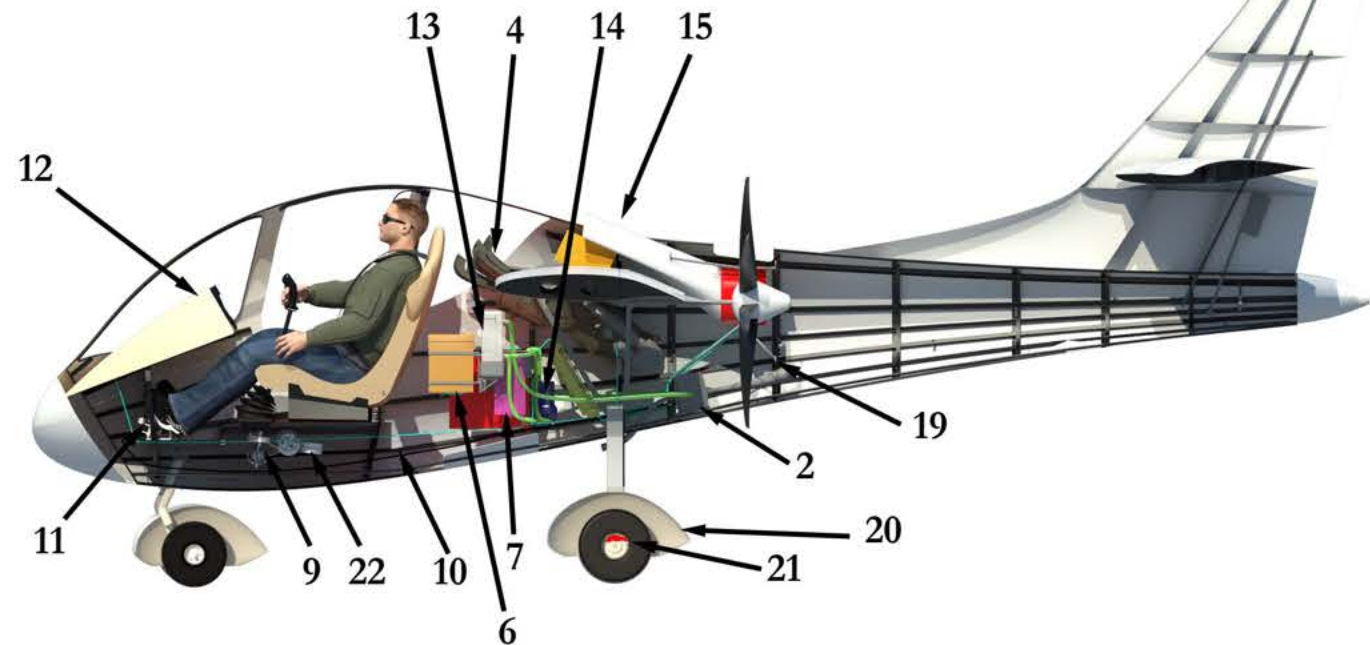
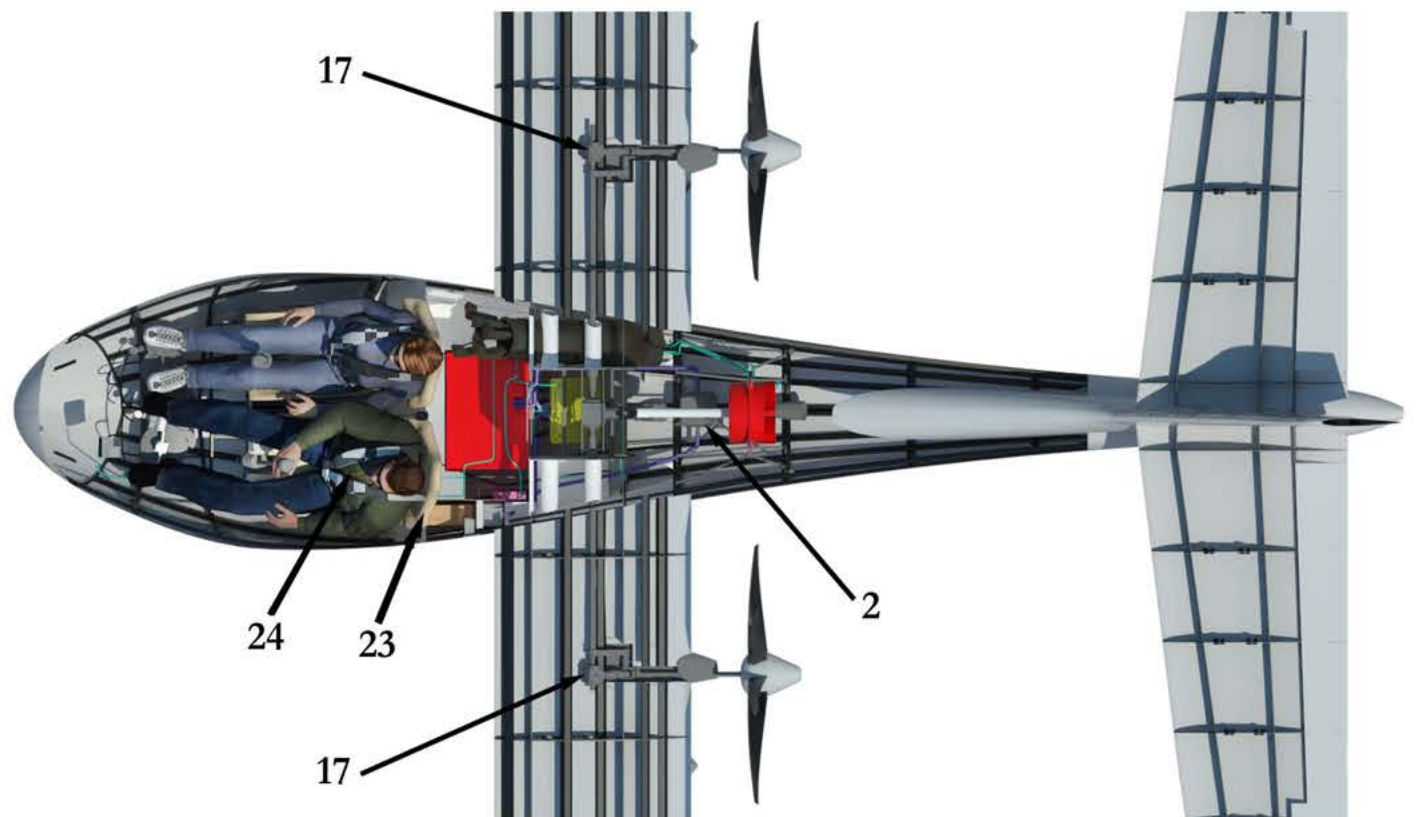
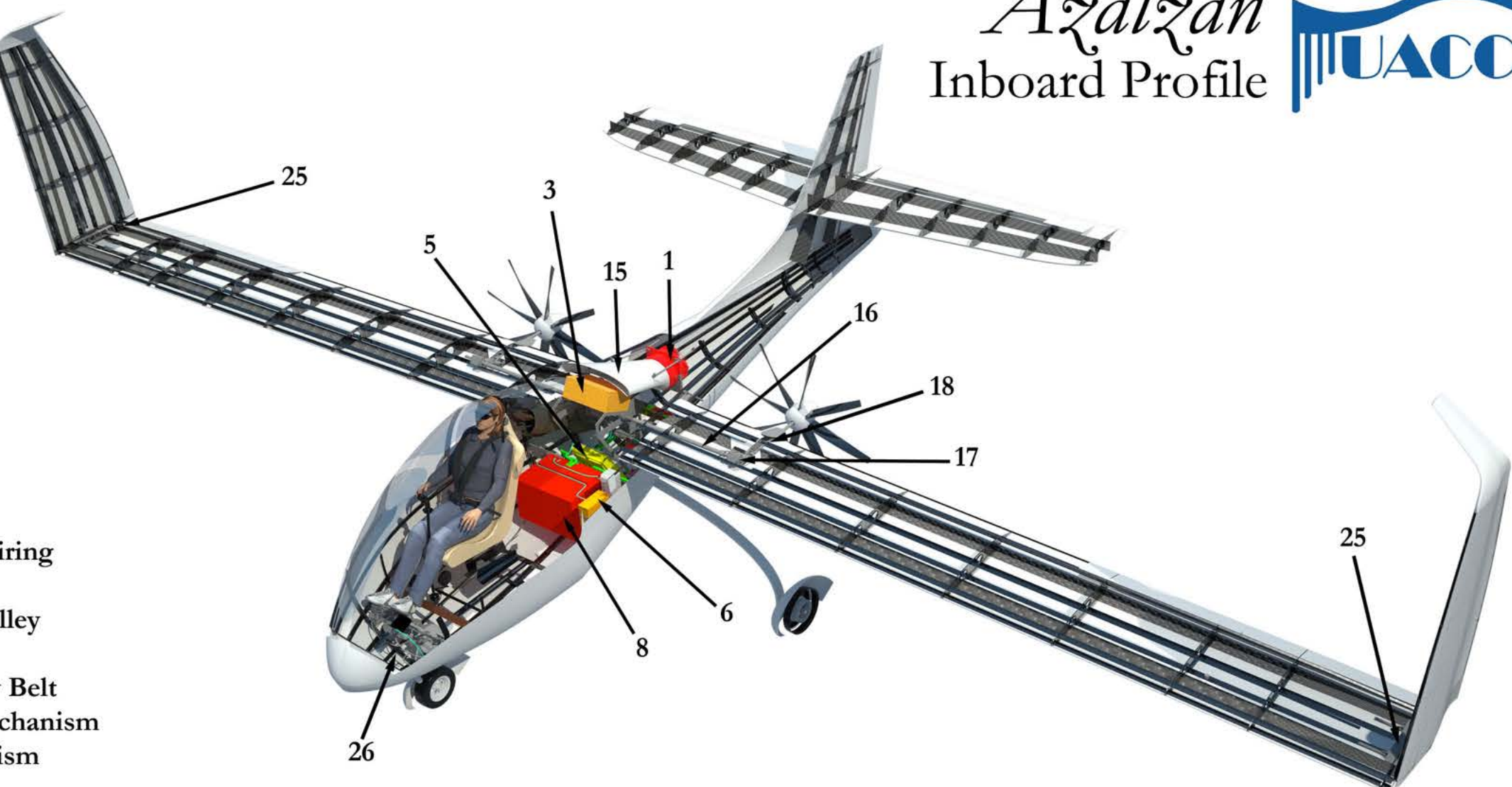


Fig. 20 Detail of nose wheel turning



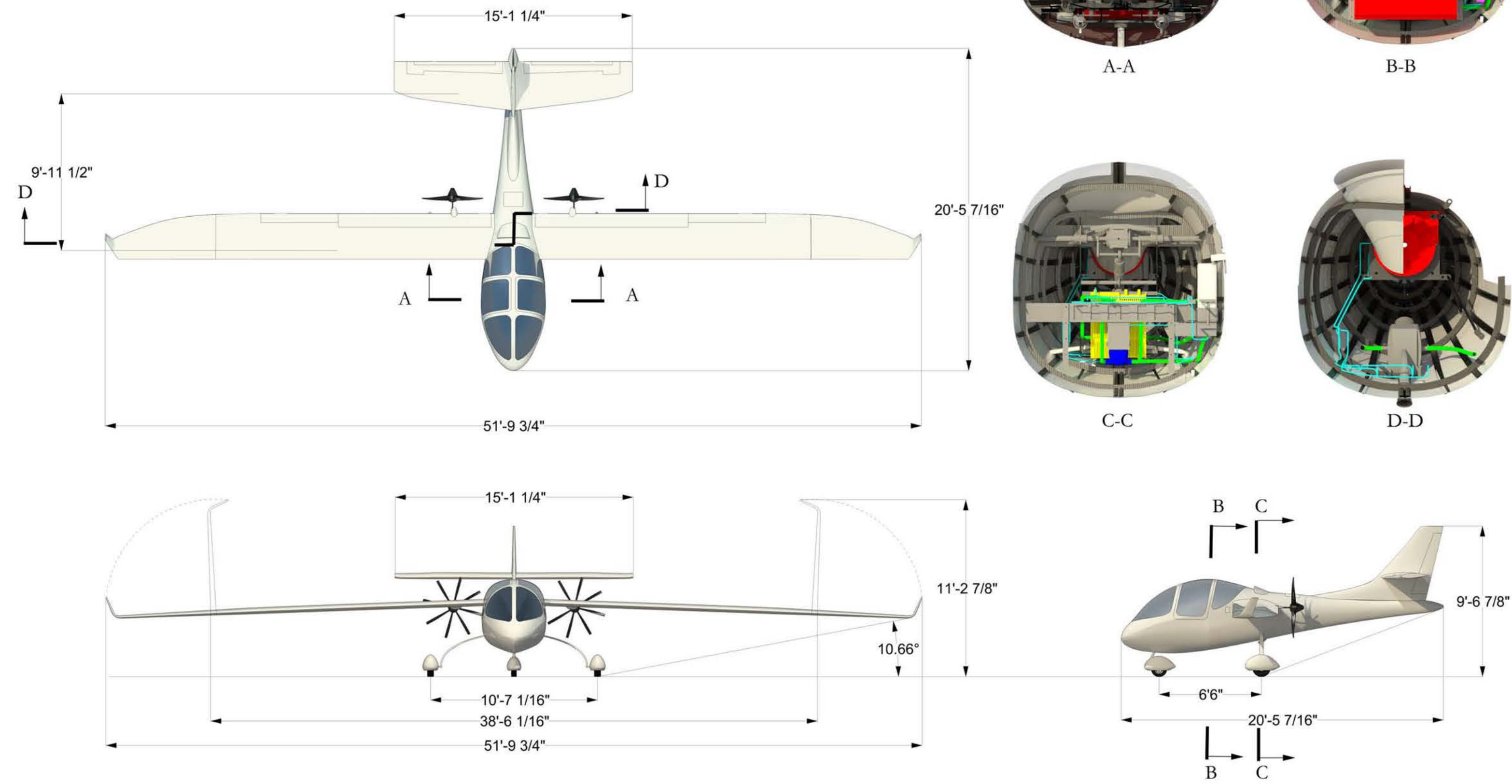
- 1. 80 hp Electric Motor
- 2. Battery Heat Exchanger
- 3. Recovery Parachute Pack
- 4. Golf Club Bag
- 5. Motor Controller Unit
- 6. Battery Charger Unit
- 7. DC-DC Converter
- 8. Li-Air Battery
- 9. Control System
- 10. Brake Line
- 11. Rudder Pedal
- 12. Dashboard
- 13. Coolant Reservoir
- 14. Coolant Pump
- 15. Air Inlet
- 16. Drive Shaft
- 17. Gearbox
- 18. Propeller Shaft
- 19. Motor Mount
- 20. Landing Gear Fairing
- 21. Brake Calipers
- 22. Control Cable Pulley
- 23. G-Seat
- 24. Four Point Safety Belt
- 25 Wing Folding Mechanism
- 26. Steering Mechanism



Azalzan
Inboard Profile 

Azalzan

Three view and cross-sections.



6.0 Aerodynamics

6.1 Airfoil Design

The method for selection of airfoil profiles was dictated by two main criteria. First, in order to maximize the extent of natural laminar flow on the upper surface (thus reducing friction drag), the selected airfoils needed a favorable “rooftop” shape pressure coefficient distribution²². Second, the airfoil geometry must have moderate pitching moment coefficients to avoid larger horizontal tail planform areas required to balance the aircraft. In order to obtain a reasonable baseline airfoil, a study of 15 low Reynolds number, natural laminar flow airfoil geometries (available on University of Illinois at Urbana-Champaign’s²³ web portal) was conducted. The airfoils were analyzed using the *DesignFoil* software on the merit of the maximum extent of laminar flow at $C_L = 0.65$ (selected in section 2.1). Figure 21 presents a summary of the airfoil selection.

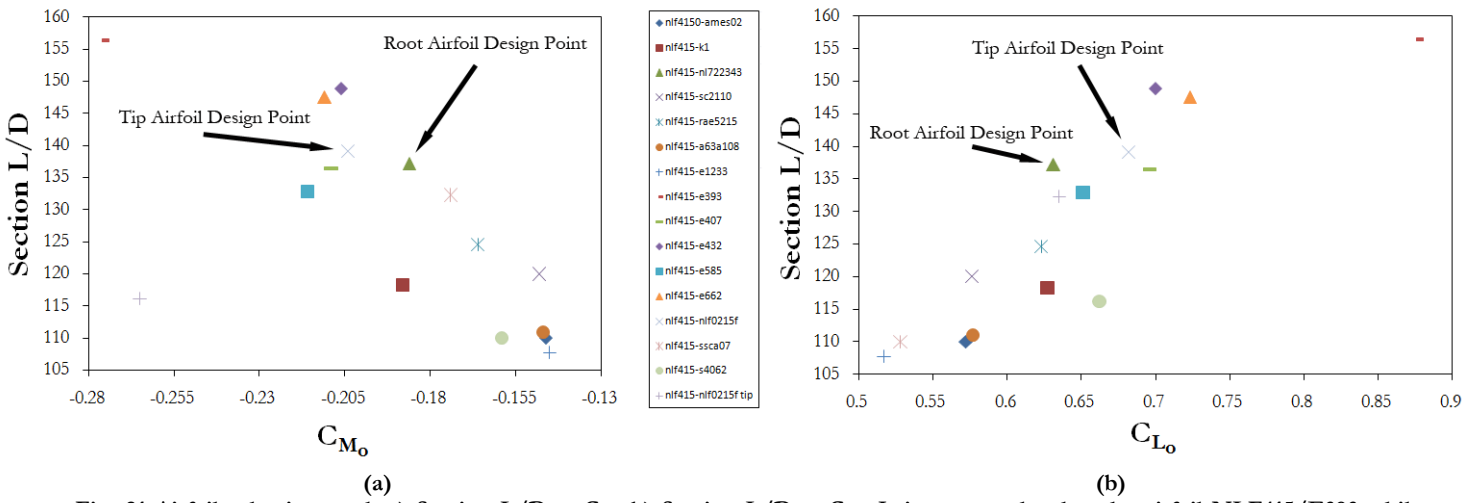


Fig. 21 Airfoil selection pool. a) Section L/D v. C_{M_0} b) Section L/D v. C_{L_0} . It is noteworthy that the airfoil NLF415/E393 while having outstanding L/D and C_{L_0} performance, attains too large of a moment coefficient, making it unsuitable as a wing airfoil.

Using these airfoils, multiple combinations of upper and lower surface curves were analyzed in order to select the best performing combination. NASA Langley’s NLF-415 was selected as the upper airfoil profile for both root and tip. The NL722343 was selected for the lower root airfoil profile and NLF 0215F was chosen for the lower tip airfoil profile. Camber adjustment was performed on the root and tip airfoils to increase their section cruise L/D. As the extent of laminar flow plays a significant role in airfoil performance, CFD analyses (using *ANSYS CFX*) were then performed to verify the locations of transition to turbulence as well as general airfoil characteristics.

Figures 22 and 23 present a summary of the results of the CFD analyses performed on the root and tip airfoils.

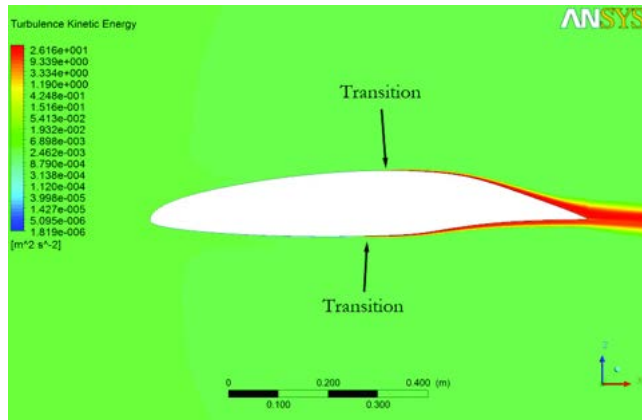


Fig. 22(a) Root airfoil turbulent kinetic energy

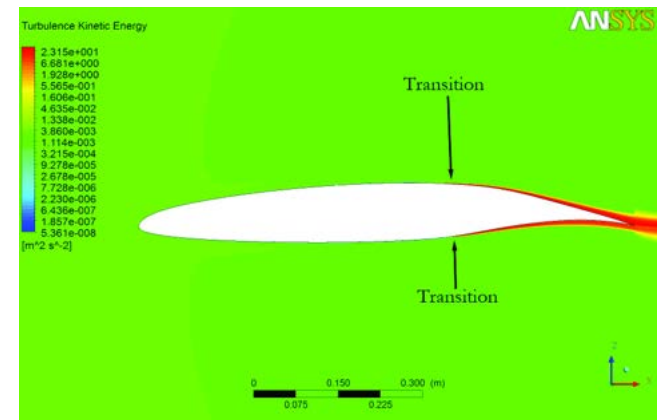


Fig. 23(a) Tip airfoil turbulent kinetic energy

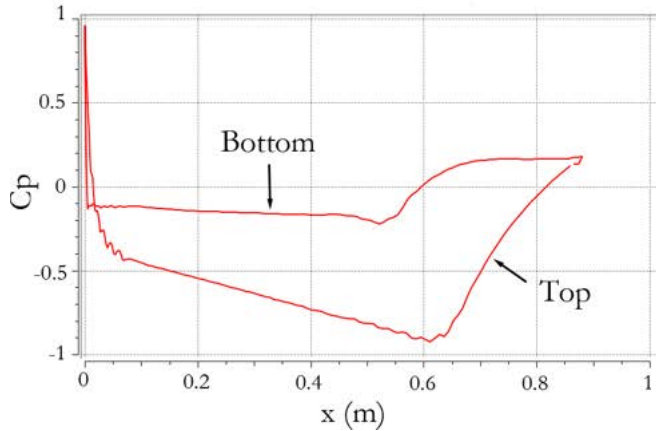


Fig. 22(b) Root airfoil pressure coefficient plot

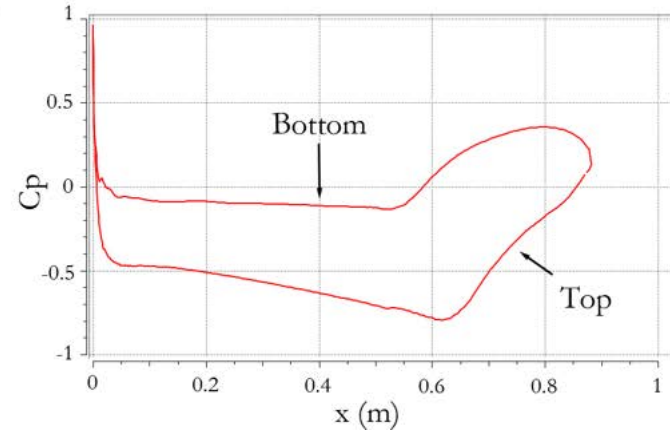


Fig. 23(b) Tip airfoil pressure coefficient plot

CFD analyses were performed on tip and root airfoil profiles to determine the location of the transition to turbulence. The analyses are simulating the stream wise flow speed of 80 *kts.* with ISA atmospheric conditions at 9,500'. The chord length selected for the analysis corresponds to the final wing planform geometry. A structured mesh was constructed and refined near the boundaries according to y^+ rules for modeling transition. A shear stress transport turbulence model was coupled with a γ - θ transitional model. The sand roughness and geometric roughness were prescribed to be $0.509016 \mu\text{m}^{24}$ and $0.05 \mu\text{m}^{25}$ respectively. As it can be observed from the pressure plots, the airfoils feature a “rooftop” shape pressure coefficient plot, indicating the existence of favorable pressure gradients for a large portion of the airfoil chord.

6.2 Wing Planform Optimization

As presented in Sec. 4.1, one of the first steps in determining the general dimensions of Azalzan was to establish the wing aspect ratio. Using the results of the preliminary drag analysis, it was determined that a high aspect ratio wing would maximize range for the longest flight segments

(cruise and loiter). After a detailed drag analysis was performed on Azalzan, it was possible to make a more detailed study on the effect of AR on the overall performance and efficiency of the aircraft.

The aspect ratio directly affects the aerodynamic performance of the aircraft, as it has a direct effect on reducing the induced drag. A lower induced drag results in a lower required power and, for the same battery, a longer range. However, a very large aspect ratio might result in undesirable aeroelastic flutter which can have catastrophic effects on the structure. Therefore, it is important to optimize the AR for both performance and safety reasons. A detailed sensitivity study was made, following the process described in section 4.1, using the results of the detailed drag analysis. The results of this study are summarized in Fig. 24. As in the preliminary study, the optimum AR value is achieved as the value of the derivative $\partial R / \partial AR$ is close to zero. If range was plotted against aspect ratio, a maximum range would occur at this value of AR. However, the derivative reaches zero at a very high AR (~ 21), resulting in structural problems associated with wing flutter. Therefore, a value of 18.35 was selected as the final design point for the AR of the wings, signifying a synthesis between airplane performance and airframe safety. Given the wing area of 136.3 ft^2 , a wingspan of 50' is obtained for Azalzan. Since this span is longer than the width of the 40' T-Hangars required by the RFP, UACC has decided to implement a wing folding mechanism, which will be described in Secs. 7.4 and 14.1.

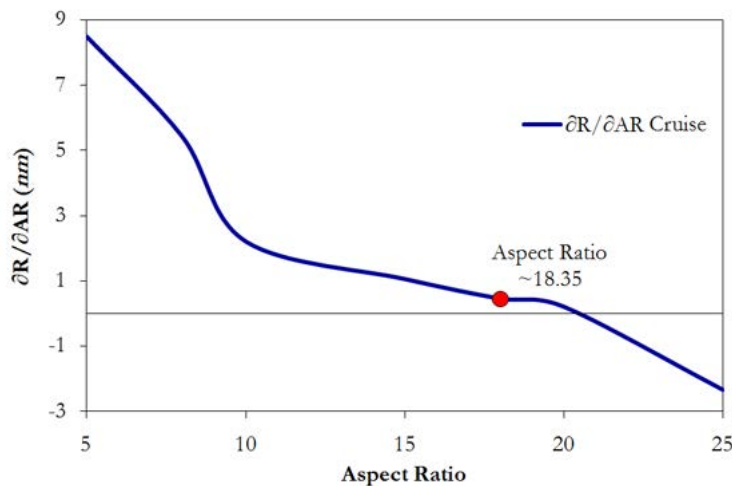


Fig. 24 Results of Aspect Ratio analysis using a detailed drag analysis. For simplicity, the results of loiter are not shown since its $\partial R / \partial AR$ derivative did not change significantly. Wing aspect ratio selected as 18.35.

6.3 Winglets

To improve the aerodynamic efficiency of the wing and lower the lift-induced drag, winglets were implemented into Azalzan. Particular attention was paid to the loft generated between the wingtip chord and the winglet root to ensure a smooth transition preventing adverse effects that may arise from rapid curvature changes near the wingtip²⁶. The PSU 94-097 airfoil was selected for the cross-section of the winglets because it is specially designed and optimized for the purpose of minimizing interference with the wing pressure field. Additionally, it helps to maximize the wing's yawing moment coefficient, therefore assisting in the overall lateral directional stability of the aircraft²⁷. Figure 25 presents a CFD analysis of the local pressure distribution on the winglet airfoil. Given that the winglets are installed at the tip of a relatively high aspect ratio wing, it was decided that they should be manufactured using lightweight and stiff carbon-fiber honeycomb materials to reduce their adverse effects on wing flutter. Figure 26 presents the final integrated geometry of the winglets.

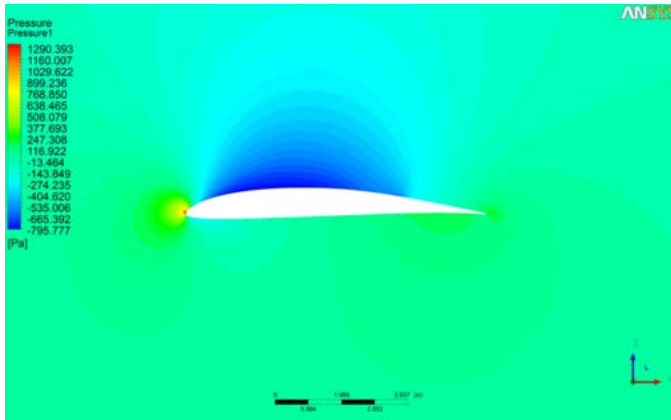


Fig. 25 CFD analysis of the local pressure distribution on the winglet airfoil

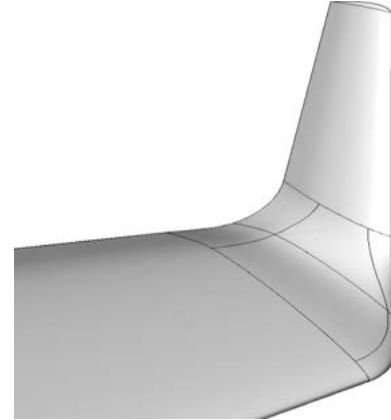


Fig. 26 Winglet geometry

6.4 High Lift Devices

The strategy to maintain maximum laminar flow on the wing surfaces dictated that no moving part on the leading edge should be incorporated. This led to the decision to incorporate only the most efficient trailing edge devices that can generate a $C_{L_{max}}$ up to 2.0, as was assumed in Sec. 2.5, given that the flap will extend to 76% of the wing half-span (as dictated by the location of the wing folding line).

Reviewing the ESDU Data Item 95021²⁸, it was determined that a set of single-slotted Fowler flaps would generate sufficient lift for this purpose.

Using Roskam's²⁹ method for sizing flaps, a parametric study was performed to determine the required flap chord to wing chord ratio that will generate sufficient $C_{L_{max}}$ at takeoff and landing.

Figure 27 shows the results of this analysis for flaps having a streamwise extent between 15% and 35% of the wing chord. In order to evaluate the combined effect of the flaps and the propeller tilting a low speed, steady-state CFD analysis was performed. to verify the

attachment of flow, as well as a maximum section lift coefficient exceeding 6.5, attained at landing conditions with a flap deflection and thrust vector of 40°. Figure 28

presents the results of this analysis as velocity contours and pressure gradients.

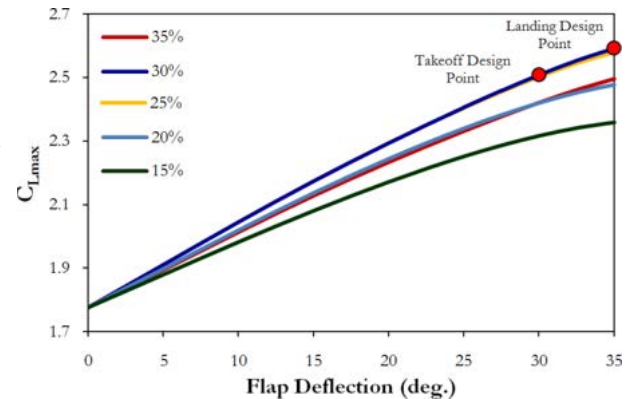


Fig. 27 Aircraft maximum lift coefficient vs. flap deflection for different flap chord to wing chord ratios. The takeoff position of 30° and landing flap setting of 35° are indicated. No power effects are taken into consideration

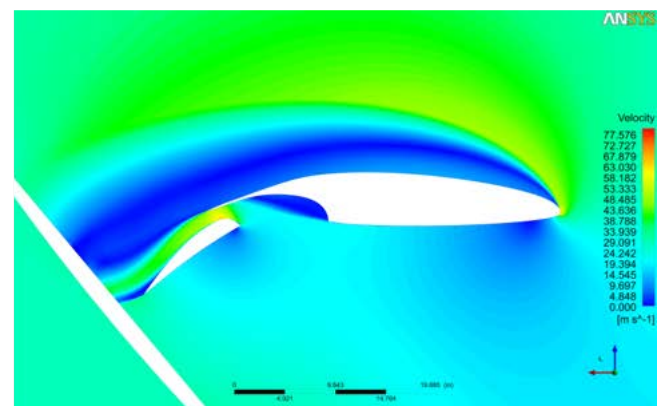
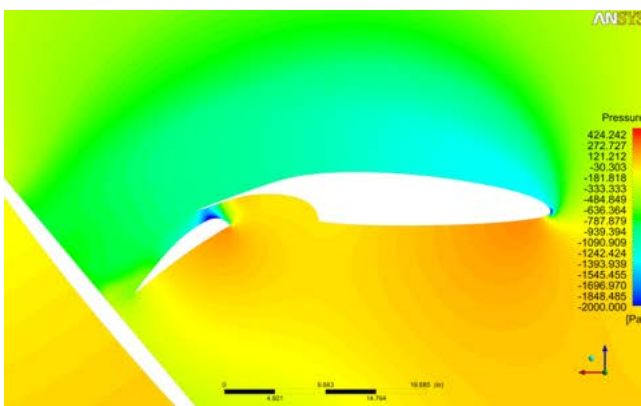


Fig. 28 CFD analysis on wing section with flaps, at landing conditions with a flap deflection of 40°, including the effect of the tilted propeller. Left displays velocity contours and Right displays pressure gradients.

6.5 Wetted Area Distribution

To perform detailed Class II³⁰ drag estimations, a precise measurement of the wetted area of the airplane was necessary. This was accomplished after initial CAD surface models for the configuration were finalized. The areas were extracted numerically with high precision tools and

were used in the drag calculations that are presented in the sections to follow. Table 5 and Fig. 29 summarize the result of the wetted area distribution analysis.

Table 5 Summary of Wetted Area Distribution analysis

Component	Wetted Area (ft^2)	% Total
Fuselage	153.98	24.50
Wing	316.86	50.42
Winglets	5.37	0.85
Horizontal Tail	82.18	13.08
Vertical Tail	38.5	6.13
Intake	8.03	1.28
Landing Gear Strut	6.49	1.03
Landing Gear Faring	13.60	2.16
Tires (Exposed)	3.40	0.55

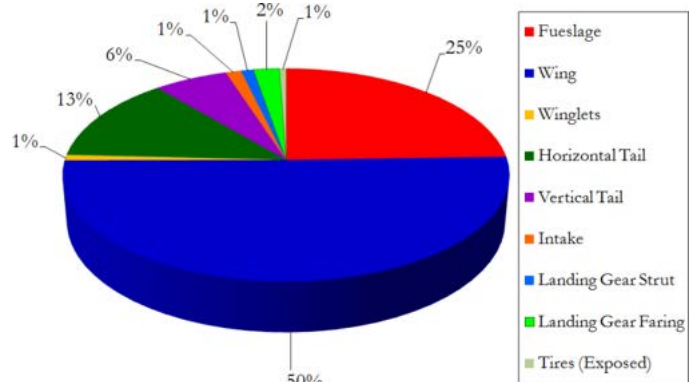


Fig. 29 Pie Chart Representation of Wetted Area Distribution

6.6 Detailed Drag Polars and Breakdown

To obtain a more accurate estimate of the lift and drag forces, a detailed analysis of the aerodynamics of the aircraft was performed using the methods presented by *Roskam*³¹. The high lift drag polar methodology is adopted from *Torenbeek*³² and used to correct the nominal drag polars to account for drag due to deployed flaps at takeoff and landing. The results of the airfoil CFD analysis related to the verification of the extent of laminar flow, presented in Sec. 6.1, were used to compute the wing drag. Figure 30 presents the results of detailed drag analysis using 5th order drag polar equations, which will be used later in Ch. 13 to verify the satisfaction of performance requirements.

Figure 31 presents the drag breakdown of Azalzan at cruise conditions.

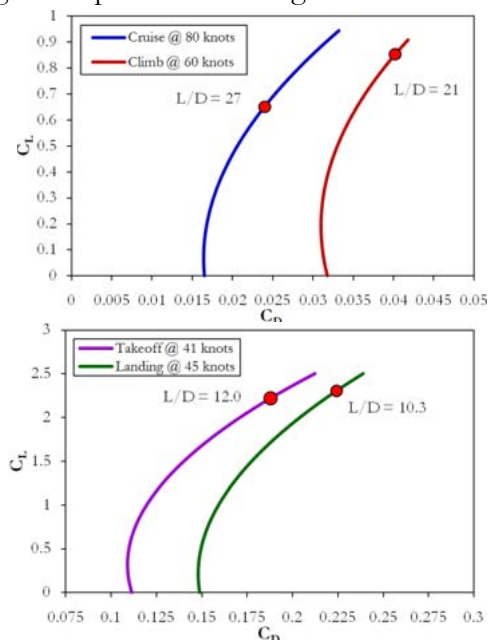


Fig. 30 Drag Polars @ Takeoff, Climb, Cruise, and Landing

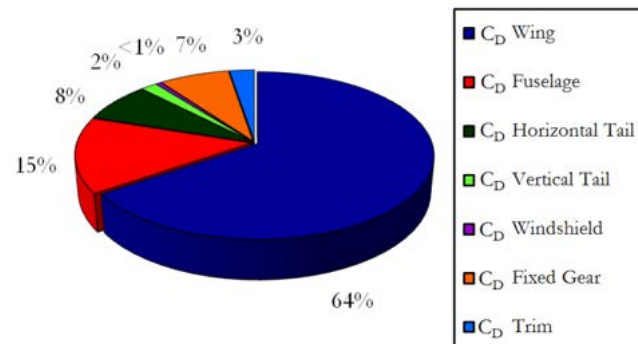


Fig. 31 Drag Breakdown @ Cruise

6.7 Full Airplane CFD Drag Verification

CFD analysis were performed to validate the feasibility of maintaining natural laminar flow on the surfaces of the airplane, as well as evaluating the parasite drag contribution of various components and the thrust generated by the accelerated and heated air exiting the fuselage from the heat management system.

A NURBS model of the aircraft's exterior surfaces was placed within the analysis domain presented in Fig. 32. Simplifications were made to allow for proper meshing of the full aircraft geometry with available computational resources.

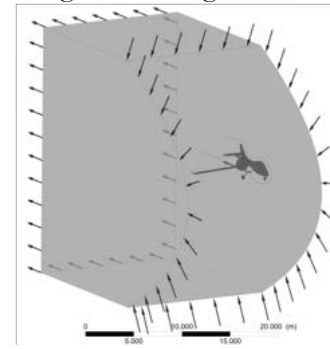


Fig. 32 CFD Domain analysis

Both air intakes were removed and control surface gaps were not modeled to allow for efficient meshing of the geometry. Then, using ANSYS ICEM CFD, the surfaces were meshed using an all-tri patch conforming surface mesh, with size controls place on each surface, as shown in Fig. 33. After the placement of volumetric element control regions, an all tetrahedral mesh was grown from the surfaces using a Delaunay algorithm in order to fill the volume with elements. In order to properly capture the boundary layer with enough detail to analyze the transition to turbulence, prism elements were grown from the surfaces into the volume mesh. With an aim of achieving a $y^+ < 7$, 15 prism layers were grown, with a first element height of 0.05 mm, the boundary layer elements can be seen in Fig. 34.

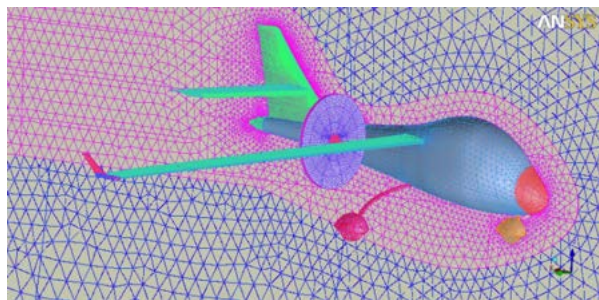


Fig. 33 All-tri patch conforming surface mesh

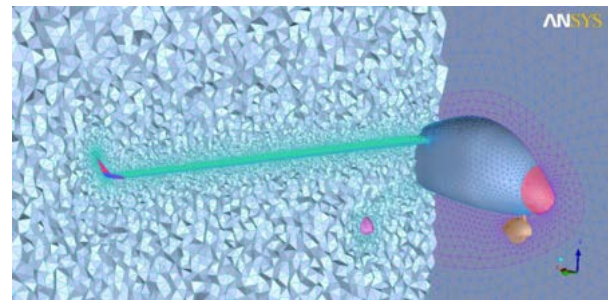


Fig. 34 tetrahedral volume mesh

This resulted in 8,706,320 elements connected by 2,591,791 nodes, with 5,091,445 elements being tetrahedral and 3,348,237 elements being prisms. Figure 35 shows a detailed view of the final mesh composition on lifting surfaces.

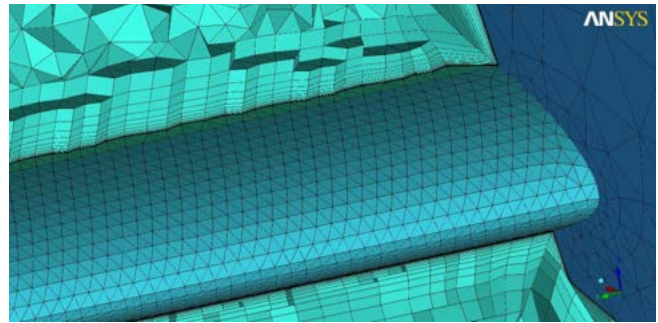


Fig. 35 Prism volume mesh refinement to capture boundary layer features.

ANSYS CFX-pre was used to apply appropriate boundary conditions on the model and to configure the solver for a steady-state analysis. The atmospheric conditions were set to those at cruise with a pressure of 69,674 Pa, temperature of 27.9 °F, and a flow field velocity of 107.4 *kta*s. Turbulence was modeled using a high resolution shear stress transport model with γ - θ transitional turbulence, which allowed for the prediction of the transition from laminar to turbulent flow on the surface of the aircraft. No-slip boundary conditions were applied to all airplane surfaces, assuming a sand roughness of $0.51 \mu m^{33}$, and a geometric roughness height of $0.05 \mu m^{34}$. The geometric height was used to correlate the transitional turbulence model. Both these heights correlate to a polished surface. The effects of the propeller were modeled using the results presented in Sec. 8.2 for the propeller's flow field on a disk shaped boundary. The exit flow from the thermal control system was modeled as a mass flow from the end of the tail cone.

The analysis was then performed using ANSYS CFX solver installed on a 64 *bit* computer with an eight core Intel i7 Q 720 processor clocked at 1.6 *GHz* and allocating 8 *Gb* of RAM. The analysis was converged to RMS values below 10^{-3} over 100 iterations, which took about 6 hours.

The result of the analysis was then post processed using ANSYS CFX-post module. Pressure coefficient and kinetic energy plots were generated to verify the existence of favorable pressure gradient on the external surfaces of the aircraft, as well as attachment of the flow, and turbulence transition locations. Figures 36 through 38 present the highlights of these results.

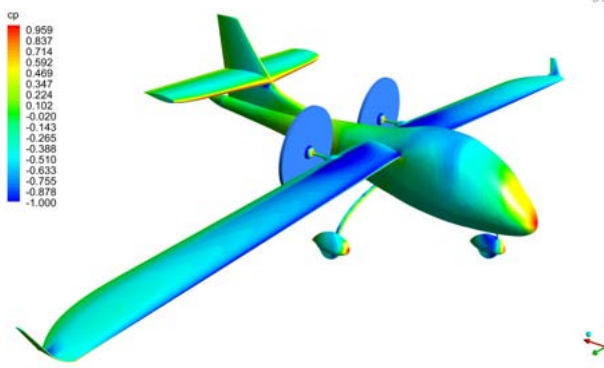


Fig. 36 Pressure Coefficient contour plot at Cruise

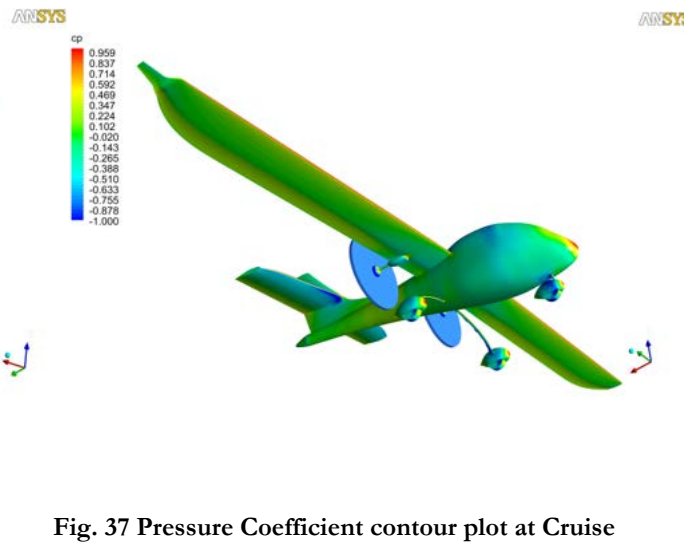


Fig. 37 Pressure Coefficient contour plot at Cruise

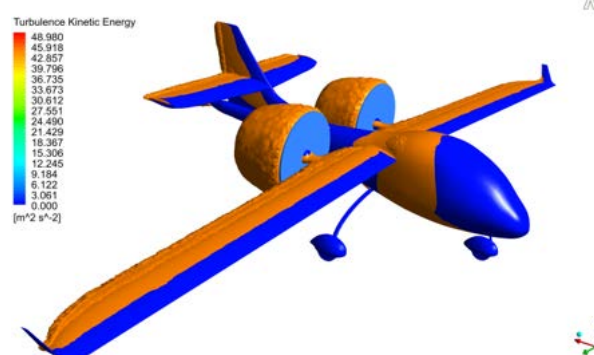


Fig. 38 Turbulence Kinetic Energy

As it can be seen in Figs. 39 and 40, the wing surfaces have substantial extents of favorable pressure gradient, so the lower surface of the wings are maintaining 70% of planform wetted area in laminar flow, while the upper surface maintains an average value of 60% laminar flow.

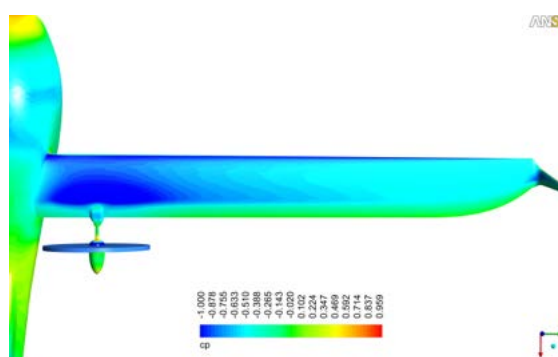


Fig. 39 Pressure Coefficient contour top

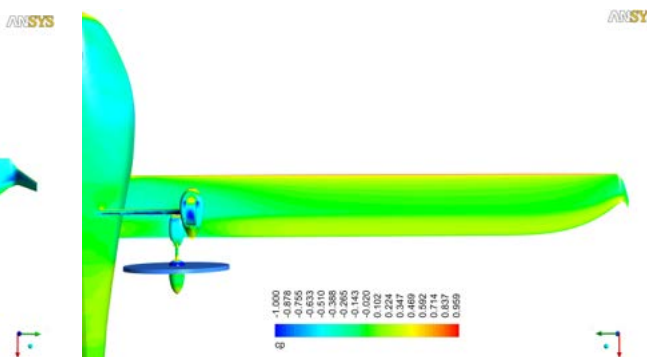


Fig. 40 Pressure Coefficient contour bottom

The fuselage forebody is also capable of maintaining significant amounts of laminar flow, estimated to cover 25% of the fuselage wetted area. This is assuming that transparency and door sealing is done with adequate precision to prevent the tripping of the surface flow and the door and transparency edges.

Integrating shear forces acting on various surfaces of the aircraft, the breakdown of the total parasite drag was obtain and is shown in Fig. 41.

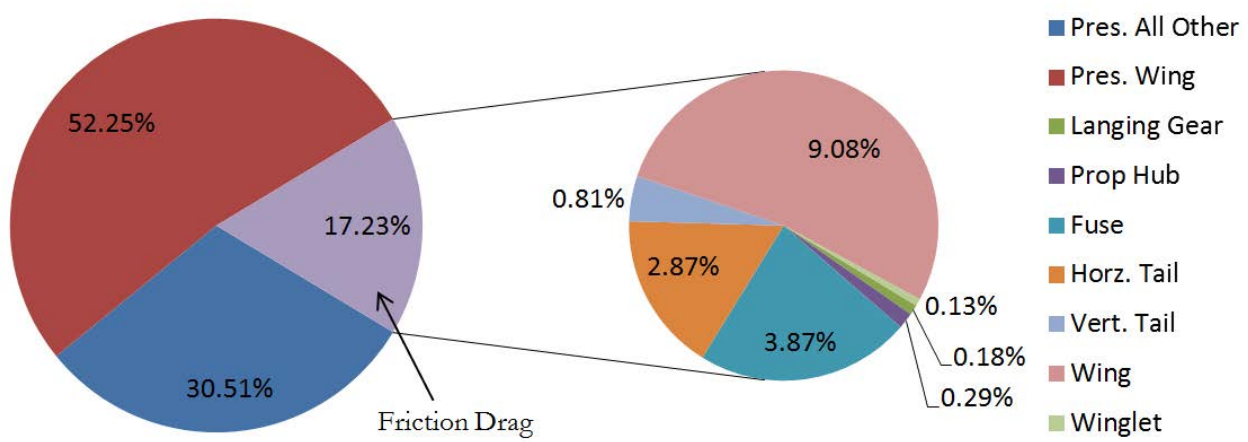


Fig. 41 Breakdown of total parasite drag

7.0 Structural Analysis

7.1 Loads V-n Diagram

In order to obtain the maneuver envelope for Azalzan, the guidelines provided by FARs for general aviation aircraft were adopted due to the lack of directly applicable design codes for S-LSAs. The maneuver envelope was constructed using guidelines provided by FAR §23.335 to determine the critical case load factors for the structural design process of Azalzan. This study indicated that the airframe is to be designed for a positive pull-up load factor of 3.8 g to occur at 88 keas at 9,500' and a negative push-over load factor of -1.52 g to occur at speeds between 55 and 83 keas. It was determined that the maneuver speed of Azalzan is 85 keas. The dive speed at cruise altitude is computed to be 117 keas.

The shear and bending moment diagrams for wing and fuselage were computed along Libove's principal axes³⁵ to perform structural analysis and sizing using AAA's load module, which computes the total load by taking into account aerodynamic and dynamic loads in addition to concentrated and distributed weight sources on the lifting surfaces and fuselage structures. To accomplish this analysis, the aerodynamic loads acting on the wing structure were estimated using various high order methods presented in ESDU Data Item 8304072, the result of which is shown in terms of lift, drag, and moment diagrams in Fig. 42. The moment coefficient plotted is computed around the elastic axis of the wing considering both lift and twisting forces acting on the structure.

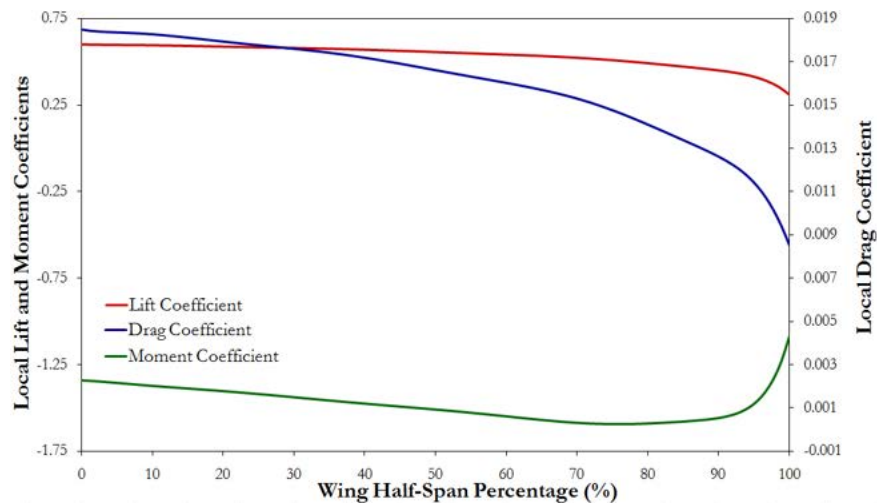


Fig. 42 Wing Loading

The loads acting on the wing structure were calculated by considering both the derived distribution of lift and drag forces as well as the torsional moment acting on the wing structure. The total acting forces and moments on the wing were computed by summing the aforementioned aerodynamic forces with the concentrated weight of the wing structure. These values were multiplied by a load factor of 3.8 to comply with the critical loading cases predicted by FAR §23.337.

The final V-n diagram is shown in Fig. 43.

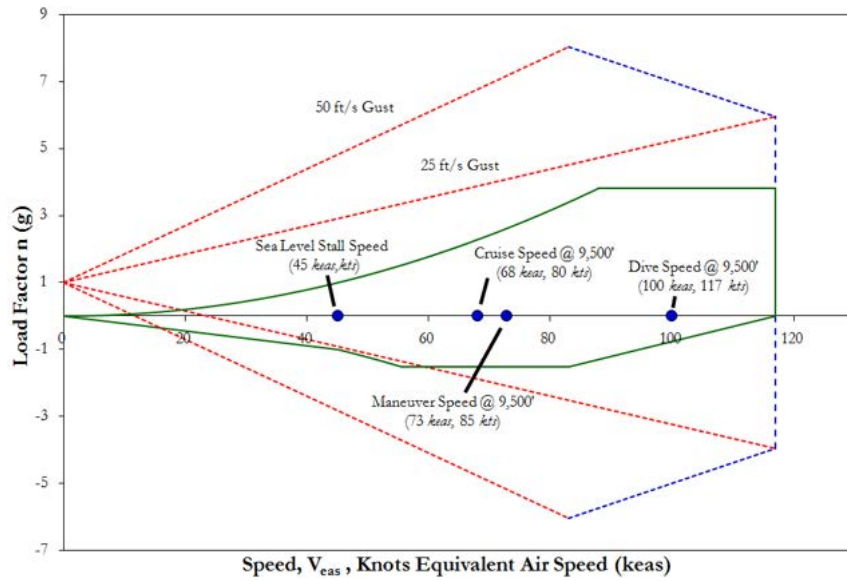


Fig. 43 Maneuver Envelope

7.2 Fuselage Structure

The structure of the fuselage consists of three major sections that are manufactured using carbon-fiber reinforced plastics (CFRP) with varying thickness depending on the longitudinal station of the section. Figure 44 presents the structural breakdown of the sub-assemblies of the fuselage.

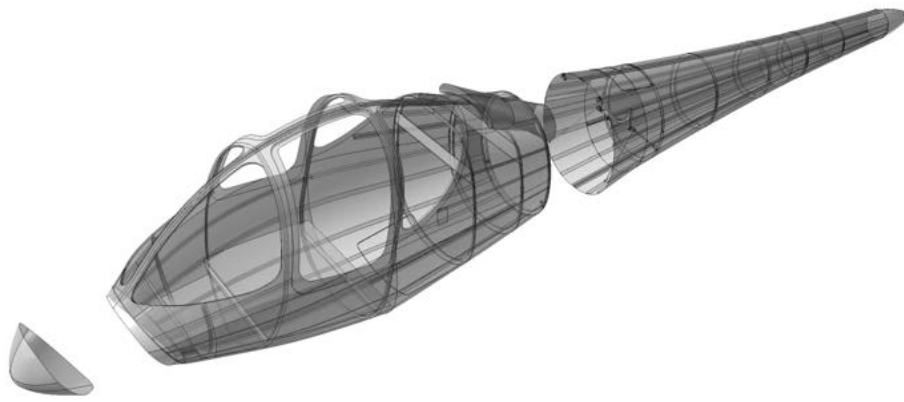


Fig. 44 Fuselage Structural Isometric

The outer skin is stabilized by adhesively-bounded longerons made from CFRP. The major sections of the fuselage are connected to each other via titanium links. There are also longitudinal floor beams along the cockpit that provide a base for the installation of seats as well as increased stiffness of the cockpit to improve crash survivability. Fuselage frames adjacent to cockpit doors are inclined to serve a dual purpose of stiffening the door edges and provide crash protection for the occupants along the axis of the seats. The cockpit and occupants are separated from dorsal and aft sections of the fuselage by an aluminum firewall, which also acts as cargo stowage. The wingbox extends into the main fuselage and is attached to reinforced frames via fasteners. The landing gear is also connected to the main wingbox by a carbon-fiber composite mount, which is fastened to the rear spar of the center wingbox. Figure 45 presents a view of the 3D CAD model constructed for the fuselage structure highlighting its main features.

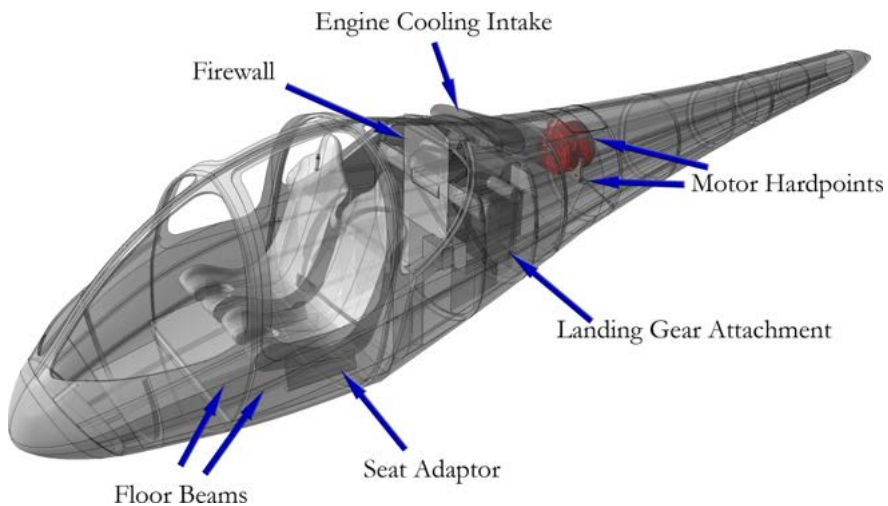


Fig. 45 Fuselage Structural Highlights

7.3 Landing Gear Attachment and Structure

The landing gear struts were designed to withstand a 10 ft./sec. sink rate as suggested by Roskam³⁶. FEA analysis was utilized to optimize the geometry of the landing gear struts as well as their attachment points on the main structure. Low-carbon steel SAE 4130 was selected due to its high yield strength and good fatigue behavior. Figure 46 presents the results of the FEA optimization of the landing gear struts.

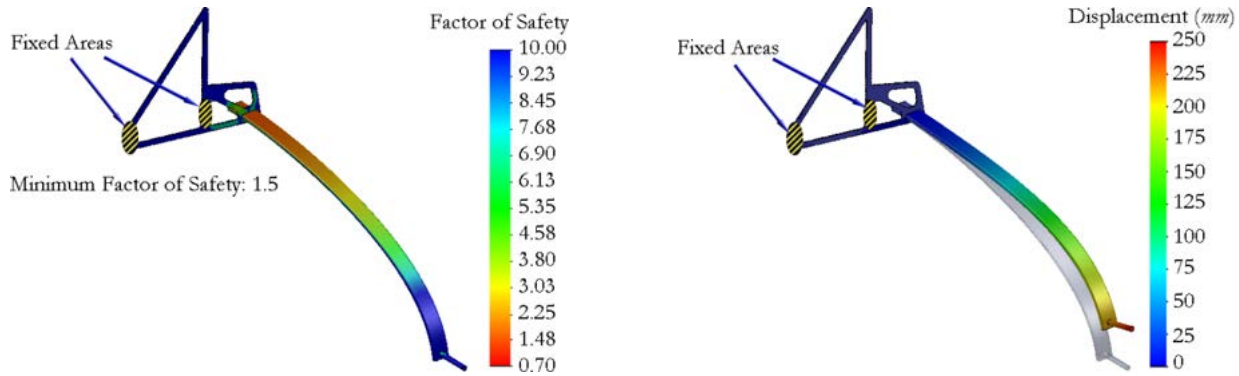


Fig. 46 Factor of Safety and Displacement results of FEA analysis on landing gear struts

7.4 Wing Structure

The wing structure of Azalzan presents a number of unique features that require novel design solutions. First, Azalzan is designed to take advantage of maximum NLF on the surface of the wing to reduce airframe drag. However, slightly misaligned edges can trip the boundary layer causing unfavorable drag-increasing turbulent flow on the surface of the wing. Therefore, the wing skin structure is constructed from two single-piece, polished skin panels on the upper and lower surfaces to minimize the potential of misaligned skin panel edges, which is more likely to occur with multiple skin panels per surface. According to *Oberg et. al.*³⁷, achieving a geometric roughness of $0.05\mu m^*$ is feasible using modern polishing methods widely available. Second, the large wingspan of the wing planform can render Azalzan incapable of using much of contemporary airport taxiways and hangers, thus UACC has integrated a wing-folding mechanism to allow the airplane to be taxied in narrow taxiways and stored in a T-hanger, as required by the RFP. Lastly, wing flutter was addressed in the design of the high AR wing planform by increasing the number of stiffener elements under the wing skin panels, which was later verified to be effective using numerical methods.

The wing manufacturing methods used for Azalzan are not sensitive to the limitations of the manufacturing methods of an aluminum airframe, which restricts the size of the panels to the maximum overall dimensions of the raw material and the tooling machinery. Utilization of

* The same assumption was applied to the CFD analysis of the wing airfoils presented in Sec. 6.1

composite materials and modern manufacturing technology allows the wing skin panels of Azalzan to be laid up in two continuous pieces, therefore minimizing the potential for misalignment and the resultant turbulent flow experienced on the surface of the wing. Although this manufacturing strategy increases the size of the tooling and autoclaves needed to cure the composites after manufacturing, it improves the potential for maintaining laminar flow on the wing.

The wing super-structure consists of two primary spars, located at 18% and 65% of the chord length, and a series of composite ribs that are spaced on average 30" apart. The upper and lower wing skin panels are attached to the wing super-structure via reinforced brackets located on skin panel stiffeners that are connected to the wing ribs. The trailing edge fowler flaps are an independent structure that is installed on the rear spar. The surfaces of the trailing edge high-lift devices are constructed of composite sandwich panels, which result in a high-strength, low-weight structure. Figure 47 presents a detailed breakdown of the wing structure of Azalzan.

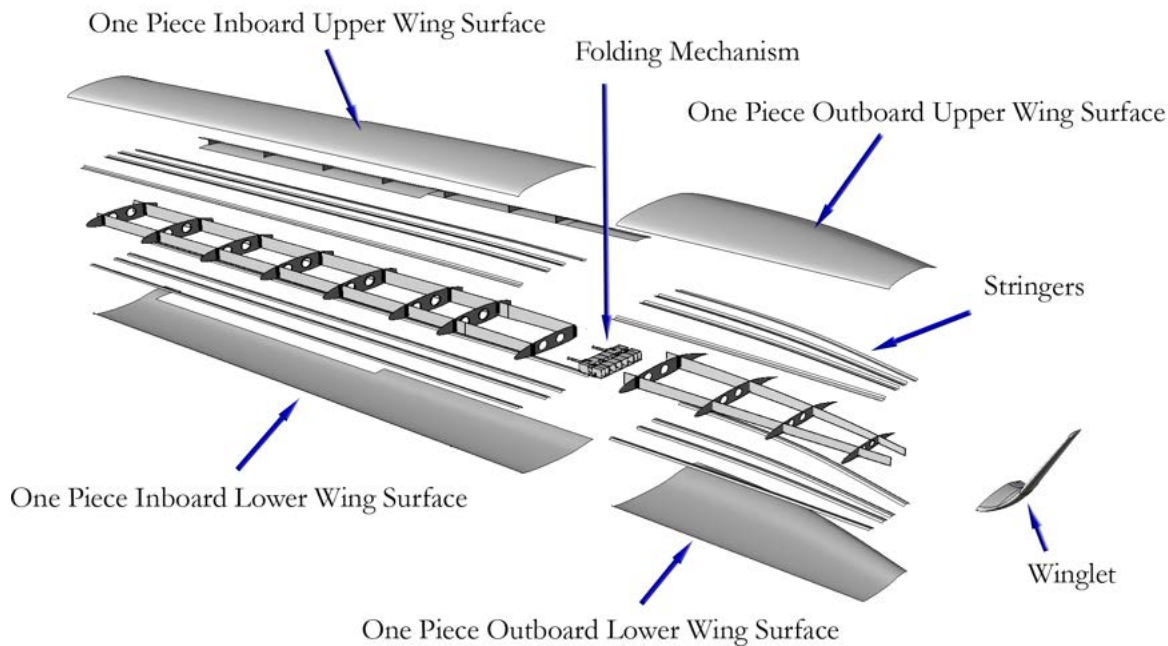


Fig. 47 Wing Structure Breakdown

The wing folding was accomplished through a multi-lug folding device, separating the outboard wingbox from the inboard wingbox and secured on the surfaces of the front and rear spars of the wingboxes, as well as the upper and lower skin panels. The folding is operated using electro-motors equipped with a worm-gearred mechanism and folds between the direction of the dihedral of

the wing and the direction perpendicular to the ground. The folding mechanism is secured before taxi and takeoff by mechanically operated latch pins that are inserted into the connector plate installed on both sides of the folding mechanism. Figure 48 shows the operation of the folding mechanism and Fig. 49 presents a close-up view of the locking mechanism.



Fig. 48 Demonstration of wing folding

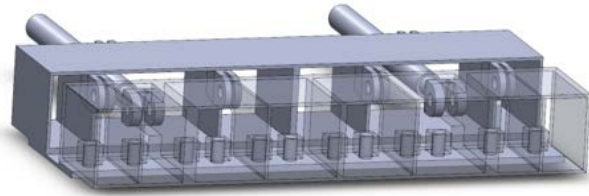


Fig. 49 Close up of wing folding mechanism

7.5 Wing Flutter Considerations

Due to the high aspect ratio of Azalzan, flutter characteristics of the wing had to be considered. Numerous techniques exist for exploring the flutter characteristics of typical aircraft, ranging from pure analytic methods to procedures treating wings as a large set of coupled, damped and driven mechanical oscillators. Typically, these procedures are difficult to implement and do not yield dependable results unless considerable effort is expended to model the structural wing coefficients with as much detail as possible.

In lieu of such procedures, UACC opted for a semi-analytic method that makes use of known flutter velocities for a variety of similar aircraft and maps these flutter velocities to velocities for similar aircraft with the aspect ratio of Azalzan. The procedure is based on a method of flutter analysis given by *Molyneux et al.*³⁸ which gives an analytic method for converting between flutter velocities of craft with infinite aspect ratio to craft of similar construct with finite aspect ratio. The method is completed by an empirically determined function which can be used to perform this conversion.

Using this method as a basis, UACC adopted a method of mapping flutter velocities between two crafts of similar construction, each with finite aspect ratio (as opposed to mapping



between two crafts of similar construct, one with finite aspect ratio, the other with infinite aspect ratio - as detailed by *Molyneux et al.*).

Molyneux et al. present an argument that the effect of aspect ratio on flutter velocity can be modeled by first considering a similar wing of infinite aspect ratio. It can be shown, by modifying the relevant quantities in the coupled oscillator equation, that the calculated flutter velocity for a finite aspect ratio craft is related to the calculated flutter velocity for an infinite aspect ratio craft of similar make by the following equation:

$$V_{\text{flutter}} = V_0 f(\text{AR}) \quad , \quad (2)$$

where V_0 is the flutter velocity for an infinite aspect ratio, V_{flutter} is the flutter velocity for a finite aspect ratio (the quantity of interest) and $f(\text{AR})$ is a function only of aspect ratio. The argument detailed in *Molyneux et al.* only shows that this equation is valid to merely consider the effect of aspect ratio by multiplicative scaling by some undetermined function (of aspect ratio only). However, it does not provide the exact form of the function - it only argues that a form with this dependence is sufficient to account for the relationship between aspect ratio and flutter velocity*.

Determination of $f(\text{AR})$ is necessary to complete *Molyneux et al.*'s procedure. Though possible analytically, it is simpler and more reliable to find $f(\text{AR})$ empirically. Following this idea, UACC analyzed several sets of similar wing planforms with comparable aerodynamic and structural derivatives for each wing in a given set but varying in aspect ratio.

Using an analytically determined value for V_0 (based on an infinite aspect ratio wing with the same structural and aerodynamic derivatives), $f(\text{AR})$ was determined empirically yielding the following overall form:

$$V_{\text{flutter}} = V_0 \left(1 + \frac{0.8}{\text{AR}} \right) , \quad (3)$$

This equation is sufficient to account for variation of flutter speed due to aspect ratio.

Now, for a new set of wings, *Molyneux et al.* suggests that V_0 be calculated from a set of 2D

* This is the extent of the result of the analytic portion of the method. For more detail on the derivation of this form, consult *Molyneux et al.*

aerodynamic strip derivatives for our wings. However, V_o can be computed using simpler methods: a craft with known V_{flutter} and AR can be used to calculate V_o for the particular family of wings sharing its aerodynamic and structural derivatives. From here, the formula can be reapplied to yield a new equation giving the flutter velocity for a new aircraft in terms of the known flutter velocity of another aircraft. Under this modification of the original method, the following equation giving the flutter velocity for Azalzan is obtained:

$$V_{\text{flutter}} = V_s \left(1 + \frac{0.8}{AR_t} + \frac{0.8}{AR_s} \right) , \quad (4)$$

where V_s is the measured or calculated flutter velocity of a structurally and aerodynamically similar reference aircraft, AR_t is the aspect ratio of Azalzan, AR_s is the reference aspect ratio, and V_{flutter} is the calculated flutter velocity for the craft. Using listed values of V_{NE} and V_D for various aircraft which are relatively similar to Azalzan, as well as regulations concerning the relationship between these velocities and flutter velocity, lower bounds for the flutter velocities of these various aircraft were derived. Using Eq.4 and the calculated flutter velocities (as well as the corresponding aspect ratios) of the reference aircraft, it is possible to create a list of possible V_{flutter} 's.

The sample aircraft were assumed to cover an extensive range of structural and aerodynamic characteristics similar enough to Azalzan so that it falls somewhere within the parameter space mapped out by the sample aircraft. Therefore, the lowest estimate of V_{flutter} given by these aircraft is a worst case scenario for Azalzan, since the previously estimated values for the various V_s are already pessimistic. Thus, it was found that it is highly unlikely for Azalzan to have a flutter velocity below this worst case estimate. Therefore, if the estimated flutter velocity exceeds the velocity necessary for regular operation, Azalzan satisfies the flutter requirements with high probability. Due to the extremely conservative and empirical nature of this estimate, UACC believes that its results are as dependable as those obtained by performing a computationally intensive analysis, but requiring significantly less effort. Using the procedure, a worst case value of 147 *kts*. for V_{flutter} was calculated, which is above the operational speed requirements, as discussed in Ch. 13.

7.6 Empennage Structure

The vertical tail of Azalzan features a similar structure as the wing in terms of architecture and composite material application. The horizontal tail is supported through a linkage to two fuselage frames. The elevator incidence angle is varied by a double redundant mechanical system installed inside the horizontal tail of the aircraft. Figure 50 presents the general structural arrangement of the empennage of Azalzan.

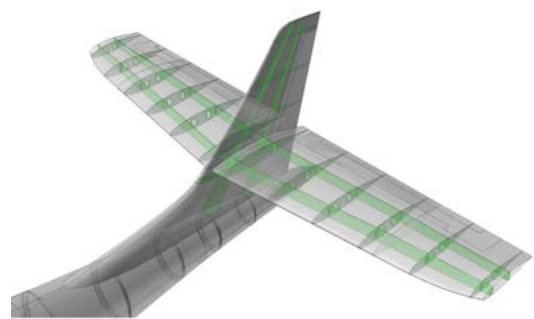


Fig. 50 Empennage Structure

7.7 Manufacturing Methods

Due to the utilization of carbon laminated composites, Azalzan is able to be manufactured using modern automated composite laying methods. These methods allow for manufacturing of large, continuous pieces of structure rather than the conventional method that relies on manufactured sub structures to create larger assemblies. The fuselage structure of Azalzan is to be manufactured in computer controlled, rotary matrix laying barrels that will be cured with heat and pressure to ensure obtaining the required mechanical properties. Wing skins are to be laid in large, continuous pieces, eliminating the possibility of small surface misalignments, then are polished to obtain an average geometric roughness of $0.05 \mu\text{m}$. If the wing surfaces of Azalzan are manufactured using conventional methods, these common misalignments (present at manufacturing or created during the service life) can lead to the tripping of the boundary layer, therefore making the implemented NLF technology less effective. Compatibility of the structural design of Azalzan with modern manufacturing methods allows for higher production rates and buy-to-fly ratios. Higher rates of production allows for substantial reduction in the overhead cost per plane and higher buy-to-fly ratios allow for significant reductions in the cost of raw materials used to build the aircraft. The exploded weight group foldout in Ch 10 presents the material distribution and the structural breakdown for Azalzan.

8.0 Propulsion

8.1 Electromotor Type Selection

In order to maintain a low overall weight figure and a high efficiency, various types of electric motors were studied to be used as a powerplant for Azalzan. Given that available battery technologies only produce direct current (DC), a tradeoff was observed between using a lower weight AC motor in need of a separate power inverter unit (DC/AC converter) and using a heavier DC motor with no need of a converter. Performing a survey of existing types of electro-motors from various manufacturers, UACC concluded that a DC brushless motor is the best available electro-motor type for the configuration. DC brushless motors typically have higher efficiencies than other comparable DC motors and have a simpler mechanical construction with no need of complex control circuits to regulate RPM³⁹. Table 6 presents a summary of the most promising choices of electric motors studied.

Table 6 Summary of Motor Selection Study

Yuneec Power Drive 60		UQM Powerphase 75	AC Propulsion Drive	BRUSA ASM8.24.10
Type	Brushless DC	Brushless DC	AC Induction	AC Induction
Weight (lb.)	66	90	110	150
Accessory Weight (lb.)	20	35	66	21
Operational Weight (lb.)	86	125	176	172
Max Power (hp)	81	100	268	82
Power Density (hp/lb)	1.23	1.11	2.44	0.55
Max Torque (lb-ft)	410*	176	N/A	400
Max Efficiency	92	94	90**	93

*Calculated; ** Approximate

8.2 Propeller

The propeller design for Azalzan was based on the limits defined by the performance of the motor selected and the goal of reducing noise to increase passenger comfort. The performance of the motor defines the range of RPMs in which the propeller is to operate, by knowing the RPM value at which the motor produces the maximum power. Minimizing the noise produced by the

propellers was also one of the design goals. As suggested by Hartzell Propeller Inc., UACC designed a propeller with a high number of blades to reduce propeller noise⁴⁰. The effects of the number of blades on efficiency, weight, and thrust produced were evaluated, and it was determined that an 8-blade propeller would be implemented given its higher relative performance and the small effect the increased number of blades has on the propeller weight (around 16 *lb.* increase relative to 3-blade propeller, which is counteracted by the smaller battery required). Figure 51 shows the 8-bladed propeller designed.

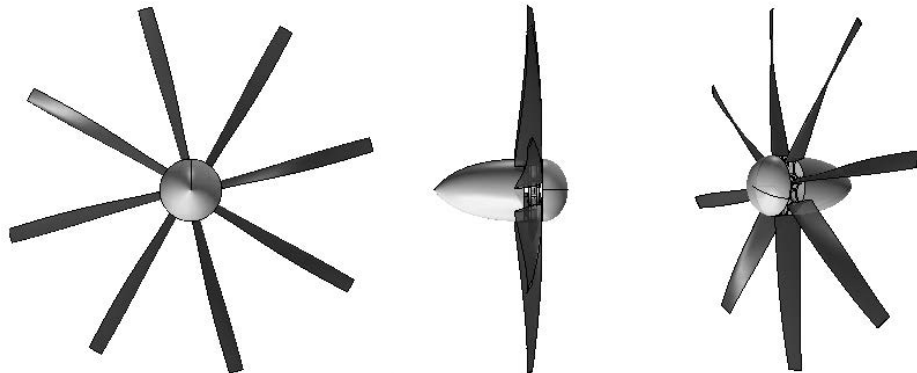


Fig. 51 Pusher propeller CAD Model

JavaProp, a java-based propeller design applet created by *Dr. Martin Hepperle*, was used to design and evaluate several propellers taking into account the aforementioned constraints (motor performance and number of blades). The performance of the propellers was evaluated at all critical flight conditions, with the efficiency at cruise being the design-driving factor given its significant effect on total energy required. For each flight condition, the velocity and the required thrust were known from the detailed aerodynamic analysis, and after setting the number of blades, the diameter and rotational speed were the parameters yet to be determined. The diameter was set at a value of 4'6" to allow for enough ground clearance during normal operation and tilted operation (as will be further described) of the propeller.

From the results obtained using *JavaProp* it was observed that the propeller efficiency would be maximized for a rotational speed in the range of 1400-1800 RPM. A cruise value of 1,600 RPM was selected after evaluating propeller efficiencies corresponding to several RPMs. Four different airfoils designed by *Hepperle*, included in *JavaProp*, were used along the radial direction of the

propeller, for which the applet optimizes the propeller twist distribution. The result is a propeller with a cruise efficiency of 91%. The efficiency and thrust curves of the propeller at cruise are shown in Fig. 52. Additionally, the propeller presents high efficiencies in other flight conditions, with all the efficiency values being above 75%.

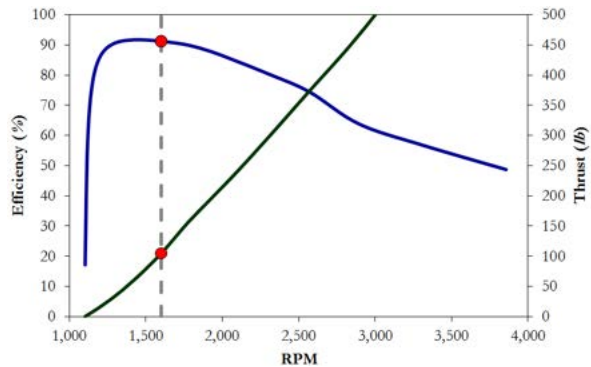


Fig. 52 Results of propeller efficiency analysis @ cruise

A tilting mechanism was designed to allow for the propeller to be tilted a maximum of 40° downwards. An electric linear actuator located in the fuselage rotates a hollow shaft axially aligned with the driveshaft. The hollow shaft in turn transmits its rotational motion to the propeller shaft via a rubber belt, which transmits the required torque to turn a U-joint in the propeller driveshaft.

Tilting the propeller downwards affects the dynamics of the aircraft in two ways: First, the resulting inclined thrust has a component directed upwards, which adds to the lift of the airplane. Second, the combined effects of propeller tilting and flap deflection greatly increase the maximum lift of the aircraft, as will be further described in section 12 .Figures 53 and 54 depict the propeller tilting mechanism.

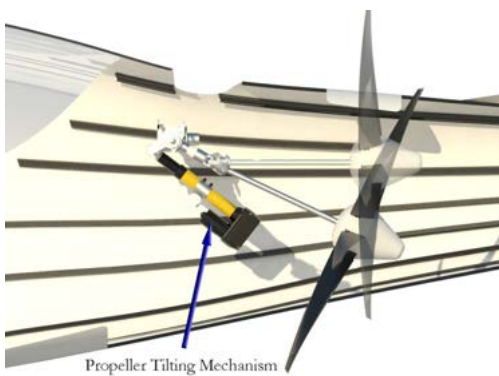


Fig. 53 Propeller tilting mechanism close up



Fig. 54 Propeller tilting mechanism detail

9.0 Electrical Systems

9.1 Electrical Storage

As it was previously stated in Sec. 2.2, lithium-air batteries possess sufficient energy while having the lowest weight and development risk of all comparable battery types. A survey of developers of modern battery technologies indicated that at present there are two main entities that are working towards commercialization of lithium-air battery technology, namely *PolyPlus* of Berkeley, CA and the University of Dayton Research Institute in Dayton, OH. Contact was made with the published researchers⁴¹ in these organizations and, as a result of their cooperation, information was obtained regarding the performance and viability of using a lithium-air battery as the primary energy source for aerospace applications in the near future.

It was determined that, given their solid-state nature, there are no special safety concerns regarding lithium-air batteries, such as explosions or catastrophic failures. From the correspondence, it was also determined that lithium-air batteries possess an efficiency of 70% at high drain rates and an estimated energy density of 1,000 *Whr/kg*. The lithium-air electro-chemical process is determined to be highly exothermic, which requires a dedicated high-performance cooling system integrated with the battery pack. It was also established that, by 2016, such batteries will be made available commercially. An estimated minimum five-year shelf life and over 500 charge cycles are projected for a commercialized lithium-air battery unit. It was also confirmed that the lithium-air battery unit has to be operated at relatively high temperatures, generally greater than 120 °F. Given this information and the most accurate estimation of the required amount of energy to fly the mission specified by the RFP (presented in Sec. 2.3), a lithium-air battery pack was designed taking into account its integration with the dorsal fuselage section. Figure 55 presents a view of the battery pack design. Considering that the battery pack is made up of hundreds of small cells⁴², the outer geometry of the pack can be tailored to fit in otherwise unused spaces in the aircraft. The battery pack was designed to utilize some of the

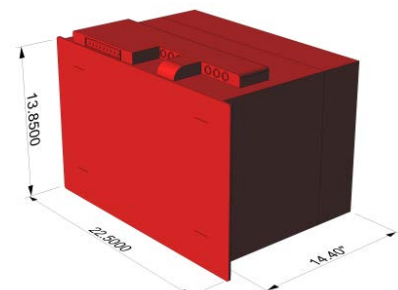


Fig. 55 Battery pack

unused space in the lower fuselage section. An onboard battery charger/monitor rectifies alternating current from a conventional electrical outlet to direct current required to charge the battery. The performance of the charger will be discussed further in Sec. 14.2.

9.2 Electric Distribution Architecture

The presence of a high-voltage motor as well as low-voltage components dictates that the electric architecture of Azalzan must feature two voltages of 166 V and 28 V , respectively. This requires the implementation of a DC-DC converter to extract the 28 V electric current from the high-voltage ($161\text{-}190\text{ V}$) battery. The high current demand of the motor (342 A max.) requires two wires to carry each of the three phases to minimize voltage loss and eliminate the need for a complex, heavy, and expensive circuit breaker. The architecture was fully simulated in the *Simulink* environment to verify the behavior of the system via validating steady-state currents, motor speed, and mechanical torque produced by the motor in various flight conditions. A sample signal reading is presented after the electrical system foldout.

The requirement of specific voltages and currents for the motor to operate as desired at every flight condition makes it necessary to implement an advanced power management system. This system acts as a controller, determining the optimal current and voltage levels that must be supplied by the battery to the motor. The unit creates the desired three-phase output for the motor from a DC current provided by the battery. Another smaller control system is used to regulate the low-voltage (28 V) electric circuit, comprised of the prop-tilting actuator, cockpit lighting, and instrumentation.

9.3 Avionics and Secondary Electrical Components

A number of secondary electrical components are present in Azalzan, including the avionics system, the lighting system, and the prop-tilting actuator. The avionics package consists of a combination of multi-function displays (MFDs) and backup analog instruments. The main element is the *Garmin GTN™ 750*, a $7''$ digital MFD that has all of the relevant flight indicators, e.g. artificial horizon, altitude, rate of climb, airspeed, horizontal situation indicator, and G-meter. Additional

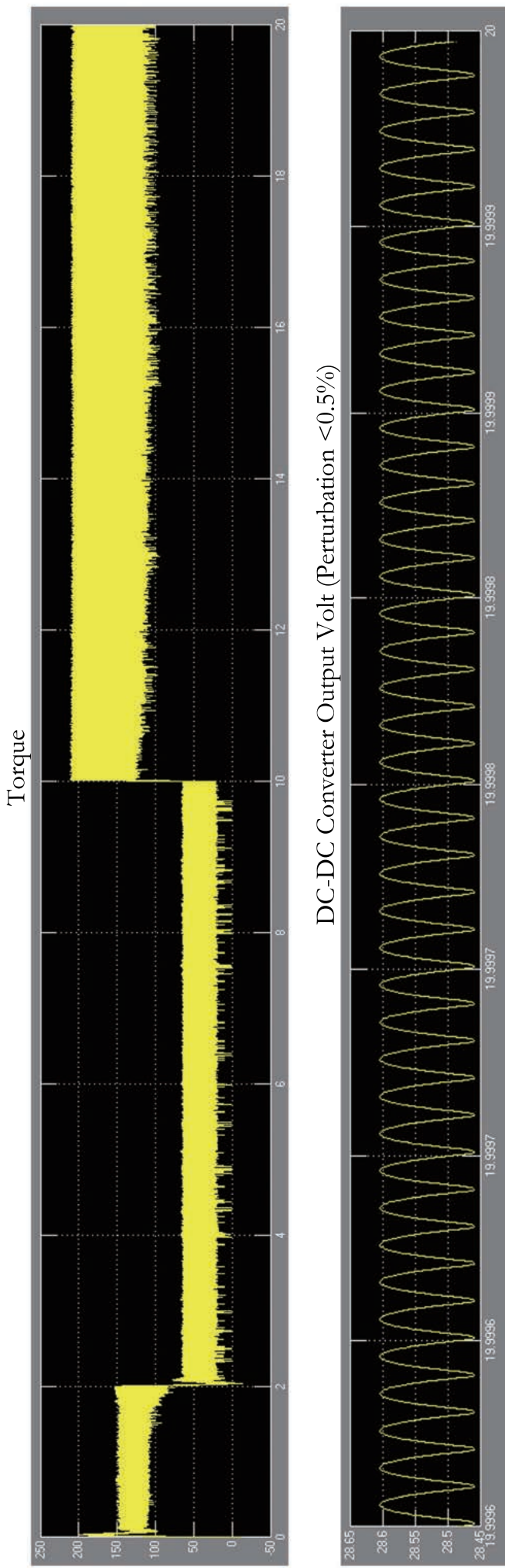
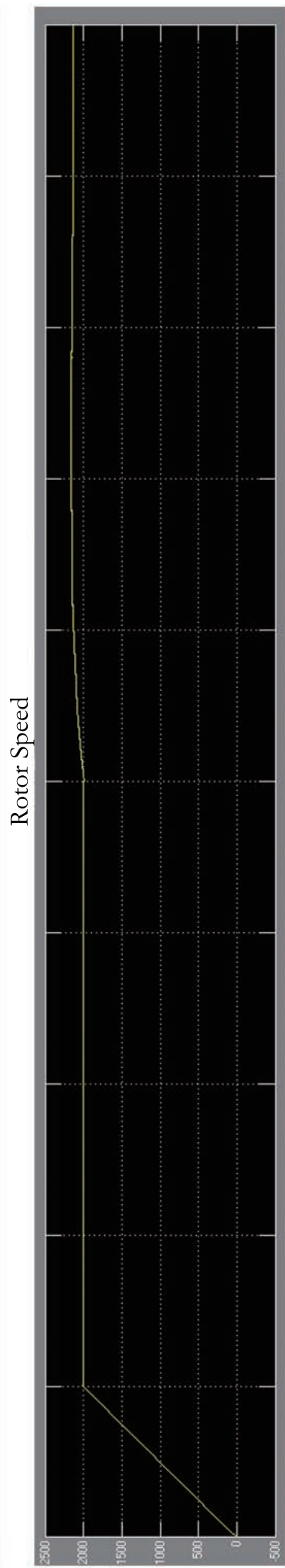
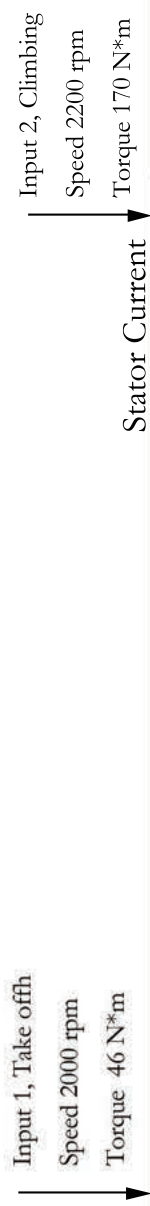
units display the motor parameters, e.g. power and RPM, and navigational maps. On the co-pilot side of the cockpit, flight-test instruments are installed to obtain measurements and relevant information in the prototype aircraft. Figure 56 shows the cockpit layout of a flight test airplane model.



Fig. 56 Cockpit layout in a prototype airplane

The commercial version of Azalzan will be available with a variety of options for instrumentation ranging from an iPad-based system developed by *Amapola Flyg*⁴³ to an all-in-one GPS/Nav/Comm *Garmin* system. The iPad-based instrumentation will require an external GPS signal antenna to increase the accuracy of the GPS processors installed. The antenna would be located on the tip of the vertical tail. All the configurations include a battery energy level indicator.

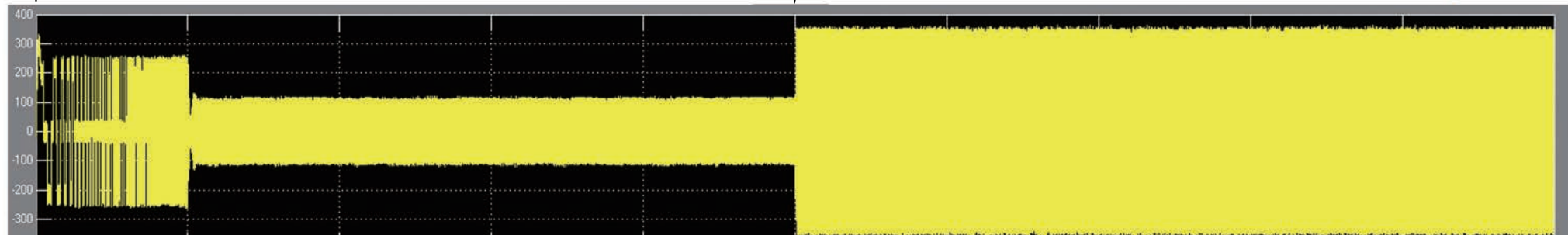
The propeller-tilting mechanism is activated autonomously when a deep stall is detected by the air data computer of the aircraft. The *Nook CC* 12"-travel 24 VDC electrical linear actuator was selected given its low weight and high static capacity (3,000 lb.). The electric system foldout shows the main components of the electric system, including the avionics layout and the electric architecture.



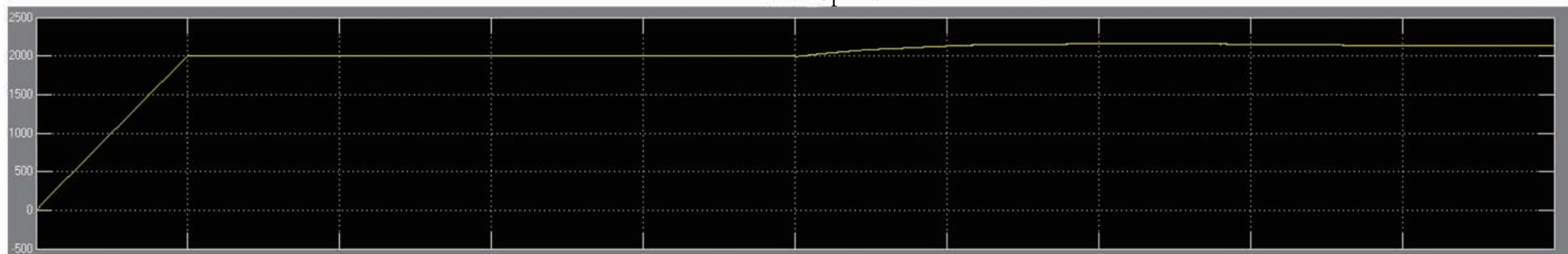
Input 1, Take offh
Speed 2000 rpm
Torque 46 N*m

Input 2, Climbing
Speed 2200 rpm
Torque 170 N*m

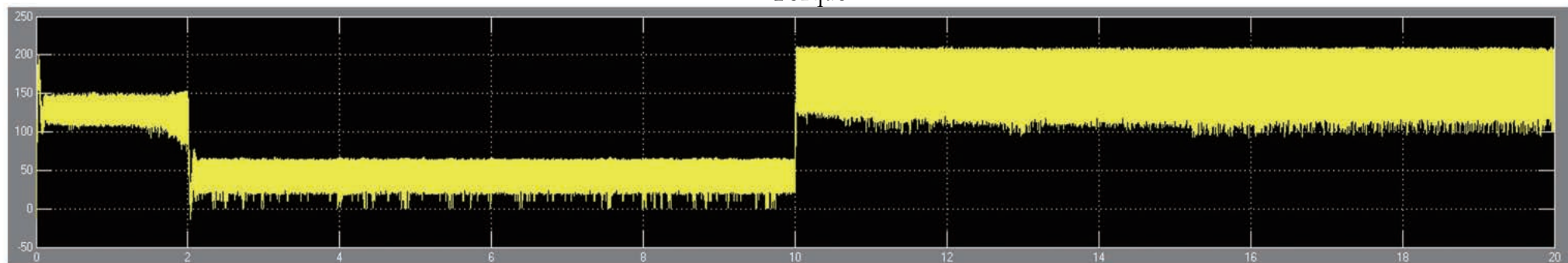
Stator Current



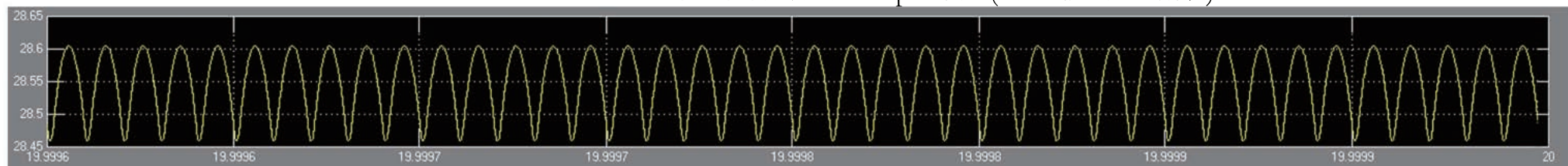
Rotor Speed



Torque



DC-DC Converter Output Volt (Perturbation <0.5%)



10.0 Systems Integration

10.1 Heat Management

The use of high-powered electric and electronic systems results in a large quantity of heat that must be dissipated to maintain optimum operating conditions. An advanced heat management system was designed combining liquid-cooled and air-cooled systems to dispose large amounts of excess heat. As suggested by Tesla Motors⁴⁴, a liquid-air plate-fin heat exchanger was used for cooling the battery pack due to its low weight and high volume-to-surface area ratio⁴⁵. The heat exchanger for the system was sized using methods outlined by Hesselgreaves⁴⁶ to determine its overall volume and weight as well as the required mass flow of the cooling liquid and air. The heat generated by the battery, summarized in Table 7, was

Table 7 Power used and heat generated at critical flight conditions.

calculated in order to size the heat exchanger. The heat was calculated by assuming that the battery power inefficiency was dissipated in the form of heat.

Flight Condition	Power (kW)	Heat (kW)
Takeoff	37.7	17.0
Climb	12.2	5.2
Cruise	12.3	5.3
Descend	92.7	4.0
Landing	10.0	4.3

The heat exchanger was designed to dissipate a maximum of 17 kW of heat as dictated by the battery heat generation during takeoff. It was determined that a maximum water flow rate required to remove the heat generated to be 3.0 gal./min. The maximum airflow at standard conditions is 195 *cfm*. To circulate the cooling fluid, the *Flojet* Quad Pump 4000 Series, an electrically-driven water pump capable of inducing 5.0 gal./min., was selected because it satisfied the required flow rate while having the lowest weight. Figure 57 shows the location of the battery cooling system in the fuselage.

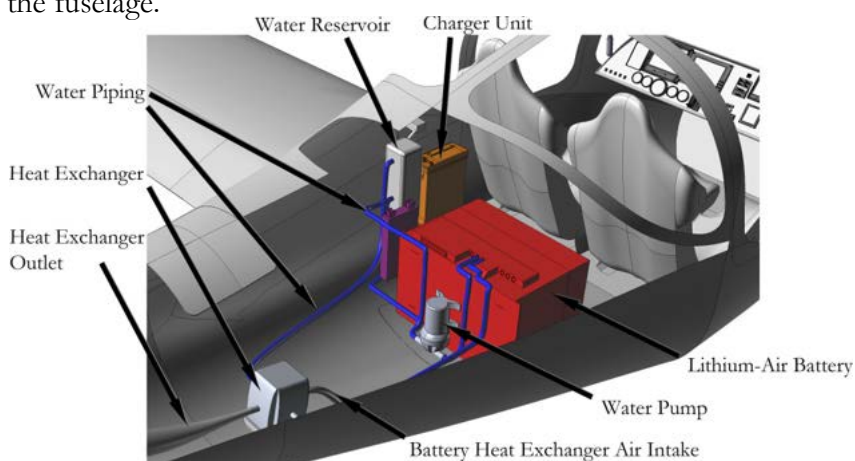


Fig. 57 Battery cooling system

The cooling air needed for the operation of the heat exchanger is obtained via a scoop installed on the lower fuselage with a frontal area of 8.9 in.^2 . The scoop is offset by 1.5 in. from the lower fuselage surface into the airstream, to avoid ingesting the low-energy fuselage boundary layer. To ensure that no interference arises from the ingestion of the tire spray during wet runway ground operations, a tire spray pattern analysis was performed using methods outlined in ESDU Data Item 83042⁴⁷ to determine the maximum depth of water allowable. The maximum depth of contaminates on the surface of the runway, at which the operations of the cooling system of the aircraft may be impacted by the impinging tire spray released from the nose landing gear, was determined to be $3/8''$, corresponding to a side spray elevation angle and a plan view angle of 18° each. Figure 58 presents the tire spray pattern at the maximum contaminate depth.

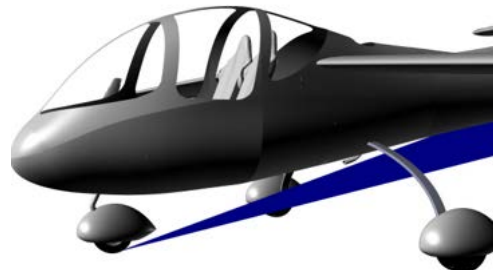


Fig. 58 Tire spray

The motor is cooled by air that is obtained via a large S-duct routed from the upper fuselage. The heated air flows from the motor through the tail cone, exiting the aircraft at the base of the fuselage assisted by the operation of the propeller.

10.2 CFD Verifications

Given the complexity of the arrangement of the heat-producing systems inside the fuselage, a numerical simulation was required in order to obtain accurate predictions of temperature at various locations of the fuselage. To achieve this, the geometry of the aft fuselage, including all of the systems, mid wingbox, and the cargo area was used to create an unstructured volume mesh in *ANSYS ICEM* environment. Figure 59 presents a view of the analysis domain.

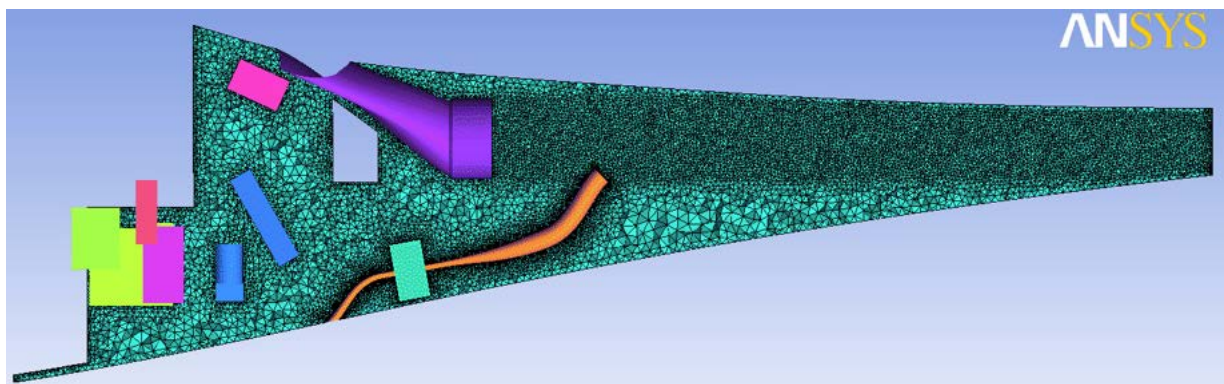


Fig. 59 CFD mesh for thermal analysis. The final model included more than five million nodes refined at more critical areas, such as areas with strong airflows present (i.e. adjacent to cooling air jets).

Basic thermal loads were applied to the model by either determining the heat generation through boundary conditions or, in rare cases, steady-state temperature and thermal conductivity. Mass flows were applied through the air inlets and an operating pressure was defined for the fuselage tail cone outlet. Table 8 presents a summary of the assumptions applied to the thermal model.

The analysis was repeated for two thermal cases; one during cruise at ISA conditions at 10,000' and the other at 500' at ISA+23.5°C (100 °F) while all systems are performing at their maximum allowable temperature. Results were post-processed to ensure that at no place in the fuselage the temperature exceeds the maximum allowable operating temperature of any of the components and the airframe. A summary of the results of the numerical thermal simulation is presented on the mechanical systems foldout.

Table 8 CFD assumptions applied to the thermal model to numerically analyze the heat generated by exothermic systems inside the fuselage

Hot Day Approach: ISA +23.5 °C @ 500 ft			
Component	Boundary Condition	Value	Units
Battery	Static Temperature	75.0	°C
Cargo Area	Adiabatic	----	----
Charger	Adiabatic	----	----
DC/DC Converter	Heat Flux	492.7	W/m ²
		150.0	W
Fuselage	Heat Transfer Coefficient	5.9	W/(m ² ·K)
		37.9	°C
Heat Exchanger	Static Temperature	47.1	°C
Heat Exchanger Exhaust	Heat Transfer Coefficient	13.0	W/(m ² ·K)
		56.4	°C
Heat Exchanger Inlet	Mass Flow	0.2	kg/s
		56.4	°C
Heat Exchanger Intake	Heat Transfer Coefficient	5.9	W/(m ² ·K)
		37.9	°C
Landing Gear Beam	Adiabatic	----	----
Motor	Heat Transfer Coefficient	15.5	W/(m ² ·K)
		38.9	°C
Motor Inlet	Mass Flow	1.1	kg/s
		38.9	°C
Outlet	Relative Static Pressure	-32.4	Pa
Parachute Pack	Adiabatic	----	----
Power Controller	Heat Flux	109.4	W/m ²
		246.0	W
Coolant Pump	Heat Flux	570.4	W/m ²
		51.8	W
Coolant Reservoir	Adiabatic	----	----
Spars	Adiabatic	----	----

Cruise @ 10,000 ft			
Component	Boundary Condition	Value	Units
Battery	Static Temperature	50.0	°C
Cargo Area	Adiabatic	----	----
Charger	Adiabatic	----	----
DC/DC Converter	Heat Flux	492.7	W/m ²
		150.0	W
Fuselage	Heat Transfer Coefficient	7.5	W/(m ² ·K)
		-2.3	°C
Heat Exchanger	Static Temperature	4.2	°C
Heat Exchanger Exhaust	Heat Transfer Coefficient	13.2	W/(m ² ·K)
		10.6	°C
Heat Exchanger Inlet	Mass Flow	0.3	kg/s
		10.6	°C
Heat Exchanger Intake	Heat Transfer Coefficient	7.5	W/(m ² ·K)
		-2.3	°C
Landing Gear Beam	Adiabatic	----	----
Motor	Heat Transfer Coefficient	16.2	W/(m ² ·K)
		-1.5	°C
Motor Inlet	Mass Flow	1.6	kg/s
		-1.5	°C
Outlet	Relative Static Pressure	-83.2	Pa
Parachute Pack	Adiabatic	----	----
Power Controller	Heat Flux	109.4	W/m ²
		246.0	W
Coolant Pump	Heat Flux	570.4	W/m ²
		51.8	W
Coolant Reservoir	Adiabatic	----	----
Spars	Adiabatic	----	----

10.3 Flight Control System

A mechanical reversible control system was implemented in Azalzan given its simplicity and light weight compared to irreversible systems, e.g. fly-by-wire systems. The small hinge moments required to actuate the control surfaces, presented in Ch.12, make it possible to use a direct system in which no heavy hydraulic assistance is necessary. This reflects the trend experienced in LSAs of using reversible mechanical control systems. The pilot controls the aircraft in a conventional manner using a stick to control pitch and roll via elevators and ailerons, respectively. Pedals are used to provide yaw control through a fin rudder. A pulley mechanism transfers the control stick and pedal motions to the control surfaces as shown in Fig. 60. The mid-motor pusher configuration dictates the use of a driveshaft that can interfere with the routing of control cables to the empennage surfaces. As a result, a novel ring-shaped mechanism was used to generate the desired movement of the control surfaces while avoiding the driveshaft, as depicted in Fig. 61.

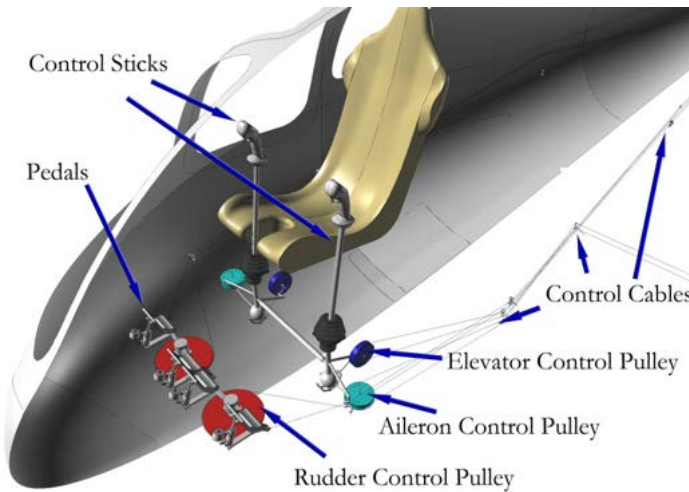


Fig. 60 Flight control system

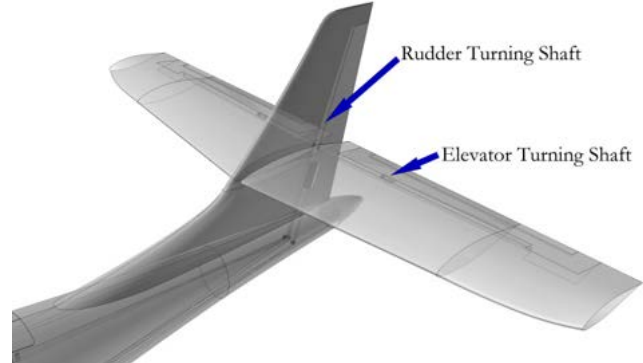


Fig. 61 Control cables and driveshaft

10.4 Steering and Brakes

As mentioned in Sec 5.9, pedals are used in Azalzan to control steering and braking while on the ground. The steering system consists of a gear mechanism that transfers pedal rotational motion into the nose landing gear, allowing the aircraft to turn easily on the ground. The mechanism is

designed so that the torque required from the pilot is smaller than the torque produced on the nose wheel, alleviating the required pedal force exerted by the pilot.

Azalzan uses a closed circuit hydraulic differential braking system. This increases maneuverability on the ground by allowing the pilot to brake each wheel separately, providing a pivot point around which to rotate. This results in a minimum turn radius of 5.3', measured from the pivot point to the centerline of the airplane. The brakes are controlled by a hydraulic system that is activated by pressing on either the pilot or copilot pedals. A maximum hydraulic pressure of 500 psi was calculated to provide enough braking force to stop in 380'. A disc braking system with 4"-diameter rotors is installed in each main wheel assembly, providing braking power for the wheels. Figure 62 presents a view of the turn radius of Azalzan. Figure 63 details the steering system and braking cylinders.

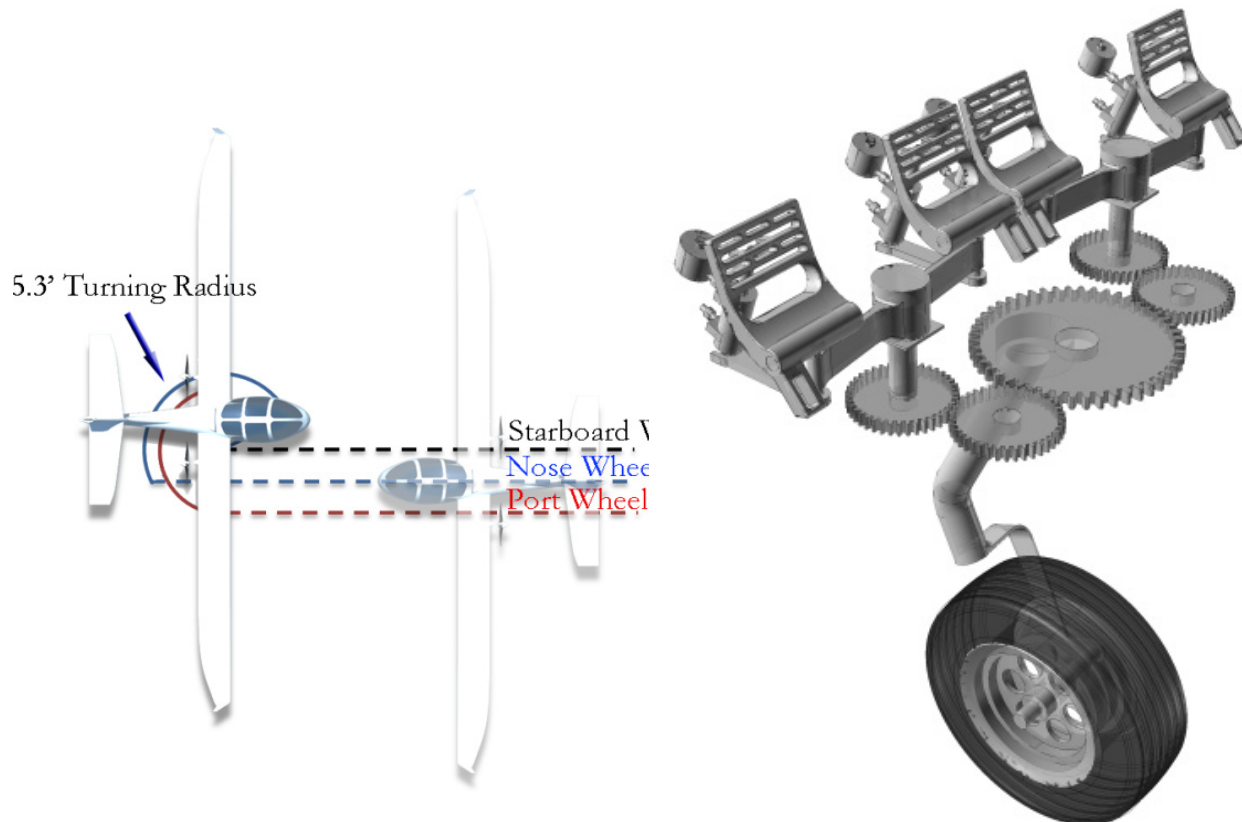
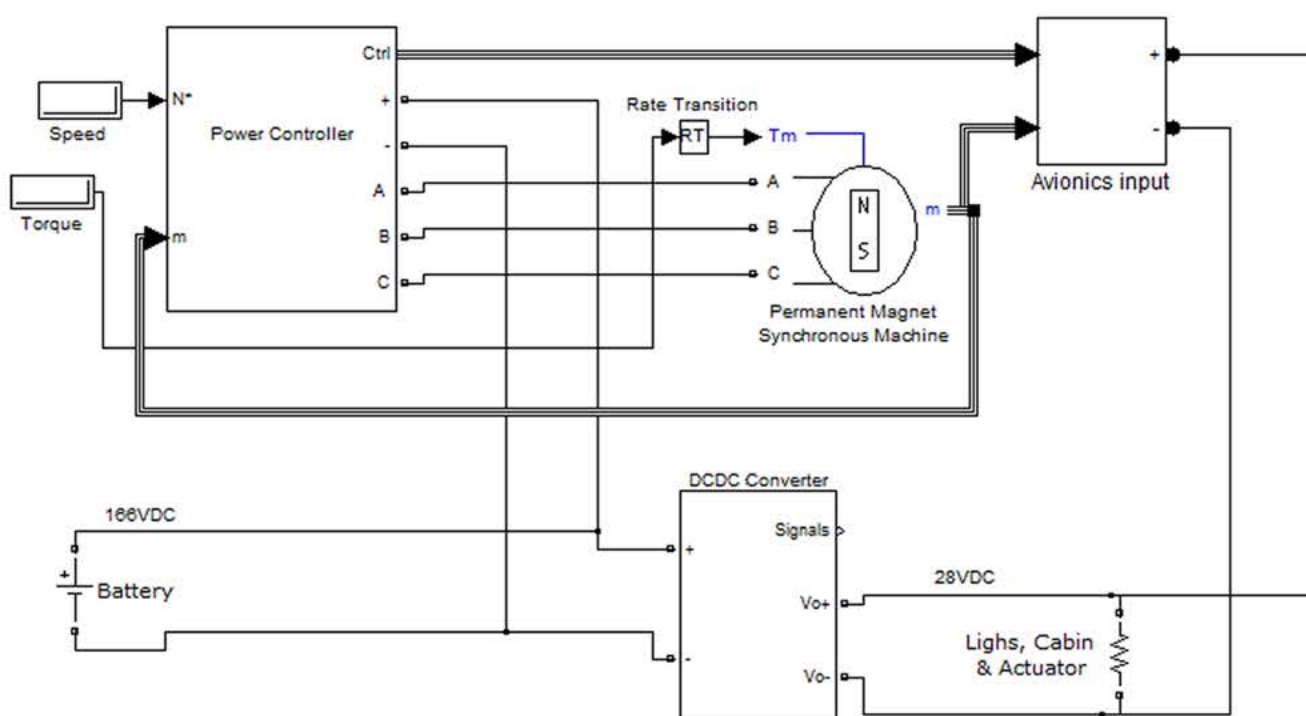
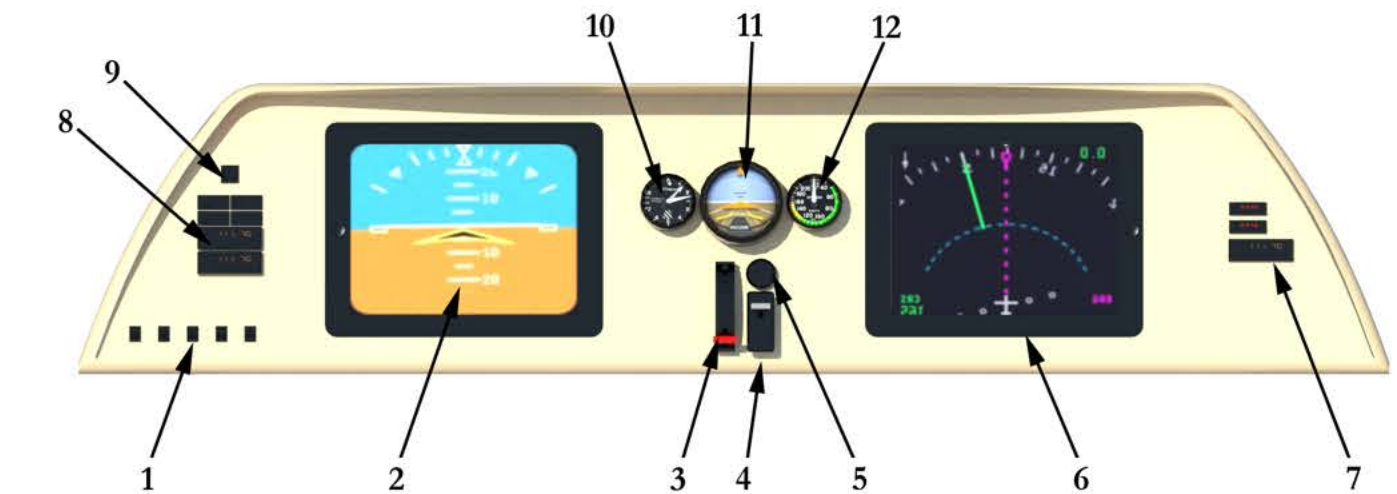
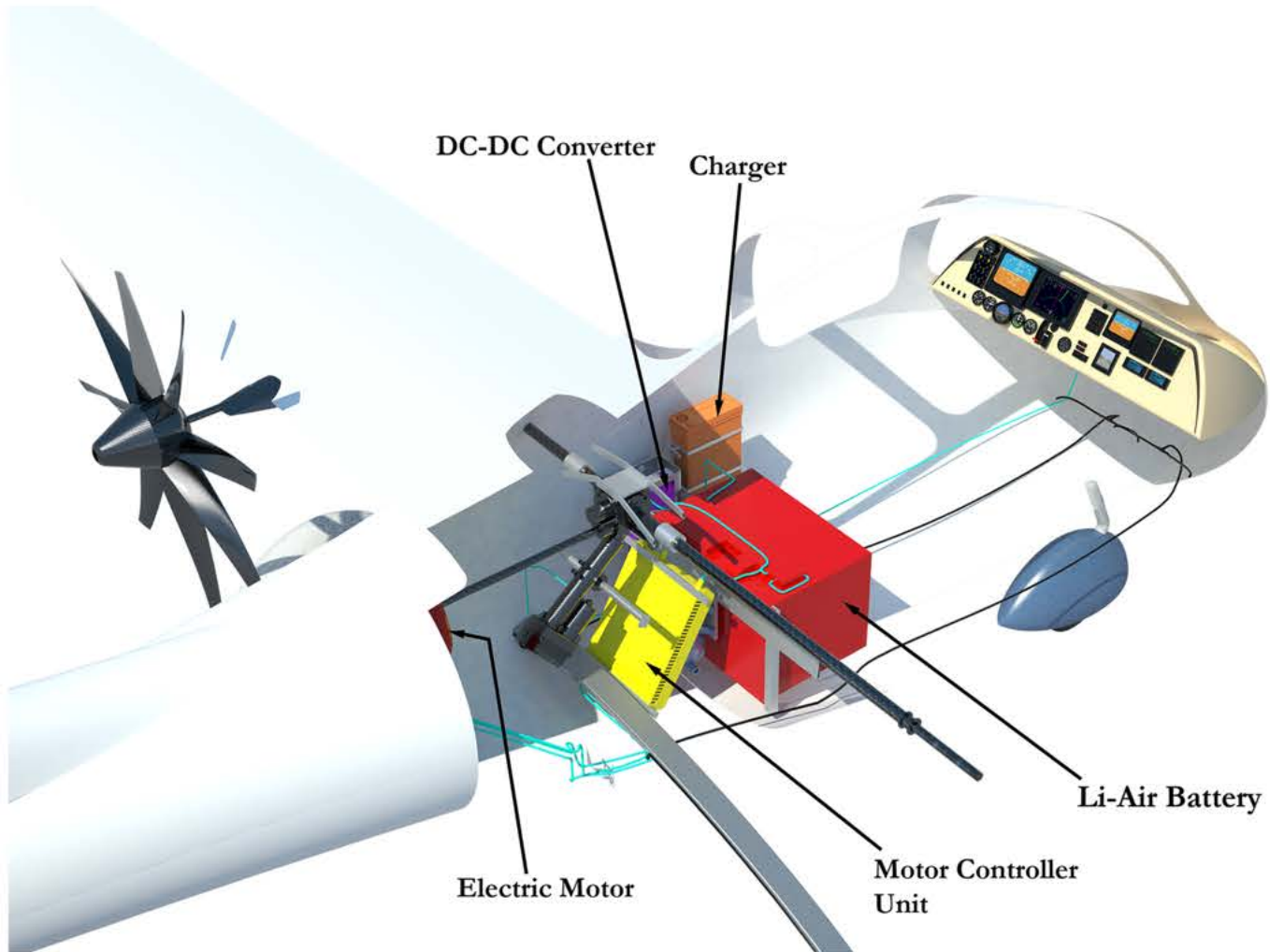


Fig. 62 Top View of turning radius

Fig. 63 Steering system



- Electric switches
- iPad unit with instrumentation software
- Flap position heaver
- Throttle
- Battery charge indicator
- Secondary passenger iPad unit (optional)
- Secondary radio panel (optional)
- Primary radio panel
- Radio unit power switch
- Analog altimeter (optional back-up)
- Analog attitude indicator (optional back-up)
- Analog air speed indicator (optional back-up)
- Analog rate of climb indicator (optional back-up)
- Propeller RPM indicator
- Prototype test radio compass
- Video camera display
- Prototype test telemetry display
- Bank/turn indicator
- Flight engineer attitude indicator
- Data recorder multi-function panel

12.0 Stability and Control

12.1 Loading Cases

As suggested by the RFP, the alternative loadings of the airplane were investigated by determining the CG location for three critical cases; a single light passenger (120 *lb.*) with no luggage, two light-heavy passengers (170 *lb.*) with luggage (60 *lb.*), and two heavy passengers (200 *lb.*) without luggage. Additionally, the option for trading one passenger for an additional battery was accommodated for. It was concluded after the analysis (as will be presented in following sections) that Azalzan is capable of accommodating all loading cases required by the RFP with sufficient longitudinal static margin and negligible degrading of handling performance.

12.2 Balance, CG Travel, and Wing Location

Static stability of the configuration was achieved by performing a parametric study of the impact of the longitudinal location of the wing on the magnitude of static margin using the methods presented by Roskam⁵². Mass properties analysis of Azalzan indicated that a CG travel range equivalent to 19.8% of mean aerodynamic chord of the aircraft is possible among all different loading cases dictated by the RFP. A minimum target positive stick free static margin of 20%⁵³ was selected for the mid-cruise segment of the flight to ensure the inherent static stability of the aircraft.

The result of this parametric study can be seen in Figure 66.

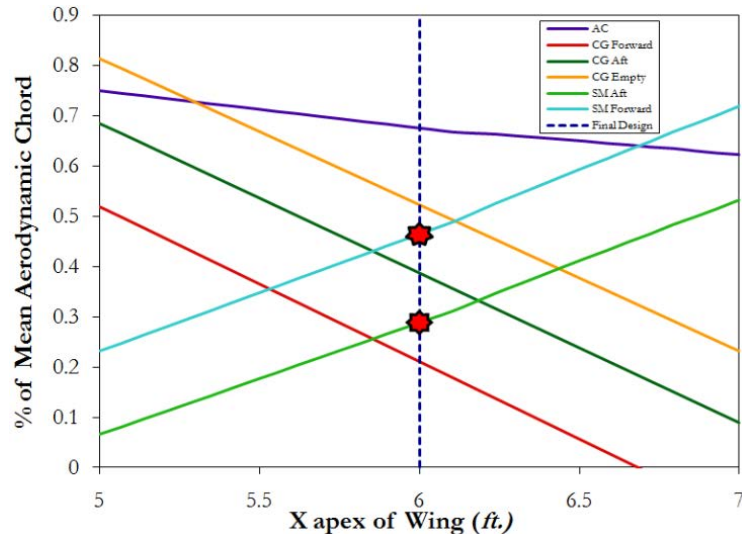


Fig. 66 Wing location trade study

11.0 Weight Justification & Analysis

11.1 Detailed Weight Analysis

A detailed weight analysis (Class II⁴⁸) collaborates the methods established by *Cessna*⁴⁹, the United States Air Force, *General Dynamics*, and *Torenbeek*⁵⁰ to accurately project the weight of the aircraft by verified methods based on geometry of the airplane⁵¹. However, the versatility and utility of these methods are not without faults. Specifically, these methods are overly general and are best applied to standard aircraft configurations and fall short when applied to aircraft with unconventional characteristics like Azalzan, e.g. high aspect ratios, wing folding mechanisms, and heavy use of composite materials. For example, the *Cessna* weight methods predicted an overly large value for the wing weight that contradicted common sense. Due to this deficiency, UACC later pursued a Class III part-by-part weight estimation that broke down the design of Azalzan into an appropriate custom weight estimation. Table 10 presents the results of the Class II weight estimation.

Table 10 Summary of Class II weight estimation

Weight Component	Cessna Method (lb.)	USAF Method (lb.)	GD Method (lb.)	Torenbeek Method (lb.)	Average Values (lb.)
Wing	130	123	-----	125	126
Horizontal Tail	28	28	-----	-----	26
Vertical Tail	10	8	-----	-----	8
Fuselage	122	87	-----	-----	104
Nose Landing Gear	8	1	-----	28	14
Main Landing Gear	35	2	-----	73	43
<i>Structure</i>	<i>332</i>	<i>249</i>	-----	<i>226</i>	<i>323</i>
Propeller	-----	-----	66	66	61
Propeller Motor	136	-----	-----	130	66
Tilting System	-----	-----	-----	-----	14
Battery	-----	-----	-----	-----	160
Propeller Shaft	-----	-----	25	23	63
<i>Power Plant</i>	<i>136</i>	-----	<i>91</i>	<i>219</i>	<i>364</i>
Air Induction System	-----	-----	-----	1	1
Flight Control System	27	108	-----	32	47
Avionics	-----	-----	-----	66	43
Electrical System	43	85	-----	39	47
Cooling	-----	33	-----	5	15
Furnishings	34	-----	-----	31	20
Other Items	-----	-----	-----	5	3
Parachute	-----	-----	-----	-----	33
<i>Fixed Equipment</i>	<i>103</i>	<i>226</i>	-----	<i>178</i>	<i>208</i>
Empty Weight	-----	-----	-----	-----	895
Maximum Takeoff Weight	-----	-----	-----	-----	1,295

11.2 Class III Weight Estimation

The UACC component-by-component weight analysis was done following the Class II weight analysis to ensure the integrity of the estimated weight of Azalzan. UACC verified the structural integrity of major load-bearing structure using the methods discussed in Ch. 7 as well as FEA performed using *SolidWorks*. The verified geometry's weight was analyzed part-by-part considering the materials selected based on cost and structural needs. These methods recognize properties of advanced materials that otherwise are neglected in standard weight analysis. For instance, CFRP offers twice the strength at half the weight of 7075 T6 Aluminum. Furthermore, part-by-part analysis is not based on statistical data typically incorporated in empirical weight methods based off statistical data of aircraft over the last 40 years. Hence, the unique design aspects of Azalzan including the 18.35 aspect ratio, folding wing mechanism, heat management system, and full electrical architecture must be accounted for individually. Figure 64 highlights the aforementioned heat management system, folding wing mechanism, and propeller tilting components analyzed separately as part-by-part weight estimation. The following foldout presents the results of the Class III weight estimations as illustrated, exploded weight groups

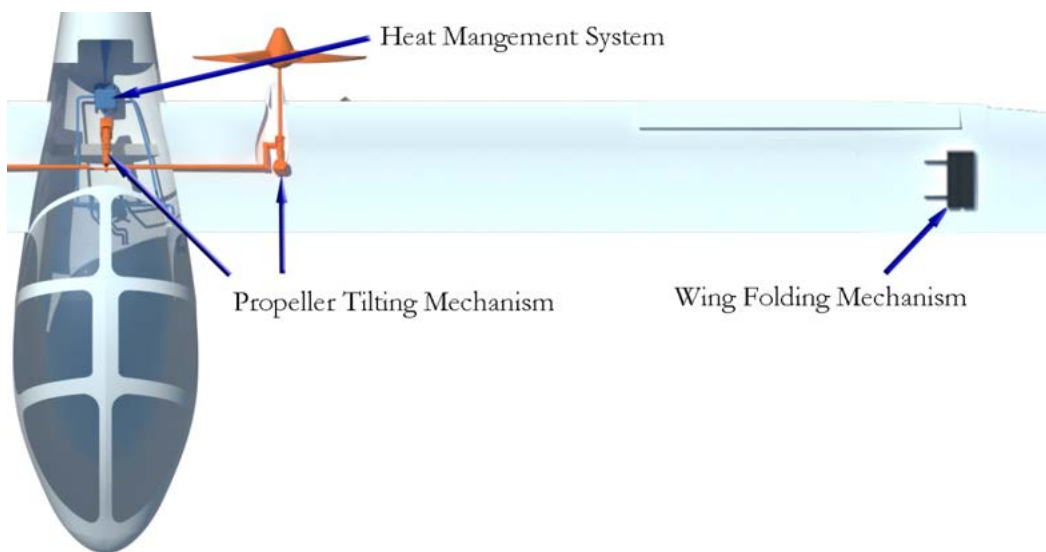


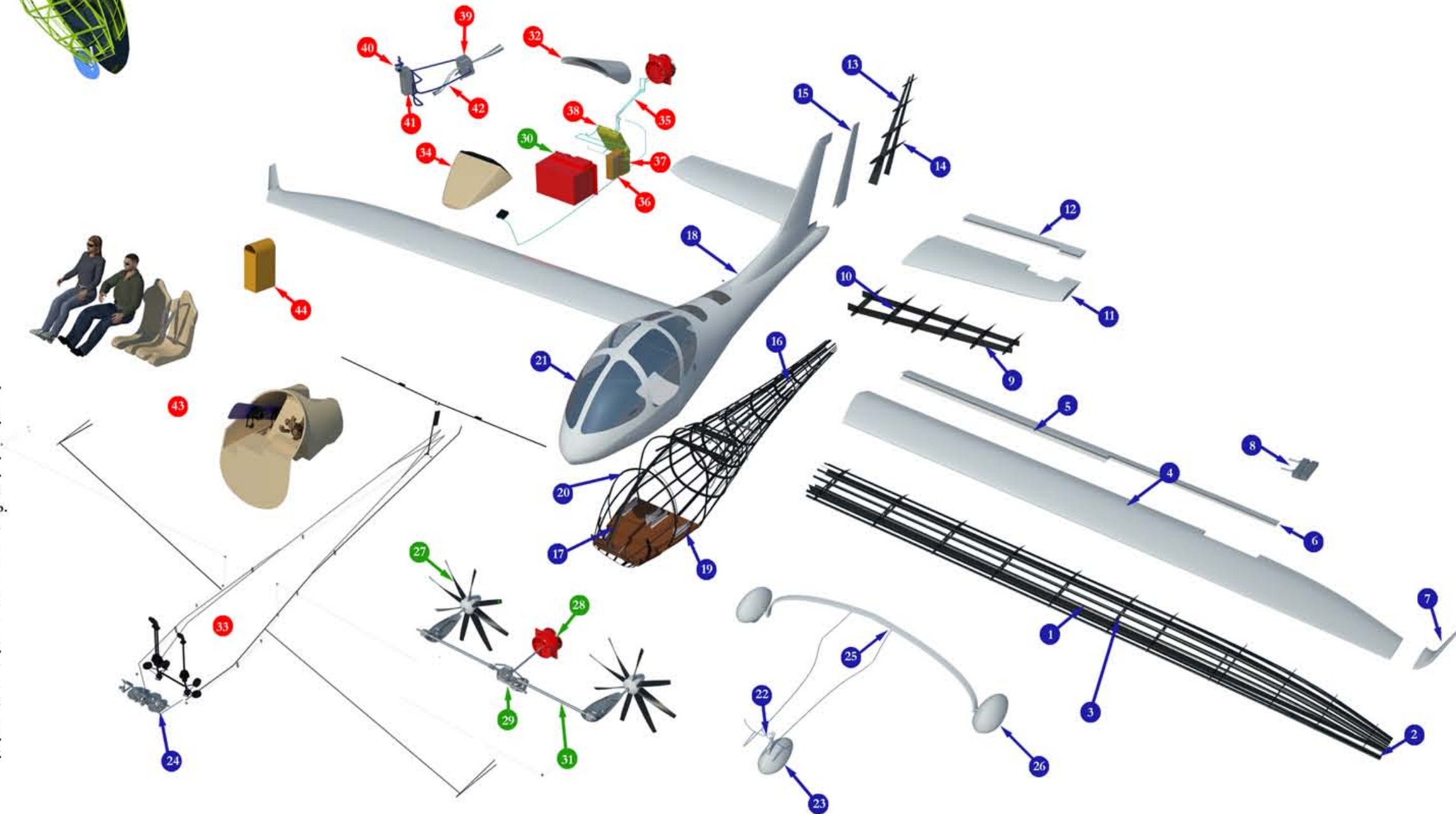
Fig. 64 Highlights of the heat management system, folding wing mechanism, and propeller tilting components



31% ■ CFRP
9% ■ CFRP Sandwich Panel
5% ■ CFRP Honeycomb Panel
35% ■ Aluminum
14% ■ Steel
2% ■ Fiberglass
3% ■ Titanium

1	Wing Spars	43 lb.
2	Wing Longerons	19 lb.
3	Wing Ribs	23 lb.
4	Wing Skin	24 lb.
5	Flaps	19 lb.
6	Wing Aileron	5 lb.
7	Winglets	3 lb.
8	Wing Folding Mechanisms	12 lb.
9	Horizontal Tail Spars	11 lb.
10	Horizontal Tail Ribs	6 lb.
11	Horizontal Tail Skin	5 lb.
12	Elevator Surfaces	5 lb.
13	Vertical Tail Spars	2 lb.
14	Vertical Tail Ribs	4 lb.
15	Rudder	1 lb.
16	Fuselage Frames	21 lb.
17	Fuselage Longerons	15 lb.
18	Fuselage Skin	16 lb.
19	Seat Railing	7 lb.
20	Cockpit Reinforcement	38 lb.
21	Transparencies	19 lb.
22	Landing Gear Strut	3 lb.
	Tires & Rims	30 lb.
	Steering Mechanism	5 lb.
	Leaf Spring	52 lb.
	Landing Gear Fairings	9 lb.
	Propellers	46 lb.
	Propeller Motor	66 lb.
	Propeller Tilting Mechanism	19 lb.
	Li-Air Battery	160 lb.
	Shaft System	41 lb.
	Air Induction System	1 lb.
	Control System	6 lb.
	Avionics	7 lb.
	Wiring	5 lb.
	Charger	4 lb.
	DC-DC Converter	5 lb.
	Motor Controller Unit	22 lb.
	Heat Exchanger	6 lb.
	Coolant Pump	4 lb.
	Coolant	10 lb.
	Piping	5 lb.
	Furnishings	20 lb.
	Parachute Pack	33 lb.

- Structure
- Powerplant
- Fixed Weight



11.4 Center of Gravity Analysis

The center of gravity location was estimated based on the results of the Class III weight analysis and the locations of individual components. The defined location of the airplane empty weight is shown in Table 11, and the airplane's component CG's are located in the component CG side profile in Fig. 65. Tables 12 and 13 show detailed summaries of takeoff weight figures and moments of inertia, respectively.

Table 11 Detailed Takeoff Weight

W_{fix}	141 lb.
$W_{Structure}$	441 lb.
W_{PP}	337 lb.
W_{PL}	400 lb.
W_E	920 lb.
W_{TO}	1,320 lb.
$W_{TO,Extended}$	1,290 lb.
$W_{TO,Light}$	1,070 lb.

Table 12 Empty Weight CG

	Empty Weight	MTOW	Extended	Light
X_{CG}	8.19'	7.12'	7.13'	7.64'
Y_{CG}	0'	0'	0'	0'
Z_{CG}	5.00'	5.00'	4.97'	4.97'

Table 13 Moment of Inertia

I_{xx_B}	13 slug-ft ²
I_{yy_B}	384 slug-ft ²
I_{zz_B}	371 slug-ft ²
I_{xz_B}	31 slug-ft ²

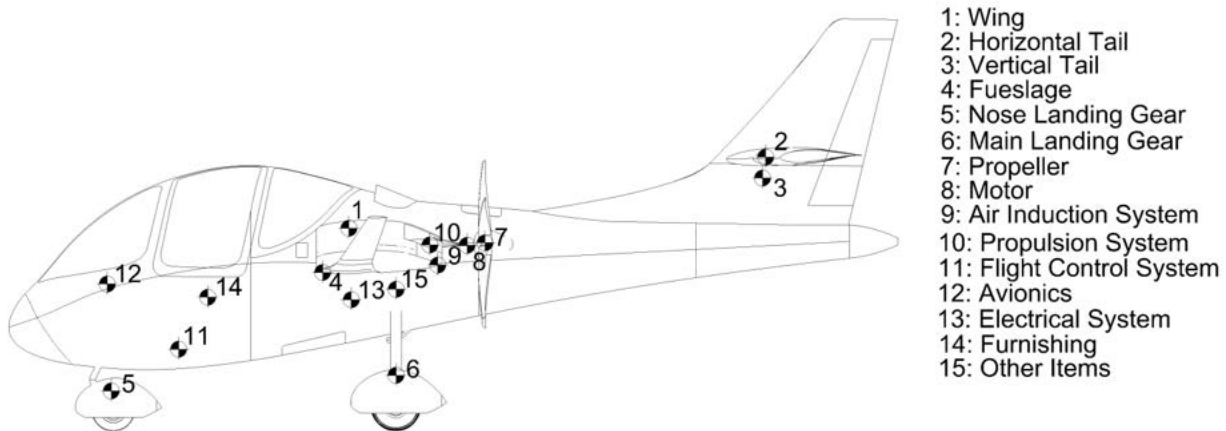


Figure 65 CG locations, side profile

UACC concluded that a longitudinal wing apex of 72" will provide sufficient positive static margin at forward and aft locations of the CG, therefore ensuring the maintenance of the static stability of the aircraft under all loading conditions.

12.3 Tail Sizing and Trim Diagram

The empennage of Azalzan was sized to satisfy basic stability and control requirements set by MIL-F-8785⁵⁴ and recommended by Roskam⁵⁵ as well as being able to initiate the takeoff rotation. MIL-F-8785 recommends that in order to maintain static longitudinal stability, the air vehicle must possess negative values of C_{m_x} and C_{m_z} at all flight conditions. A horizontal tail area of 42.2 ft^2 , capable of maintaining a C_{m_x} and C_{m_z} of at least $-0.2 \text{ rad}'$, was selected by performing a parametric study that varied the area of a generic horizontal tail planform and then computed the corresponding C_{m_x} and C_{m_z} using methods presented by Roskam⁵⁶. A trim diagram was generated assuming it is equipped with an elevator capable of deflecting $\pm 20^\circ$ in order to verify the capacity of the airplane to maintain trim at all loading conditions. This trim diagram can be seen in Fig. 67.

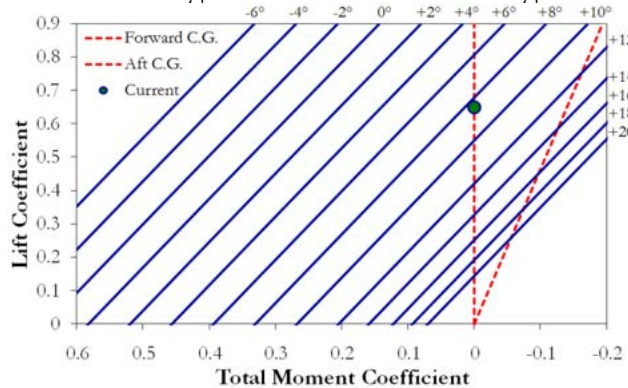


Fig. 67 Trim diagram with current cruise condition

12.4 Stability & Control Derivatives

MIL-F-8785⁵⁷ requires that every aircraft should have a neutral point located behind the most aft center of gravity in order to maintain static longitudinal stability in all flight conditions. The location of the aircraft's neutral point was determined using the method presented by Roskam⁵⁸. A selection of the results with the load case of two 170 lb. passengers and 60 lb. of cargo is presented in Table 14. As it can be seen from this table, the magnitude of the static margin is always positive

indicating that the location of the center of gravity is always ahead of the aerodynamic center of the aircraft in all critical flight segments.

Table 14. Location of CG, aerodynamic center, and corresponding free stick static margin at takeoff, cruise, and landing conditions

Segment	Takeoff	Cruise	Landing
\bar{x}_{cg}	0.2165	0.2165	0.2165
\bar{x}_{ac}	0.7002	0.6603	0.71
SM_{free}	49.74%	38%	51.03%

In order for the aircraft to remain statically stable, the pitching moment coefficient due to the angle of attack (C_{m_a}), and pitching moment coefficient due to angle of attack rate derivative ($C_{m_{\dot{a}}}$) both should be negative. In order to verify the lateral and directional static stability of the aircraft, yawing-moment coefficient-due-to-sideslip derivatives ($C_{n_{\beta}}$), and rolling-moment-coefficient-due-to-sideslip derivatives ($C_{l_{\beta}}$) were computed. As *Roskam* suggests, to maintain lateral and direction static stability, $C_{n_{\beta}}$, should be positive while $C_{l_{\beta}}$ should have a negative value. These derivatives were computed using methods presented by *Roskam*⁷⁶ and can be seen in Table 15.

Table 15. Important longitudinal and lateral-directional static stability derivatives

Segment	Takeoff	Cruise	Landing
$C_{m_a} [rad/l]$	-3.80	-3.09	-3.80
$C_{m_{\dot{a}}} [rad/l]$	-8.42	-7.08	-8.48
$C_{n_{\beta}} [rad/l]$	0.0264	0.0238	0.0255
$C_{l_{\beta}} [rad/l]$	-0.0434	-0.0554	-0.0362

12.5 Aileron Sizing

Due to the acceptability and availability of FAR-23 standards for light general aviation aircraft, guidelines suggested by this code are used to estimate the required size of the ailerons for the aircraft. To perform this estimation, a theoretical approach presented by *Roskam*⁵⁹ was used. In the interests of brevity, this method is not presented in this proposal. The goal of achieving “level I” rolling qualities in the takeoff flight condition was pursued using the rolling time constants suggested by FAR-23. Assuming an individual aileron has a C_a/C_w equal to 20% starting at 47% of the half-span (following the flap), the outboard station of the aileron was calculated to be located at 76% of the half span. This aileron geometry was validated later during the analysis of the lateral directional flying qualities by fulfilling the rolling requirements defined in FAR-23.

12.6 Dynamic Stability

The dynamic stability analysis for Azalzan were performed using *AAA*’s flight dynamics modules and the results for the most important flight segments, specifically takeoff, cruise, and landing, are presented herein. Handling quality analyses performed using the *AAA* package indicates that Azalzan is capable of achieving Level I and Level II flight handling characteristics in all segments of flight. Results are confirming the satisfaction of the regulations presented by FAR-23 and MIL- F-8785 for light airplanes with regard to the time constants and damping ratios, in particular those pertaining to phugoid and short period oscillation modes.

In order to verify longitudinal dynamic stability, dynamic stability derivatives were evaluated along the x , y and z axes to determine the transfer functions and characteristic equations for Azalzan. The methods applied were obtained from USAF Stability and Control DATCOM⁶⁰. Natural frequencies and damping ratios for short period oscillations, and phugoid modes, were calculated based on the methods presented by *Roskam*⁶¹. Values of short period and long period natural frequencies and damping ratios can be seen in Table 16 for takeoff, cruise, and landing conditions.

Table 16. Dynamic longitudinal stability characteristics for various flight conditions

Flight segment:	Takeoff	Cruise	Landing
$T_{\gamma_{2P}} \text{ sec.}$	19.6	65.4	22.8
$Level_p$	I	II	I
$Level_{\zeta_{SP}}$	II	II	II
$\omega_{n,S,P} (\text{rad/sec}^{-1})$	5.61	7.37	4.98
$\omega_{n_P, long} (\text{rad/sec}^{-1})$	0.75	0.34	0.75
ζ_{SP}	0.64	0.57	0.65
$\zeta_{P, long}$	0.05	0.03	0.04

12.7 Propeller Tilting

Analysis was performed to quantify the effects of the propeller tilting system on the pitch down moment of the airplane using methods presented by Roskam⁶². The moment coefficient due to thrust (C_{m_T}) was computed for various flight conditions and can be seen in Table 17.

Table 17. Moment coefficient due to prop-tilting at all flight segments.

Flight segment:	Takeoff	Climb	Cruise	Descent	Loiter	Descent 2	Landing
$C_{m_T(PT)}$	-0.3399	-0.1660	-0.0670	-0.0310	-0.0843	-0.0207	-0.2207

It was concluded that an additional pitch down moment of 120 $lb\cdot ft$ and 128 $lb\cdot ft$ can be generated during takeoff and landing, respectively, which is equivalent to an average increase in horizontal tail area of 1.3 ft^2 . A flight simulation was performed using *X-Plane 9* to validate the capacity of the prop-tilting mechanism to help recovery from low-altitude deep stall situations.

13.0 Performance

13.1 Performance of Installed Powerplant

Based on the methods presented by *Roskam*⁶³, the installed power characteristics of the propulsion system were modeled for the purposes of determining the performance of the aircraft. The properties of the custom-designed propeller, presented in Sec. 8.2, were used in this analysis. The results of the analysis can be seen in Table 18.

Table 18. Installed power characteristics of propulsion system

Flight segment:	Takeoff	Climb	Cruise	Descent	Loiter	Descent 2	Landing
P _{avail, shaft (hp)}	14.2	55.0	28.3	4.0	15.6	4.0	17.6
P _{avail, propeller (hp)}	10.5	38.6	24.9	3.4	12.6	3.4	13.3
Advance Ratio	0.4	0.55	1	0.55	0.55	0.55	0.45
C _p	0.0229	0.0942	0.0522	0.0069	0.0267	0.0069	0.029
η _p	0.77	0.77	0.91	0.90	0.87	0.90	0.76

13.2 Takeoff Performance

The required takeoff field length for Azalzan is determined by applying relations presented by ESDU Data Item 85029⁶⁴ and considering the ground effect on generated lift and drag⁶⁵. It is assumed that the aircraft uses the previously sized flaps during takeoff without assistance from leading edge high lift devices, making the maximum lift coefficient ($C_{L_{max}} = 2.5$) attainable. The average kinetic friction coefficient was computed using the data presented by *Roskam*⁶⁶ to be 0.02, assuming a conventional tarmac mix, as used in the United States.

The takeoff trajectory was computed for normal takeoff and can be seen in Fig. 68. Assumptions regarding takeoff performance computations and the results of this analysis are presented in Tables 19 and 20.

Table 19 Takeoff Condition

$C_{L_{max,TO}}$	2.7
$C_{DO,TO}$	0.2125
$L/D _{TO}$	11.8
Π_{TO}	0.95

Table 20 Takeoff Performance

$V_{S_{TO}}$	36 kts.
V_{LOF}	41 kts.
S_{TO}	600'
$S_{TO,G}$	190'

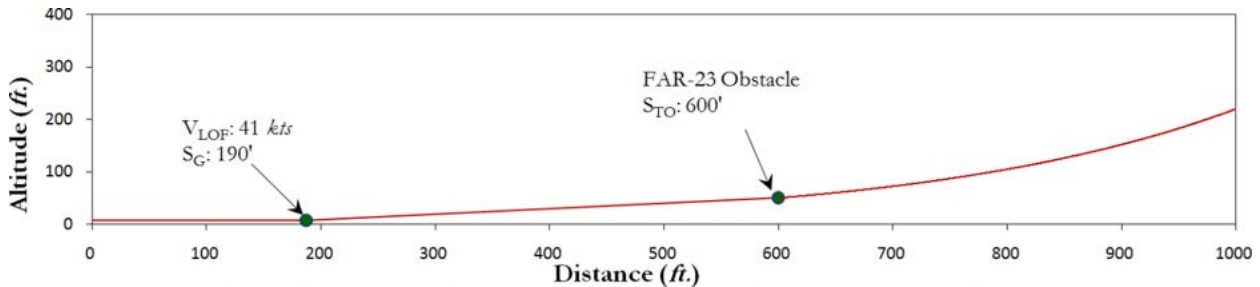


Fig. 68 Takeoff trajectory

13.3 Climb Performance

In order to calculate the maximum rate of climb for Azalzan, and in general, the climb performance of the aircraft relations presented by Roskam⁶⁷ were used. The rate of climb was plotted versus velocity to capture the performance of the aircraft in climb at various altitudes. This graph is shown in Fig. 69. Analyses were performed in order to determine the time required to climb from sea level to 9,500' based on the mission profile presented by the RFP. The results and assumptions for this analysis are presented in Table 21.

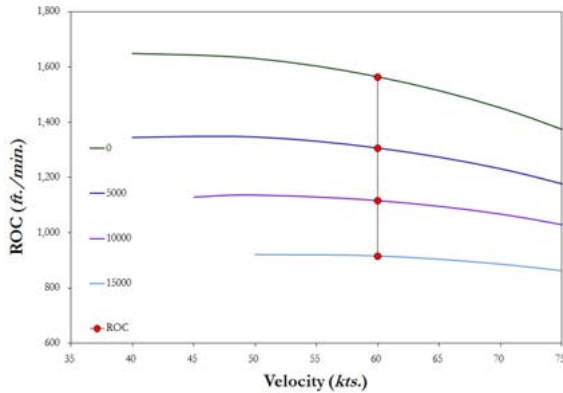


Fig. 69 Climb performance

Table 21 Results of climb performance

Δ_h	9,500'
A	0.56°
R/C	625 fpm
CGR	0.1
$P_{SpExPwr}$	743 fpm
$t(1 \rightarrow 3)$	15.2 min.

13.4 Maximum Cruise Speed

An analysis was performed of the required and available power at cruise for Azalzan. From this analysis it was determined that the maximum possible cruise speed at 9,500' is 151 *kts*. At this velocity, the required power to overcome drag equals the maximum power of the motor. However, the flutter characteristics, presented in Sec. 7.5, and the structural design of Azalzan dictate that the aircraft may not exceed 147 *kts*. This requires an electronic de-rating system to be installed on Azalzan, which would impose a nominal rating of 75% on the maximum power available of the electric motor at cruise.

13.5 Maneuvering Performance

The airplane's instantaneous and sustained pull-up/push-over performance are calculated based on the methods presented by *Roskam*⁶⁸. The analysis was performed to calculate the minimum turn radius, maximum pull-up load factor, and turn rate by plotting the power available, power required, and load factors versus speed. Maximum maneuver capabilities are reached when the amount of excess power is maximized at an airspeed of 117 *kts*. Results of the maneuverability analysis at cruise condition are summarized in Table 22.

Table. 22 Pull-up and Instantaneous turn performance

V _m	80 <i>kts.</i>
Q ₁	0.2727
n _{pull-up}	2.15 <i>g</i>
ψ	62.3°
Turn Rate	0.45 rad./sec.
R _{turn}	300'
n _{turn}	2.15 <i>g</i>

13.6 Endurance

The endurance of the aircraft was computed by estimating the amount of energy required to perform the mission profile presented in Sec. 2.3. A similar method to that presented in Sec 2.3 was utilized to estimate the endurance of the aircraft. However, the most accurate available drag coefficients, obtained from detailed aerodynamic analysis presented in Sec. 6.6, were substituted in place of the preliminary drag coefficients. A summary of this updated energy budget can be seen in Table 23.

Table. 23 Finalized energy budget, updated from detailed aerodynamic analysis

Flight Condition	Altitude (ft)	Speed (<i>kts.</i>)	Detailed Analytic C _D	Duration (min)	Distance Travelled (<i>nmi</i>)	Mechanical Work Performed (Whr)	Energy Fraction
1. Takeoff	0	45	0.1491	10	8	2,300	8 %
2. Typical Climb	4,750	60	0.0658	15	15	8,000	27 %
3. Cruise	9,500	80	0.0219	100	135	14,535	48 %
4. Descent	6,000	60	0.0373	7	7	280	1 %
5. Loiter	2,500	60	0.0359	30	30	3,700	12 %
6. Descent	1,250	60	0.0333	3	3	145	<1 %
7. Landing	0	40	0.2030	3	2	1,040	3 %
TOTAL	-----	-----	-----	168	235	30,000	100 %

It was observed that an endurance of 2.8 *hrs.*, corresponding to a 235 *nmi.* range, can be achieved with a 67 *kW-br* battery onboard. This endurance is extendable to 6.2 *hrs.* with the use of an extended range battery pack (ERP) that may be installed in place of the passenger, as requested by the RFP and discussed in Sec. 14.4.

13.7 Landing Trajectory

The method presented by ESDU Data Items 91032⁶⁹, 92020⁷⁰, and EG6/4⁷¹ was used to estimate the landing distance for the aircraft assuming a Maximum Landing Weight (MLW) of 1,317 *lb.* MLW is defined as the empty weight of the aircraft plus two 170-*lb.* passengers and 60 *lb.* of luggage onboard. The ground effects are taken into account in this analysis, for which the results are presented in detail in Table 24. Figure 70 presents the results of the simulation of the landing trajectory of the aircraft.

Table 24. Landing performance

Δ_n	0.1
$\bar{\gamma}$	3.43°
V_{S_L}	35 <i>kts.</i>
V_A	45 <i>kts.</i>
S_{air}	710'
S_{LG}	290'
S_L	1000'

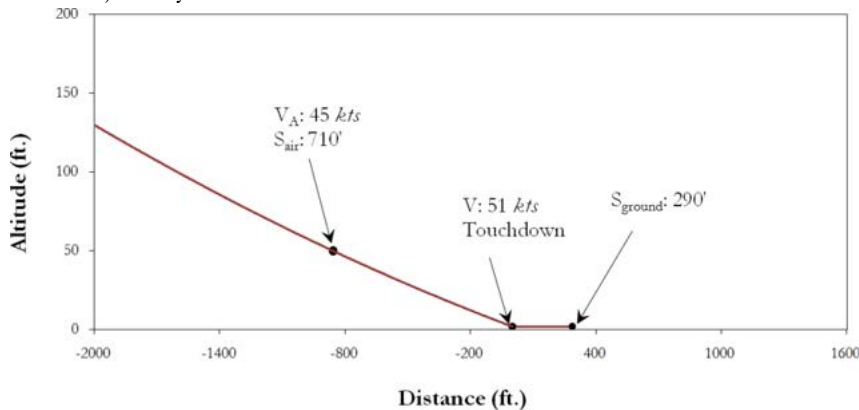


Fig. 70 Landing Trajectory

13.8 Stall Speed

The stall speed is evaluated using the equations presented by Roskam⁷². From these equations, the maximum lift coefficient (including flap effects) of the aircraft was calculated as 2.5, to be achieved at 7° angle of attack. Additionally, the maximum clean lift coefficient in flight conditions not using flaps was determined as 1.9. From the $C_{L\max}$'s, the stall speeds at all flight conditions were able to be calculated. Table 25 presents a summary of the stall speed performance of the aircraft. Azalzan is equipped with a prop-tilting mechanism that allows production of enormous amounts of nose down pitching moment, suitable for recovery from deep stalls.

Table 25. Stall speeds

Flight segment:	Takeoff	Climb	Cruise	Descent	Loiter	Descent	Landing
V _S [kts.]	35	38	54	51	48	47	35

13.9 Noise Assessment

Cabin noise is of crucial interest in determining user comfort level. Post analysis evaluation of readily calculable factors contributing to overall cabin noise level yields the conclusion that the most significant factor in the noise level is the propeller noise. All other noise is at least an order of magnitude smaller by comparison, and under logarithmic addition, will give a small increase on top of the noise level given by the propeller.

The noise level of the propeller measured in-cabin must then be calculated. Using a purely empirical method developed by *Marte et al.*⁷³, the noise due to the propeller (without intervening material such as a windshield) at cruise is computed to be approximately 138 dB.

Constructing the windshield with a sound attenuating glass epoxy of approximately 6mm thickness results in an average of 31 dB attenuation across most of the audible frequency range. This results in an effective sound level of approximately 107 dB. This estimate is said to be accurate to -5 to +9 dB and is substantially quieter than present day SLSAs. This noise level is very similar to the noise levels experienced by commercial jetliner passengers.

Based on a set of simulated measurements taken at these locations (taking both distance and angle of inclination with respect to prop axis during the three critical regimes), the maximum relevant dB levels were calculated at takeoff, approach, and sideline, as presented in Table 26.

Table 26. Summary of Noise results

	Takeoff	Approach	Sideline
Max dB level	29 dB	44 dB	33 dB

14.0 Maintenance & Operations

14.1 T-Hangar & Storage

As requested by the RFP, Azalzan was designed to be stored in a T-hangar. Such storage imposed limitations on the span of the wings, the horizontal tail, and the maximum height of the aircraft. As the design space analysis presented in Sec. 6.2 demanded a relatively high wing span of 50', wing folding was required in order to fit inside a 40' wide T-hanger. This was accomplished through a multi-lug folding mechanism, separating the outboard wingbox from the inboard wingbox, and secured on the surfaces of the front and rear spars of the wingboxes, as well as the upper and lower skin panels. The folding is operated using electro-motors equipped with a worm-gearred mechanism that directs the folding between the direction of the dihedral of the wing and the direction perpendicular to the ground. The folding mechanism is secured before taxi and takeoff by electrically operated latch pins that are inserted into the connector plate installed on both sides of the folding mechanism. Figure 71 presents a structural view of the locking mechanism.

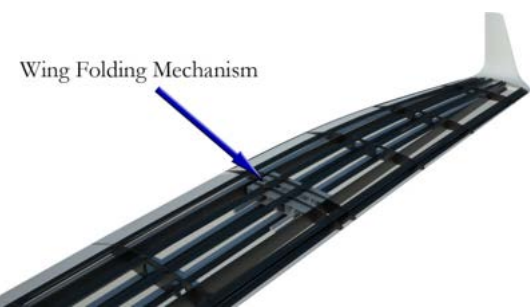


Fig. 71 Wing folding mechanism structure close-up

It was noted that the geometry of the T-hangar is not fully regulated, especially with regards to the height of the hangar. It was observed that T-hangars with minimum heights of 10'-6" are widely available and many T-hangars have door heights exceeding 12'. This geometry ultimately defined the location of the fold line for the wing given a door span of 40', as dictated by the RFP. Figures 72 and 73 present Azalzan stored in a T-hangar.

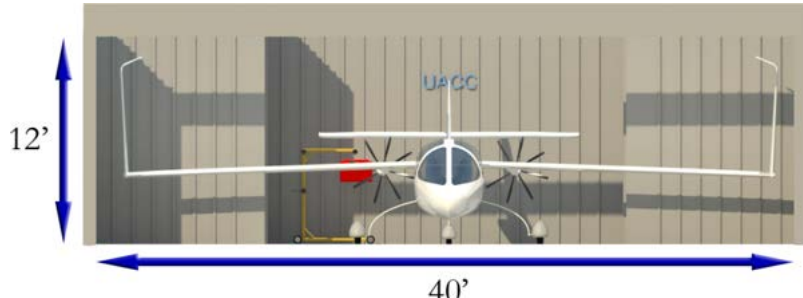


Fig. 72 Front view of T-hangar storage



Fig. 73 Isometric view of T-hangar storage

14.2 Battery Recharging Performance

As mentioned in Sec. 9.1, Azalzan has an onboard battery charger for use during ground operations. In order to minimize the charging time while maximizing the compatibility with the current electrical grid, the SAE J1772 electrical connector standard⁷⁴ was adopted in Azalzan. This standard allows for a maximum charging power 19.2 kW when connected to a 240 VAC socket, which is standard and widely available. This will result in a full charge in 3.8 hrs. Figure 74 shows the onboard charger located in the mid fuselage.

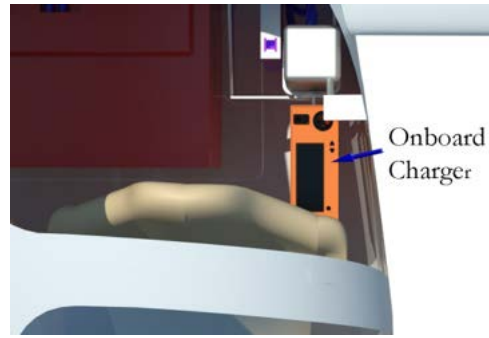


Fig. 74 Location of the onboard charger

14.3 Battery Lifecycle & Replacement

As part of the product lifecycle evaluation of Azalzan, an estimation of the durability of the battery was performed. For this purpose, UACC contacted a leading expert in the field of advanced Li-air battery technology, *Dr. Binod Kumar*, regarding the maximum charge-discharge cycles and shelf life of Li-air batteries. In private correspondence with *Dr. Kumar*, an estimated 500 charge cycles and five year shelf life was determined to be achievable with this battery technology.

Even though lithium is corrosive and may be hazardous for the environment, the manufacture and operation of Li-air batteries have proven to be both environmentally conscious and safe for human use in a wide range of applications. Furthermore, the solid-state nature of Li-air batteries makes them safe even when subject to punctures or other mechanical failures⁷⁵. A means for disposing the battery is necessary due to the use of lithium as the anode material of the battery. However, given the wide use of lithium-ion and other types of lithium-based batteries, there is an established infrastructure to take care of the batteries once their end-of-life is reached. It should be noted that apart from regular verification of the correct functioning of the battery and its charge level indicator, the Li-air battery does not required any scheduled maintenance throughout its lifecycle.

14.4 Extended Endurance Battery Package

As required by the RFP, Azalzan has the option of installing an additional battery pack in place of a passenger in order to increase range for single-pilot operations. In order to utilize economies of scale and reduce the overall cost of producing the batteries, UACC decided that the ERP would be identical to the main battery pack. As a result, the battery accessories will be common, which simplifies maintenance by reducing the number of spare parts required. This feature also allows the ERP to be used as a replacement for the main battery when it has reached its end-of-life.

When installed, the additional battery provides energy for an extended range of 510 *nmi*, 275 *nmi* longer than the standard 235 *nmi* block range. In order to install the extended range pack (ERP), the passenger-side seat and stick must be removed so that space can be made available for safe operation. Given that the ERP is used to increase energy capacity, but not the overall power of the aircraft, the use of dedicated cooling and control systems for each battery is not required. Instead, the installation of the ERP only requires use of two connections for power and coolant, without the need to install additional cooling or control systems.

To aid the installation of the ERP, a small, light-weight personal-use crane is available, which can be used to lift and transport the battery from storage to its final location in the plane, and vice versa. Once the battery has been positioned, it is fastened in place to guarantee safe operation during flight. The final phase of installing the ERP is securing the electric and coolant connections. Figures 75 and 76 show the ERP installation process and the cockpit with the ERP installed.

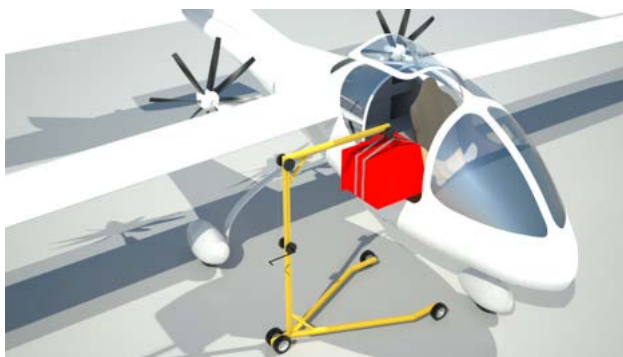


Fig. 75 ERP installation process with a light-weight, personal use crane

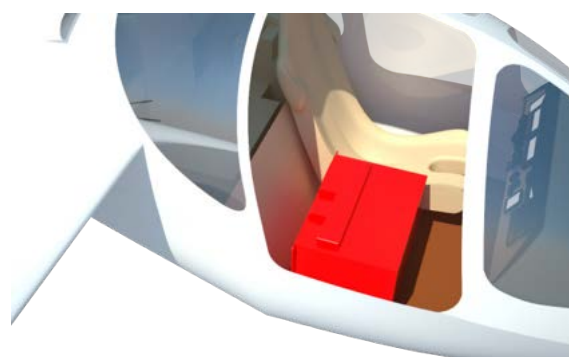


Fig. 76 Cockpit with ERP installed

14.5 Regular Inspections

One of the advantages of electric over conventional aircraft is the reduction in the number of components and systems that require regular inspections and service, such as fuel and lubricating systems. Furthermore, the inspection of electric and electronic components is usually simpler than that of equivalent mechanical systems⁷⁶. Such is the case of the electric motor and battery for which computerized tests can be performed to assess airworthiness. A preflight automatic test is used in Azalzan to ensure the correct functioning of the electric and electronic components. The airplane also has access panels that allow for inspection of electrical and mechanical components, including the propeller tilting mechanism, the electric motor, the battery, the charging system, the wing folding mechanism, and the cooling system. Figure 77 shows the location of the access panels.

Access Panels

- | | |
|----------------------|---------------------------|
| 1: Battery | 3: Motor |
| 2: Charger & Coolant | 4: Wing Folding Mechanism |

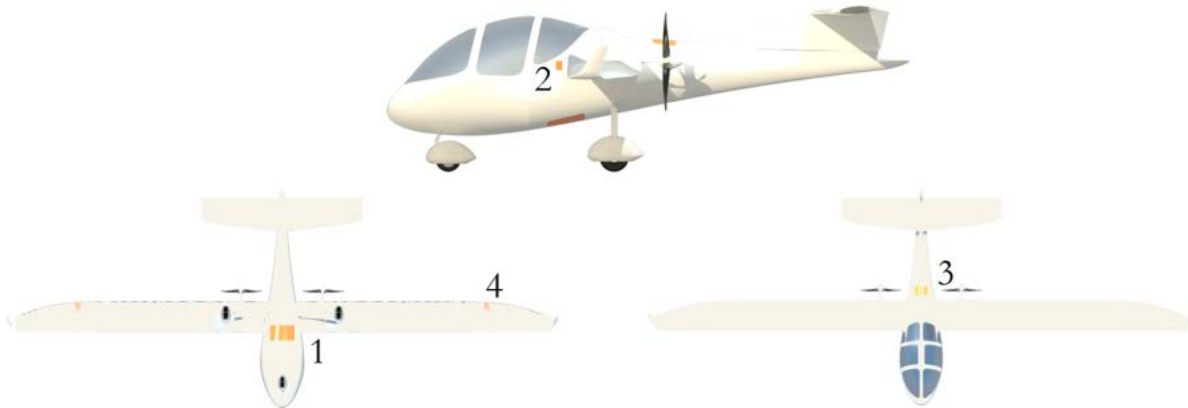
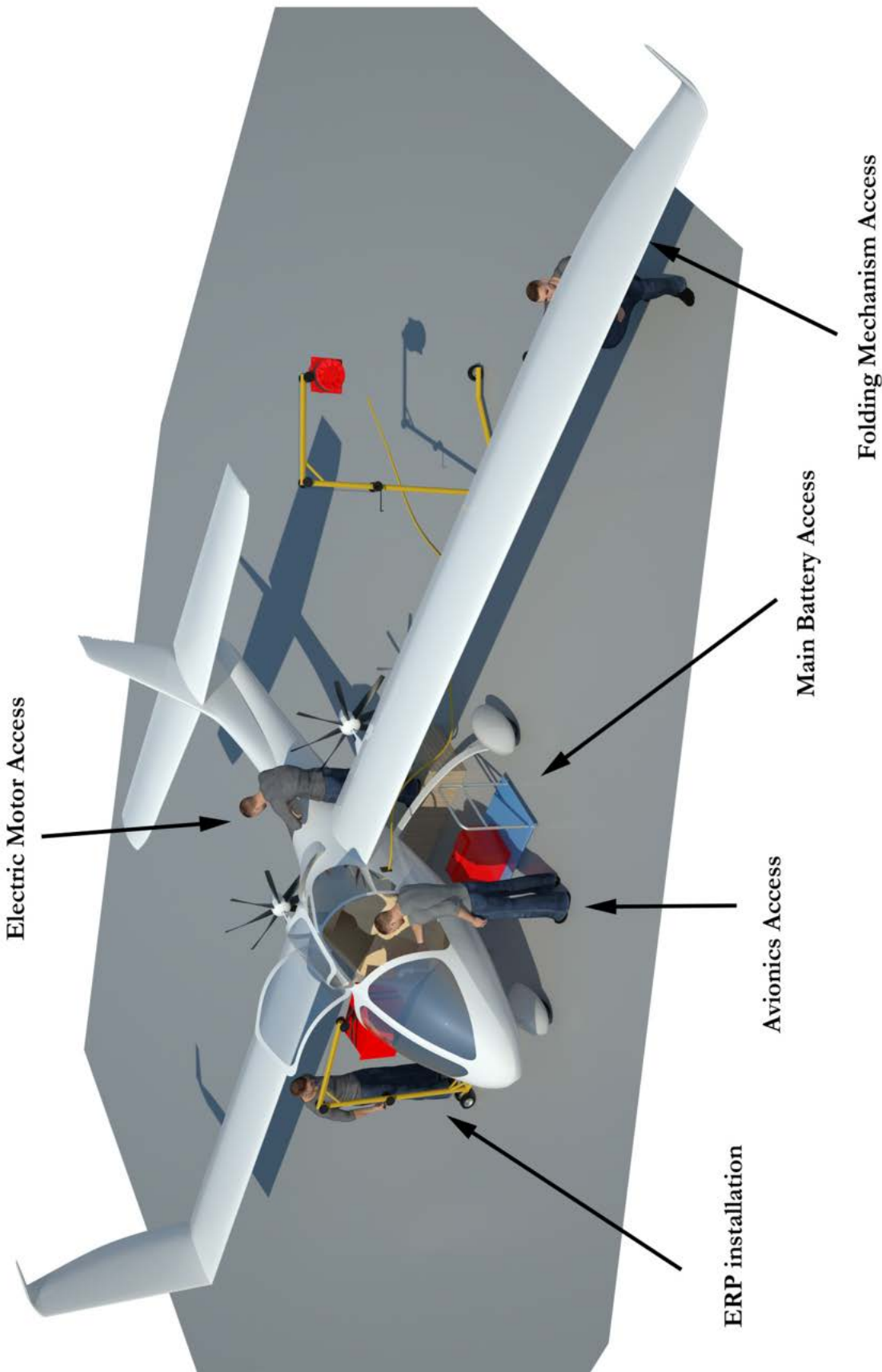


Fig. 77 Access Panels

14.6 Accessibility Picture



15.0 Safety Features and Analysis

15.1 Deep Stalls and Propeller Tilting

Reviewing the information regarding general aviation accidents published by the NTSB, it was observed that approximately 50% of the accidents of personal general aviation aircraft occur during takeoff and landing phases of flight⁷⁷. Seeing as these flight phases involve lower speeds, higher angles of attack, and lower altitudes, deep stall may be one of the primary causes. Therefore, an innovative system that can assist the pilot from recovering excessive angles of attack at low speed and altitude may improve the safety of the aircraft. UACC introduced a novel propeller tilting system that accomplishes this task, as explained in Sec. 5.4. This system autonomously detects deep stalls and increases the propeller inclination angle to produce a nose-down moment (depending on the airplane attitude) to assist stall recovery.

15.2 Parachute Deployment

In order to improve the overall crash survivability, a parachute airframe recovery system was designed and implemented following the methodology presented by *Knacke*⁷⁸. A 14.3% extended skirt canopy was selected given its performance for the sport aircraft application, i.e. high drag coefficient and low angle of oscillation (less than 15°). A descent rate of 25 ft./sec. was chosen following *Knacke's* recommendation for the design of the parachute. The designed parachute has a nominal diameter of 42' and is constructed of rip-stop nylon sized to recover the aircraft at dive speed and maximum weight. The parachute package is located in the central fuselage from where the parachute canopy is deployed by a *Cesaroni* Pro 29⁷⁹ solid rocket motor that pulls the canopy through the intake located on the upper fuselage. The parachute is attached to the airframe at three points, two of which are attached to the rear wing spar near the wing roots. A third riser is attached to the foremost fuselage frame and breaks through the skin of the aircraft along the fuselage centerline when the parachute is deployed. Figures 78 and 79 on the following page show the geometry of the deployed canopy and the parachute package in the fuselage. The design was validated by comparing

the resulting dimensions and characteristics with those of commercially available parachute recovery systems manufactured by *BRS Aerospace*⁸⁰.



Fig. 78 Deployed canopy

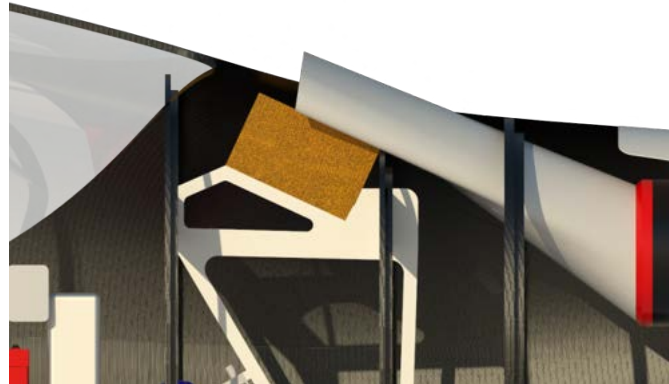


Fig. 79 Parachute package inside the mid fuselage. To facilitate deployment of the parachute, the intake is especially designed with weakened regions.

15.3 G Seats, Seatbelts, and Airbags

The cockpit is outfitted with high-G, ergonomic, lumbar-supported seats based on the *Oregon Aero* High-G Seat, which passes the 19-G lumbar load survivability test required for certified general aviation aircraft⁸¹. This seat increases the crash survivability and passenger safety by protecting the occupants from severe injury and from becoming trapped due to excessive seat deformation. A four-point *AMSAFE* airbag seatbelt system was selected to further improve safety and crash survivability. Figure 80 shows the cockpit G-seats and seatbelts.



Fig. 80 Cockpit G-seats and seatbelts

15.4 Wings Folded

Considerations were made for the unlikely scenario in which the pilot must perform a takeoff or landing maneuver with folded wings. As the Azalzan configuration has the ailerons located inboard of the folding section of the wing in case of such mishap, the craft maintains all modes of control and only flight dynamics and performance are slightly influenced. In order to quantify these effects, flight simulations were performed using *X-Plane 9*⁸², replicating a hot day (ISA+20 °C) takeoff from a runway at 2,000' altitude with the wingtip sections completely folded.

Figure 81 presents a snapshot of the virtual aircraft during the flight dynamic simulation. The analysis showed that Azalzan can achieve a roll rate of $15^\circ/\text{sec}$, a climb rate of $1,350 \text{ fpm}$, and a sustained turn rate of $3.2^\circ/\text{sec}$. while flying with folded wings. The general behavior of the airplane was satisfactory and the spiral modes at low altitude and low speed were improved due to the increase in the side area of the airplane.



Fig. 81 Wings folded flight dynamic simulation

15.5 Lightning Strike

Considering the heavy use of composites in the structure of Azalzan, it is realized that a low-altitude lightning strike will present a serious threat to the integrity of the aircraft. This is caused by the non-conductive nature of composites, which results in significant structural damage when subject to high electric current. This damage is caused by high temperatures that result from the accumulation of charge in the structure at the strike point⁸³. To remedy this issue, a network of conductors can be utilized or conductive material may be embedded in the CFRP composite matrix. Also, parts of the structure that have a higher probability of being struck by lightning (especially wingtips and the tips of empennage surfaces⁸⁴) may be manufactured from metallic material to facilitate current transfer locally⁸⁵. Azalzan implements both approaches by having aluminum tips for the wing and empennage and an embedded copper mesh to improve the conductivity of the CFRP material.

16.0 Cost & Risk Analysis

16.1 Market Forecast

The LSA category was introduced by the FAA in 2004 with the implementation of Rule 69 FR 44772⁸⁶. Since then, over 7,000 aircraft and 120,000 pilots have been registered or certified in the US in the LSA category. The FAA forecasts an average long-term annual growth of 3.3% in the LSA fleet in the US and 6.1% in the number of sport pilots⁸⁷. Figure 82 shows the number of LSA-type aircraft and pilots forecasted by the FAA for 2005-2031. From this data, an average of 300 new LSAs will be added to the US fleet each year starting in 2013.

Considering that North America accounts for 53.4% of the total worldwide market for small aircraft⁸⁸, UACC expects a worldwide market of over 600 LSA-units per year.

Assuming a 20-year production run of 500 or 1,500 aircraft would result in an average of 25 or 75 aircraft per year, respectively. From the projected worldwide annual sales of LSAs, an 4% to 12.5% market share is achievable depending on the rate of production. Given the ever-rising cost of aviation fuel and very low operating costs of an electric airplane, Azalzan is expected to present a significant market advantage over competitor S-LSAs.

16.2 Project Risk Assessment

UACC has determined that the highest development risk item from the standpoint of the project schedule for Azalzan is the Li-air battery pack. Correspondence with present-day developers indicates that they have high certainty of the pack being available well in advance of the 2016 entry into service for Azalzan. However, should this projection fail to materialize, i.e. there is a delay in the development or certification of the battery, alternatives must be considered. There will be two options for Azalzan, the first of which is to use readily available alternative battery technologies that may cause a significant reduction in the range and endurance of the aircraft due to their higher

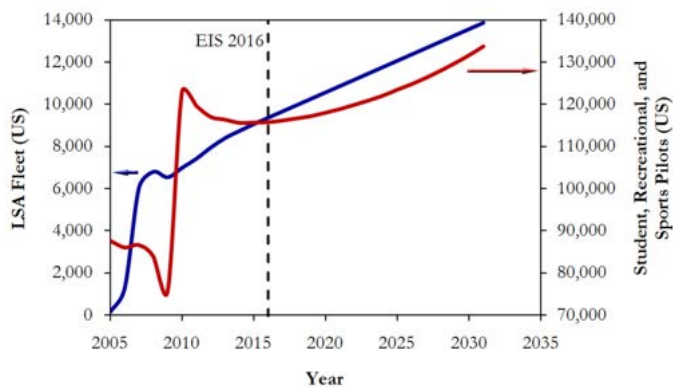


Fig. 82 Results of number of LSAs and pilots forecasted from 2005-2031

weight and reduced energy capacity. UACC has considered other possible battery technologies that could be applied in Azalzan, including lithium-ion and zinc-air. Li-ion batteries have been developed and are approaching their maximum practical capacity⁸⁹, which is around four times smaller than that of Li-air batteries. This would result in an increase of approximately 560 *lb.* to store the same amount of energy, which would result in a significant reduction in range and endurance. Rechargeable zinc-air batteries have been developed, and companies such as *ReVolt* are already planning on commercializing this type of battery in the near future⁹⁰. Zinc-air batteries can store a similar amount of energy per unit volume as Lithium-air batteries⁹¹, which will make it possible to have the same size of battery as the one already designed. However, given the larger weight of Zn-air batteries, the range and endurance would be reduced by about 12.5 %. This would result in a maximum range of 205 *nmi.* and a maximum endurance of 2.5 *hrs.* for a Zn-air battery version of Azalzan. It should be noted that this version of Azalzan would still fulfill the RFP endurance requirements.

The second option is to delay the entry-into-service date to allow for the maturation of the Li-air battery technology. This option presents the lowest risk of meeting the performance target for the aircraft, which is a crucial marketing advantage for Azalzan. However, it would increase the development costs and may delay and reduce the return on the original investment.

16.3 Itemized Cost Estimation

To obtain the most accurate estimation of the unit cost of Azalzan, a method was synthesized using parts of methods presented by *Roskam* and the *RAND Corporation*. The method presented by *Roskam*⁹² is applicable only to aircraft with metallic structures. This requires a modification to capture significant features of this aircraft that are otherwise unaccounted for, such as the extensive use of composite materials. For this purpose, parts of a methodology developed by the *RAND Corporation*⁹³ were used. This methodology assesses the effect of the type of the structural materials on the overall airframe cost by assigning complexity and cost factors to each material relative to aluminum. The method then calculates projected component costs of engineering,

tooling, materials, and labor based on the weight and type of raw material used. The method presented limitations given its publication date and the type of aircraft considered for the derivations (mainly fighter aircraft with weights greater than 10,000 lb.).

The empirical equations presented by *Roskam* were modified with the complexity factors from *RAND* to obtain accurate projected costs for each component from design to manufacture. The itemized cost breakdown for a production run of 500 aircraft is presented in table on the following page. In order to obtain flyaway costs, the itemized cost estimation process was repeated assuming different production runs as presented in Fig. 83. Flyaway costs of \$300,000 and \$150,000 were obtained for 100 and 500-unit production runs, respectively, using a US labor rate. Using a China labor rate, flyaway costs of \$196,000 and \$100,000 were obtained for 100 and 500 unit production runs, respectively. A detailed flyaway cost calculation for a production run of 500 units is shown in table 27.

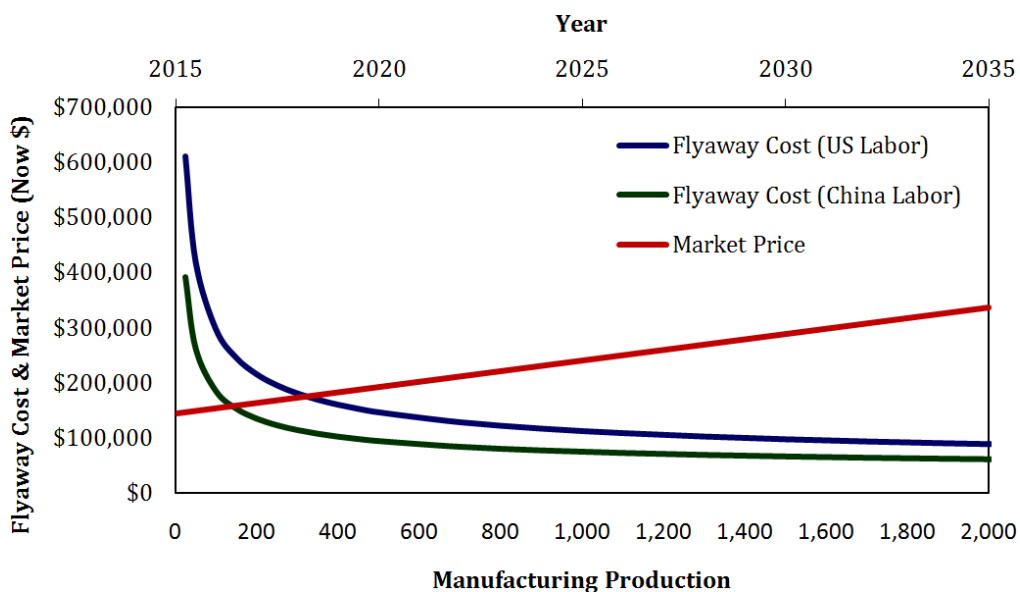


Fig. 83 Flyaway Cost and Market Price at varying manufacturing productions, using US and Chinese labor rates.

Table 27 Flyaway cost calculation for a production run of 500 Units.

#	AMPR Weight (Reference)	Weight (lb)	Material Composition (%)	Nonrecurring Engineering Hour for 500 Units (Hours)	Nonrecurring Tooling Hour for 500 Units (Hours)	Recurring Engineering Hour for 500 Units (Hours)	Recurring Tooling Hour for 500 Units (Hours)	Manufacturing Labor Hour for 500 Units (Hours)	Quality Assurance Hour for 500 Units (Hours)	Recurring Material Cost for 500 Units (\$)	Purchase Cost for 500 Units (\$)
1	Component	579	Aluminum	Titanium	Steel	CFRP	Fiberglass	6627.64	41966.00	18204.64	96517.84
1	Wing	63.00	0	0	100	0	786.05	5388.17	2426.50	15227.81	83960.44
	Wing Spars and Longerons	23	0	0	100	0	286.97	1967.11	885.86	5559.36	30652.22
	Wing Ribs	24	0	0	100	0	299.45	924.38	5801.07	31984.93	1039.51
	Wing Skin	5	0	0	100	0	62.38	427.63	192.58	1208.56	6663.53
	Wing Aileron	19	0	0	100	0	237.06	1626.00	731.80	4592.62	28321.40
	Wing Flap	12	0	0	100	0	149.72	1026.32	462.19	2900.54	15982.47
	Folding Mechanism	3	0	0	100	0	37.43	286.58	115.55	725.13	2079.02
	Winglet	15	100	0	0	0	171.70	1087.20	450.45	2887.84	519.76
2	Horizontal Tail	11	0	0	100	0	137.25	940.79	423.67	2658.82	14659.76
	H Tail Spar	6	0	0	100	0	74.86	513.16	231.10	1450.27	1039.51
	H Tail Rib	5	0	0	100	0	62.38	427.63	192.58	1208.56	6663.53
	H Tail Skin	5	0	0	100	0	62.38	427.63	192.58	1208.56	6663.53
	Elevator	5	0	0	100	0	37.43	256.68	115.55	725.13	2079.02
	Elevator Tab	0.3	0	0	100	0	3.74	72.55	31.98	1380.60	51.98
	Horizontal Tail Adapter	3	0	100	0	0	34.34	256.58	102.81	635.12	3851.25
3	Vertical Tail	1	0	0	100	0	12.48	85.53	38.52	241.71	1332.71
	V Tail Spar	1	0	0	100	0	24.95	171.05	77.03	483.42	2665.41
	V Tail Rib	2	0	0	100	0	37.43	256.58	115.55	725.13	346.50
	V Tail Skin	3	0	0	100	0	37.43	256.58	115.55	725.13	346.50
	Rudder	5	0	0	100	0	12.48	85.53	38.52	241.71	1332.71
	Adapter	2	0	0	100	0	24.95	171.05	77.03	483.42	2665.41
4	Fuselage	23	0	0	100	0	286.97	1967.11	885.86	5559.36	30652.22
	Fuselage Frame	23	0	0	100	0	187.15	1282.90	577.74	2598.67	19990.58
	Fuselage Longeron	15	0	0	100	0	199.63	1386.42	616.25	3867.38	21332.29
	Fuselage Skin	16	0	0	100	0	80.13	598.69	239.90	1481.94	8986.24
	Seat Railings	7	0	100	0	0	454.55	787.19	1248.54	7474.71	5858.03
	Cockpit Reinforcements	38	0	0	100	0	324.17	2209.19	890.42	6521.21	33159.89
	Transparencies	24	0	0	100	0	324.17	2209.19	890.42	6521.21	33159.89
5	Propeller System	46	0	0	100	0	573.94	3934.22	1771.73	61304.45	7969.58
	Propeller	46	0	0	100	0	237.06	1625.00	731.80	4592.62	28321.40
	Tilting System	19	0	0	100	0	237.06	1625.00	731.80	4592.62	28321.40
6	Air Induction System	66	0	0	100	0	513.16	231.10	1450.27	7966.23	1039.51
	Intakes	1	0	0	100	0	513.16	231.10	1450.27	7966.23	1039.51
7	Flight Control System	1	0	0	100	0	74.86	513.16	231.10	1450.27	7966.23
	Control Systems & Equipment	6	0	0	100	0	74.86	513.16	231.10	1450.27	7966.23
8	Nose Landing Gear	6	0	0	100	0	34.34	217.44	90.08	477.59	3116.90
	Strut	3	100	0	0	0	34.34	217.44	90.08	477.59	3116.90
	Fairing and Tire	3	0	0	0	100	40.52	276.15	111.30	815.15	4144.99
	Electromechanical Steering	5	0	0	100	0	34.34	217.44	90.08	477.59	3116.90
9	Tire & Rim	10	0	0	100	0	40.52	276.15	111.30	815.15	538.85
	Main Landing Gear	10	0	0	100	0	40.52	276.15	111.30	815.15	538.85
	Leaf Spring	52	0	0	0	0	87.80	598.32	241.16	1766.16	8980.80
	Fairing, tire and Breaking	6.5	0	0	0	100	87.80	598.32	241.16	1766.16	8980.80
	Hydraulic & Breaking System	6	0	0	0	0	87.80	598.32	241.16	1766.16	8980.80
10	Tire & Rim (x2)	20	0	0	100	0	40.52	276.15	111.30	815.15	538.85
	Cooling System	3	0	0	100	0	40.52	276.15	111.30	815.15	538.85
	Heat Exchangers	6	0	0	100	0	40.52	276.15	111.30	815.15	538.85
	Coolant & Pump	14	0	0	100	0	40.52	276.15	111.30	815.15	538.85
	Coolant Pump & Piping	5	0	0	100	0	40.52	276.15	111.30	815.15	538.85
11	Electrical System	5	0	0	100	0	87.80	598.32	241.16	1766.16	8980.80
	Wiring	5	0	0	100	0	87.80	598.32	241.16	1766.16	8980.80
	Circuit Breaker	4	0	0	100	0	87.80	598.32	241.16	1766.16	8980.80
	DC/DC Converter	5	0	0	100	0	87.80	598.32	241.16	1766.16	8980.80
	Power Control	22	0	0	100	0	87.80	598.32	241.16	1766.16	8980.80
	Avionics (Garmin GTN650)	7	0	0	100	0	87.80	598.32	241.16	1766.16	8980.80
	Battery (Li-Aif)	160	0	0	100	0	87.80	598.32	241.16	1766.16	8980.80
12	Furnishings, Safety & Etc.	25	0	0	100	0	87.80	598.32	241.16	1766.16	8980.80
	Cockpit Accessories	25	0	0	100	0	87.80	598.32	241.16	1766.16	8980.80
	Sunshade	1	0	0	100	0	87.80	598.32	241.16	1766.16	8980.80
	Parachute	33	0	0	100	0	87.80	598.32	241.16	1766.16	8980.80
	Paint	3	0	0	100	0	87.80	598.32	241.16	1766.16	8980.80
	Total Hours	50993.13					34660.65	15326.09	96562.84	69735.23	\$1,988,411.83
	Total Cost	\$412,009.58					\$2,447,041.95	\$1,238,347.84	\$6,817,336.84	\$10,728,496.32	\$4,574,630.83
	Unit Cost	\$100,522.55					China Labor Rate				
	Unit Cost	\$149,979.92					US Labor Rate				

16.4 Operating Cost

A revised version of the method of estimating operating cost for piston-engine aircraft presented by *Roskam*⁹⁴ was applied to Azalzan. A modification was made to take into account the use of electricity instead of fuel as the source of energy for the aircraft. It was assumed that electricity was purchased at a rate of 0.07 USD/kW-hr. based on the current market price of electricity for industrial applications⁹⁵. Table 28 presents a breakdown of operating costs for Azalzan compared to the Cessna 162 and the Breezer 600L, which are similarly sized piston-engine LSAs. The comparison airplanes were analyzed using the *Roskam* method mentioned above for single-engine piston airplanes assuming an aviation fuel price of 5.25 USD/gal.⁹⁶.

Table 28 Breakdown of Operating Costs

Cost Item	Cessna 162	Breezer 600L	Azalzan	Average Change from Conventional Competitors (Cessna 162, Breezer 600L)
Annual Utilization (nm.)	43,640	38,640	33,560	-----
Crew (\$/nm.)	0	0	0	0
Fuel, Oil & Env. Tax (\$/nm)	0.35	0.21	0.02	-94.3%, -90.5%
Insurance (\$/nm.)	0.05	0.05	0.09	+50%, +50.0%
Maintenance (\$/nm.)	0.29	0.32	0.24	-17.2%, -25.0%
Depreciation (\$/nm.)	0.26	0.30	0.33	+26.9%, +10.0%
Landing & Navigation Fees (\$)	0.01	0.02	0.02	-----
Total DOC* (\$/nm.)	1.03	0.96	0.75	-27.2%, -21.9%

References

- ¹Roskam, Jan., Airplane Design, Part I through VIII , DAR Corporation, 2003
- ²Heinemann, E., Raussa, R. and Van Every, K., Aircraft Design, The Nautical and Aviation Publication Co., 1985
- ³Eppinger, Steven D. and Ulrich, Karl T., Product Design and Development, Second Edition, Irwin McGraw-Hill, Boston, 2000
- ⁴Roskam, Jan. Airplane Design Part I Sec. 341 p. 118-187. DAR Corporation. 1987
- ⁵Roskam, Jan. Airplane Design Part II Fig. 12.7 p.286. DAR Corporation. 1997
- ⁶“Engineering Science Data Unit”. *Volumes on Performance*, item 73018. “Estimation of Cruise Range: Propeller-Driven Aircraft.”August 1975
- ⁷K. M. Abraham. A Brief History of Non-aqueous Metal-Air Batteries. ECS Transactions, 3(42) 67-71. 2008
- ⁸MIT Professor
- ⁹Yuneec International. Power Drive System Specifications. Acquired May 2011.
http://yuneeccouk.site.securepod.com/PowerMotor_Tech_spec.html
- ¹⁰ Per suggestion of Dr. Lutgard C. De Jonghe, Faculty Senior Scientist at Lawrence Berkeley National Laboratory and Chairman of PolyPlus Battery Company
- ¹¹ Appendix to Request for Proposal Document for Individual Aircraft Design Competition. AIAA. 2006-2007
- ¹² University of Dayton Research Institute. Energy Storage & Generation. Electromechanical Power. Group Leader/Distinguished Research Engineer. Professor in the department of Aerospace and Mechanical Engineering, University of Dayton, OH.
- ¹³ Roskam, Jan. Airplane Design Part I Sects. 3.1-3.6 pgs 90-168. DAR Corporation 1997
- ¹⁴ “Engineering Science Data Unit”. *Volumes on Aerodynamics*, item 95021. “Wing Lift Coefficient Increment at Zero Angle of Attack”
- ¹⁵ FAA. “Aerospace Forecast Fiscal Years 2010-2030”. page 47
- ¹⁶ General Aviation Manufacturers Association. Industry Facts and Statistics. Statistical Databook and Industry Outlook publications 1999-2011. Acquired March 2011. <http://www.gama.aero/media-center/industry-facts-and-statistics/statistical-databook-and-industry-outlook>
- ¹⁷ Dan Johnson, President and Chairman of the Light Aircraft Manufacturers Association. Market Sales Information for LSA. Acquired March 2011. <http://www.bydanjohnson.com/index.cfm?b=1&m=5>
- ¹⁸ FAA. General Aviation and Part 135 Activity Surveys – CY 2009. Table 1.1. Acquired March 2011.
http://www.faa.gov/data_research/aviation_data_statistics/general_aviation/CY2009/
- ¹⁹Roskam, Jan. Airplane Design. Part III. DAR Corporation. 2003. Pgs 252-253
- ²⁰Roskam , Jan. Roskam’s Airplane War Stories. DAR Corporation. 2002. Pg 82: Cessna 172’s sales have been increased by almost 30% as a result of similar changes affecting the look of the design.
- ²¹Roskam, Jan. Airplane Design Part IV. DAR Corporation, 1997.
- ²²Redeker, G., Horstmann, K.H., Köster, H., and Quast A. Investigations on High Reynolds Number Laminar Flow Airfoils. Journal of Aircraft Vol. 25 № 7. July 1988.
- ²³University of Illinois at Urbana-Champaign Applied Aerodynamics Group. Department of Aerospace Engineering. Airfoil Coordinates Database. Acquired Sept-Dec. 2009.
- ²⁴Roskam, Jan. Airplane Design Part VI. DAR Corporation. 1990. Section 4.12.2, pgs 110-111
- ²⁵Oberg, Eric, et. al. Machinery’s Handbook. Industrial Press. 28th Edition. Feb 2008
- ²⁶“Engineering Science Data Unit”. *Volumes on Aircraft Aerodynamics*, item 98013. “Aerodynamic Principles of Winglets.” June, 1998.
- ²⁷ Maughmer, Mark D. Design of Winglets for High-Performance Sailplanes. AIAA Journal of Aircraft. Vol. 40 № 6. Dec. 2003
- ²⁸“Engineering Science Data Unit”. *Volumes on Aerodynamics*, item 95021. “Wing Lift Coefficient Increment at Zero Angle of Attack”
- ²⁹Roskam, Jan. citing Torenbeek, E. Synthesis of Subsonic Airplane Design. Appendix G, p. 533. 1981
- ³⁰Roskam, Jan. Airplane Design Part VI. DAR Corporation. 1990. p. 21.
- ³¹Roskam, Jan. Airplane Design. Part VI. DAR Corporation. 1990. All Sections relevant to Class II drag polar analysis for light airplanes were used.
- ³²Torenbeek, E. Synthesis of Subsonic Airplane Design. Chapters pertaining to low speed aerodynamic predictions. 1981

- ³³ *Roskam, Jan.* Airplane Design Part VI. DAR Corporation. 1990. Section 4.12.2, pgs 110-111
- ³⁴ *Oberg, Eric, et. al.* Machinery's Handbook. Industrial Press. 28th Edition. Feb 2008
- ³⁵ Advanced Aircraft Analysis help file on Structure. DAR Corporation. Keyword Libove's Axis. Wichita, Kansas. 2009.
- ³⁶ *Roskam, Jan.* Airplane Design. Part IV. DAR Corporation, 1990. Section 2.4. Pg. 4. Note: Roskam derives his requirements from FAR §23.725.
- ³⁷ *Oberg, Eric, et. al.* Machinery's Handbook. Industrial Press. 28th Edition. Feb 2008
- ³⁸ *Molyneux, W.G., Hall, H.* The Aerodynamic Effects of Aspect Ratio and Sweepback on Wing Flutter, Aeronautical Research Council-Reports & Memorandum . Her majesties Stationary Office, 1957
- ³⁹ *Krishnan, R.* Permanent Magnet Synchronous and Brushless DC Motor Devices. CRC Press. 2010.
- ⁴⁰ *Hartzell Propeller Inc.* Advanced Propeller Design and Manufacturing. Technical Questions. 2009
- ⁴¹ *Dr. Lutgard C. De Jonghe*, Faculty Senior Scientist at Lawrence Berkeley National Laboratory and Chairman of PolyPlus Battery Company, and *Dr. Binod Kumar*, University of Dayton Research Institute. Energy Storage & Generation. Electromechanical Power. Group Leader/Distinguished Research Engineer. Professor in the department of Aerospace and Mechanical Engineering, University of Dayton, OH.
- ⁴² *Bercheršky, Gene et. al.* The Tesla Roadster Battery System. Tesla Motors, 2006.
- ⁴³ Fokker Technologies. Fokker Services introduces Electronic Flight Bag hardware and mounting solution for iPad. 2011
- ⁴⁴ *Berdichevsky, G., et. al.* The Tesla Roadster Battery System. Tesla Motors, 2006.
- ⁴⁵ *Shah, R.K. and Sekulić, D.* Fundamentals of Heat Exchanger Design. John Wiley & Sons, 2003.
- ⁴⁶ *Hesselgreaves, John E.* Compact Heat Exchangers: Selection, Design, and Operation. Pergamon, 2001.
- ⁴⁷ "Engineering Science Data Unit". Volumes on Aircraft Performance, item 83042. "Estimation of Spray Patterns Generated from the Sides of Aircraft Tires Running in Water or Slush." Amendment A. April, 1998.
- ⁴⁸ *Roskam, Jan.* Airplane Design Part V. DAR Corporation, 1997. p. 25
- ⁴⁹ *Schmitt, R.L. et. al.* Weight Estimation Handbook for Light Aircraft. Cessna Aircraft Company, 1959.
- ⁵⁰ *Torenbeek, E.* Synthesis of Subsonic Airplane Design. Kluwer Boston Inc., 1982.
- ⁵¹ *Roskam, Jan.* Airplane Design. Part V. DAR Corporation, 1990.
- ⁵² *Roskam, Jan.* Airplane Flight Dynamics and Automated Flight Controls. Part I Sec. 4.2.2. p. 205. 2003
- ⁵³ *Roskam, Jan.* Airplane Design Part II. Section 11.1, pp. 24-25. DAR Corporation, 1997.
- ⁵⁴ Military Specification MIL-F-8785 B Flying Qualities of Piloted Airplanes; 1969: Air Force Flight Dynamics Laboratory, WP AFB, Dayton, Ohio.
- ⁵⁵ *Roskam, Jan.* Airplane Flight Dynamics and Automatic Flight Controls, Part I, DAR Corporation, 2003, p. 186.
- ⁵⁶ *Roskam, Jan.* Airplane Flight Dynamics and Automatic Flight Controls, Part I, DAR Corporation, 2003, p. 143.
- ⁵⁷ Military Specification MIL-F-8785 B Flying Qualities of Piloted Airplanes; 1969: Air Force Flight Dynamics Laboratory, WP AFB, Dayton, Ohio.
- ⁵⁸ *Roskam, Jan.* Airplane Flight Dynamica and Automatic Flight Controls, Part I, DAR Corporation, 2003, p. 205.
- ⁵⁹ *Roskam, Jan.* Airplane Flight Dynamics and Automatic Flight Controls, Part I, DAR Corporation, 1997, Secs. 5.3.2 & 5.3.10
- ⁶⁰ *Hoak. D.E.,*"USAF Stability and Control DATCOM, Wrie Paterson AFB, OH
- ⁶¹ *Roskam, Jan.* Airplane Flight Dynamics and Automatic Flight Controls Part I, Section 5.2.4 & 5.2.5 PP 329-337 DAR Corp. 2003
- ⁶² *Roskam, Jan.* Airplane Design Part VI. Sec. 10. P 371-377. DAR Corporation. 1991.
- ⁶³ *Roskam, Jan.* Airplane Design Part VI. Section 6.4, pp. 193-198. DAR Corporation, 1990.
- ⁶⁴ "Engineering Science Data Unit". *Volumes on Performance*, item 85029. "Calculation of Ground Performance in Takeoff and Landing". Amendment A. March 2006.
- ⁶⁵ "Engineering Science Data Unit". *Volumes on Aerodynamics*, item 71007. "Low Speed Normal Force and Pitching Moment of Slender Wings in Ground Effects". June 1971
- ⁶⁶ *Roskam, Jan.* Airplane Design Part VII Sec. 5.2 p. 117-123. DAR Corporation. 1991
- ⁶⁷ *Roskam, Jan.* Airplane Design Part VII Sec 5.3. p. 124-130. DAR Corporation. 1991.
- ⁶⁸ *Roskam, Jan.* Airplane Design Part VII Sec 5.7. p. 150-155. DAR Corporation. 1991.
- ⁶⁹ Engineering Science Data Unit. *Volumes on Performance*, item 91032. "Estimation of Airborne Performance and Landing". October 1991.

- ⁷⁰ Engineering Science Data Unit. *Volumes on Performance*, item 92020. “Energy Method for Analysis of Measured Airspeed Change in Landing Airborne Maneuvers.” Amendment A, December 1996.
- ⁷¹ Engineering Science Data Unit. *Volumes on Performance*, item EG6/4. “Estimation of Ground Run During Landing.” Amendment B, February 1992.
- ⁷² Roskam, Jan. Airplane Design, Part VII. Sec. 5.1, pp. 113-116. DAR Corporation, 1991.
- ⁷³ Marte, Jack E. A Review of Aerodynamic Noise from Propellers, Rotors, and Lift Fans. National Aeronautics and Space Administration. Jet Propulsion Laboratory. Technical Report 32-1462. 1970
- ⁷⁴ SAE International. SAE Electric Vehicle Conductive Charge Coupler. 2001.
- ⁷⁵ Kumar, B. Personal correspondence. 2011.
- ⁷⁶ Gunawardana, S. Electric Airplane Research Program. Stanford University. 2009.
- ⁷⁷ National Transport Safety Board. Annual Review of Aircraft Accident Data: U.S. General Aviation. 2005.
- ⁷⁸ Knacke, Theo W. Parachute Recovery Systems Design Manual. Naval Weapons Center, 1991.
- ⁷⁹ Cesaroni Technology. Pro 29 2010 Catalog. V 1.0. Sarasota, FL.
- ⁸⁰ BRS Aerospace. Recovery Systems Spec Sheet.
- ⁸¹ Oregon Aero High-G Seat. <http://www.oregonaero.com/seat-systems/oem-high-g>. Accessed April 3, 2011.
- ⁸² Laminar Research. X-Plane v. 9.00. Created by Austin Meyer. <http://www.x-plane.com>.
- ⁸³ Szatkowski, George. Lightning Strike Protection for Composite Aircraft. NASA Langley Research Center, 2009.
- ⁸⁴ Roskam, Jan. Airplane Design. Part III. DAR Corporation. 1991.
- ⁸⁵ Szatkowski, George. Lightning Strike Protection for Composite Aircraft. NASA Langley Research Center, 2009.
- ⁸⁶ Federal Aviation Administration. “Certification of Aircraft and Airmen for the Operation of Light-Sport Aircraft”. July, 2004.
- ⁸⁷ Federal Aviation Administration. “2011-2031 Aerospace Forecast”. 2011.
- ⁸⁸ General Aviation Manufacturer Association. “General Aviation: Statistical Databook & Industry Outlook”. 2010.
- ⁸⁹ Linden, David and Reddy, Thomas. “Handbook of Batteries” 3rd Edition. McGraw-Hill, 2001.
- ⁹⁰ Bullis, Kevin. High-Energy Batteries Coming to Market. Technology Review, MIT. 2009.
- ⁹¹ Linden, David and Reddy, Thomas. “Handbook of Batteries” 3rd Edition. McGraw-Hill, 2001.
- ⁹² Roskam, Jan. Airplane Design. Part VIII. DAR Corporation, 1991.
- ⁹³ Resetar, Susan et. al. “Advanced Airframe Structural Materials: A Primer and Cost Estimating Methodology”. RAND Corporation, 1991.
- ⁹⁴ Roskam, Jan. Airplane Design. Part VIII. DAR Corporation, 1991.
- ⁹⁵ US Energy Information Administration. “Monthly Electric Sales and Revenue Report with State Distribution Reports” Jan. 2011.
- ⁹⁶ Cessna. Skycatcher: Performance and Specifications. <http://www.cessna.com/single-engine/skycatcher/skycatcher-performance.html>. Accessed May 2011.